The Effect Of Rayleigh-Taylor Instabilities On The Thickness Of Undifferentiated Crust On Kuiper Belt Objects Like Charon

by

Mark Rubin

A Thesis Presented in Partial Fulfillment
of the Requirement for the Degree
Masters of Science

Approved April 2013 by the
Graduate Supervisory Committee:

Steven Desch, Chair
Thomas Sharp
Phil R. Christensen

ARIZONA STATE UNIVERSITY

May 2013

ABSTRACT

In this thesis I model the thermal and structural evolution of Kuiper Belt Objects (KBOs) and explore their ability to retain undifferentiated crusts of rock and ice over geologic timescales. Previous calculations by Desch et al. (2009) predicted that initially homogenous KBOs comparable in size to Charon ($R \sim 600$ km) have surfaces too cold to permit the separation of rock and ice, and should always retain thick (≈ 85 km) crusts, despite the *partial* differentiation of rock and ice inside the body. The retention of a thermally insulating, undifferentiated crust is favorable to the maintenance of subsurface liquid and potentially cryovolcanism on the KBO surface. A potential objection to these models is that the dense crust of rock and ice overlying an ice mantle represents a gravitationally unstable configuration that should overturn by Rayleigh-Taylor (RT) instabilities. I have calculated the growth rate of RT instabilities at the ice-crust interface, including the effect of rock on the viscosity. I have identified a critical ice viscosity for the instability to grow significantly over the age of the solar system. I have calculated the viscosity as a function of temperature for conditions relevant to marginal instability. I find that RT instabilities on a Charon-sized KBO require temperatures $T > 143$ K. Including this effect in thermal evolution models of KBOs, I find that the undifferentiated crust on KBOs is thinner than previously calculated, only ≈ 50 km. While thinner, this crustal thickness is still significant, representing $\approx 25\%$ of the KBO mass, and helps to maintain subsurface liquid throughout most of the KBO's history.

TABLE OF CONTENTS

CHAPTER Page

CHAPTER Page

LIST OF TABLES

LIST OF FIGURES

Figure Page

Figure Page

Figure Page

Chapter 1

INTRODUCTION

1.1 Background

Although hypothesized to exist as early as 1930, the first Kuiper Belt Object (KBO) wasn't discovered until 1992 by Jewitt and Luu (1993). Clyde Tombaugh's discovery of Pluto in 1930 caused Frederick Leonard to speculate that Pluto might be the first in a series of ultra-Neptunian bodies yet to be discovered in the Solar system (Leonard 1930). In 1943 Kenneth Edgeworth postulated that the region beyond Neptune might be populated by a very large number of comparatively small objects left over from the formation of the solar system. He predicted that these objects might be the source for comets (Edgeworth 1943). In 1951 Gerard Kuiper also predicted the existence of a primordial disk of objects outside of the orbit of Pluto; however he expected the disk to eventually scatter leaving this region of space empty today (Kuiper 1951).

Since 1992, more than 1260 KBOs (Vitense et al. 2010) have been discovered with semi-major axes ranging from 30 to 55 AU, including dwarf planets such as Pluto, Eris and Haumea. The total number of KBOs with radii > 50 km has been modeled to be $> 100,000$, although the total mass contained within the Kuiper belt is expected to be < 0.12 Earth masses (Vitense et al. 2010). Unlike their terrestrial cousins, many KBOs (as well as the icy satellites of the giant planets) have densities on the order of 1 to 2 $\mathrm{g\,cm^{-3}}$, consistent with a ratio of ice to rock of greater than 50%. Compounds such as crystalline water ice, methane and ammonia have been found on their surface (Brown 2012). Their extremely low surface temperatures ($\sim 40 - 55$ K), high water

content and low densities make them unique objects in the solar system; and their thermal evolution, differentiation and structure are only beginning to be understood now.

Fig. 1.1 illustrates the relative size of eight of the largest Trans-Neptunian Objects (TNOs) relative to Earth. TNOs include KBOs as well as scattered disk objects whose semi-major axes can extend considerably further from the sun than classical KBOs. As an example, Eris is roughly the same size as Pluto, but its aphelion occurs at $\sim$ 98 AU.

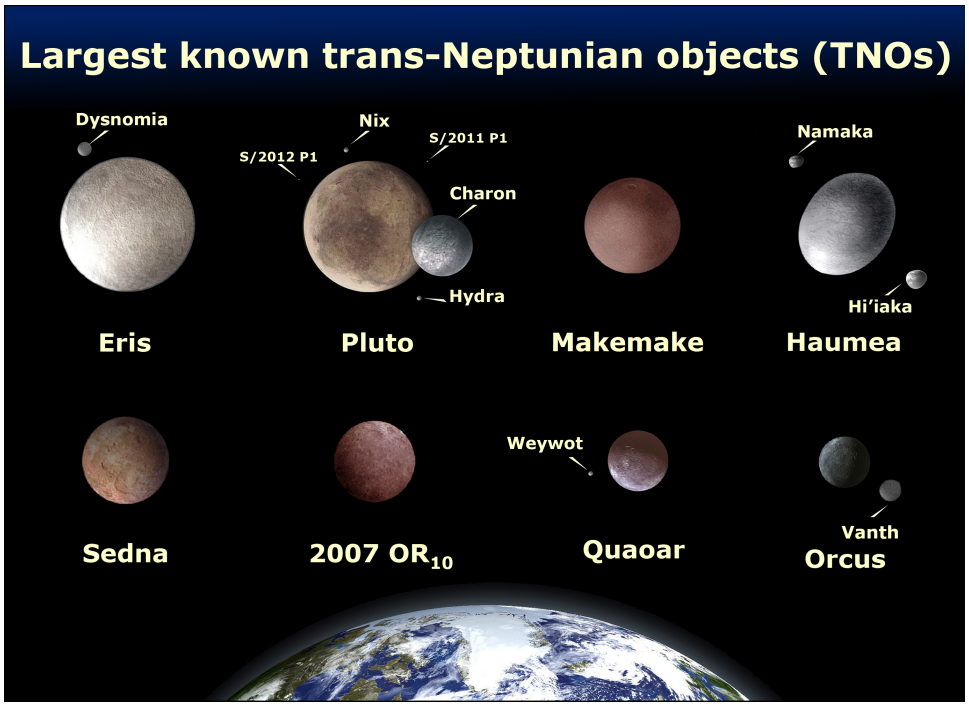

Figure 1.1: An artist's rendition displays eight of the largest TNOs. The radius of Pluto and Eris are roughly equal at $\sim$ 1200 km, but Eris is substantially denser ($\bar{\rho}_{\rm Eris} \sim 2.52\,{\rm g\,cm^{-3}}$ and $\bar{\rho}_{\rm Pluto} = 1.75\,{\rm g\,cm^{-3}}$). Charon ($R_{\rm Charon} \sim 600$ km and $\bar{\rho}_{\rm Charon} \sim 1.65\,{\rm g\,cm^{-3}}$) is the largest of Pluto's moons, and is the primary focus of the model runs performed in this thesis. Two other objects worth mentioning are Ceres, which is located in the asteroid belt, and Neptune's moon Triton, both of which are believed to have originated in the Kuiper belt. Triton is larger than any of the KBOs discovered to date ($R_{\rm Triton} = 1350$ km and $\bar{\rho}_{\rm Triton} = 2.06\,{\rm g\,cm^{-3}}$).

The models presented in this thesis are an extension of the model presented in Desch et al. (2009) and explore the thermal evolution and differentiation processes

for KBOs and other small icy bodies. One of the main results of this model, and one that I will be exploring in detail, is the possibility that KBOs only partially differentiate, resulting in the presence of a thick undifferentiated crust. This crust is thermally insulating and can help sustain internal temperatures high enough to support the presence of subsurface oceans. As the subsurface liquid freezes, it may find its way to the surface through self-propagating cracks, allowing cryovolcanism to occur (Crawford and Stevenson 1988). This cryovolcanism can result in the resurfacing of KBOs, a process frequently observed on the icy moons of the giant planets.

Another intriguing possibility that may result from these subsurface oceans is the creation of conditions that might be suitable for the formation of life. At the bottom of these subsurface oceans, where the liquid comes into contact with the hot rocky core, chemical reactions similar to those found in the "black smokers" at the bottom of Earth's oceans might occur. Admittedly, this is a long-shot, but still remains within the realm of possibility. Therefore, establishing the existence of an undifferentiated crust may have broader implications, especially for cryovolcanism.

Cryovolcanism has been established as a process for reshaping the surfaces of many icy bodies in the solar system. Observations of many of the icy satellites of the giant planets show evidence for cryovolcanism on their surface, and the implied presence of subsurface liquids. Since the time of the Voyager missions, Europa has been known to have an extremely young surface ($\sim$ 50 Myr) (Smith et al. 1979; Zahnle et al. 2003), and there is mounting evidence for the role of cryovolcanism on its resurfacing (Figueredo and Greeley 2004). Additionally, magnetometer measurements from the Galileo probe strongly indicate that Europa contains a subsurface ocean (Kivelson et al. 2000). On Ganymede, bright terrain on its surface has been interpreted as resulting from cryovolcanism in places where liquid has filled in low-lying grabens (Showman et al. 2004).

Further evidence for cryovolcanism exists on Enceladus, where much of its surface appears to be extremely young and uncratered resulting from recent resurfacing events ($< 10^8$ yr). It also has tectonic features which may be the result of cryovolcanism (Kargel and Pozio 1996). In addition, the Cassini probe has made the remarkable observation of a plume of icy material escaping from the moon's southern polar region, a region which is especially young and active (Porco et al. 2006; Hansen et al. 2006). On Titan, the Cassini Titan Radar Mapper observed evidence for a large shield volcano along with three calderas and several flows, all indicative of cryovolcanism.

Finally, many other outer solar system satellites such as Miranda, Ariel and Triton show extensive evidence for cryovolcanic activity. In most of these cases, the source of the heat flux for this tectonic activity is theorized to be the result of both tidal dissipation and internal radiogenic heating (Nimmo et al. 2002; Nimmo and Pappalardo 2004; Dombard and McKinnon 2001). Therefore, it is unclear from these observations whether an isolated KBO of similar radius will experience cryovolcanism without having available the additional source of heating from tidal forces. Additionally, there are currently no observations of KBOs with sufficient resolution to determine their surface morphology, although this situation will change when the New Horizons probe arrives at the Pluto/Charon system in 2015.

For now, the evidence for cryovolcanism on the surface of KBOs is more indirect and includes spectroscopic observations of crystalline water ice and ammonia on the surface of KBO. Crystalline water ice is converted to amorphous ice through exposure to galactic cosmic rays (GCRs) with energies $\sim$ 3 eV per molecule, and evidence for ammonia hydrates is removed by particles with energy $\sim$ 100 eV per molecule (Mastrapa and Brown 2006; Cook et al. 2007). When the additional ionizing effect of ultraviolet solar photons is included, Cook et al. (2007) determined that the spectral signatures for crystalline water ice and ammonia hydrates should be destroyed within

0.03 and 1 Myr, respectively. This makes the discovery of these compounds on the surface of KBOs difficult to explain.

Cryovolcanism provides a possible mechanism to replenish the crystalline water ice and ammonia hydrates found on the surface of KBOs, as water containing ammonia is erupted from their interior onto the surface. This possibility is enhanced by the ability of ammonia to lower the melting point of water from 273 to 176 K, thus facilitating the possibility for cryovolcanism at the very low temperatures found in KBOs. In particular, Cook et al. (2007) used their observations for the presence of crystalline water ice and ammonia hydrates on the surface of Pluto's moon Charon, to argue for the existence of cryovolcanism on Charon.

An alternative mechanism for the creation of the crystalline water ice found on the surface of KBOs is from the heat generated by micrometeorite impacts into the amorphous ice. These have the ability to locally anneal the ice, recrystallizing it. Cook et al. (2007) estimated that these impacts can anneal ice on timescales of ~ 5 Myr. However, they also found that the amorphization of crystalline water ice can occur on timescales as low as 3×10^4 yr through the action of GCRs and UV photons. Thus, unless the flux of micrometeorites in the Kuiper belt is many order of magnitude larger than that measured between 1 and 18 AU by Pioneer 10 (Humes 1980), the annealing action of micrometeorites in insufficient to overcome the amorphizing effect of GCRs and UV photons. So we are left with the question of how crystalline water ice and ammonia can be maintained on the surface of KBOs. Cryovolcanism may explain the crystalline ice on the surface.

With limited observational evidence for cryovolcanism on KBOs being available, the task to predict the occurrence of cryovolcanism and related phenomena falls on the modeling community. Direct imaging of Pluto and Charon will be possible when the New Horizons probe arrives in 2015 (Stern 2008), thereby allowing us to directly

determine whether they have experienced cryovolcanism. However, interpretation of these results still requires a theoretical understanding of the mechanisms underpinning cryovolcanism, and therefore a proper model for the differentiation and evolution of the KBOs on which cryovolcanism is observed. Conversely, theoretical models can help us to use observations of surface morphology and evidence for cryovolcanism to help determine the internal structure of KBOs.

1.2 Thermal Evolution Models of Kuiper Belt Object Interiors

Desch et al. (2009) developed a numerical code to calculate the thermal evolution for the interior of icy bodies with radii ranging from $\sim$ 400 - 1000 km. This code solves the 1-D (spherical) heat conduction equation in a way that fully incorporates time-dependence. While other models have either considered a completely homogeneous body, or one that is fully differentiated, the differentiation process incorporated in this model allows us to capture the effects of differentiation over time. As will be explained in more detail in Chapter 4, the maintenance of subsurface liquid is optimized when a hot rocky core lies beneath an enveloping ice mantle, which is in turn surrounded by an undifferentiated crust of rock and ice. The crust acts to thermally insulate the ice layer beneath it, so that sufficient heat is maintained at the core/mantle boundary to sustain the presence of liquid for many Gyr into the evolution of the KBO. A final component of the model is the inclusion of the effect of ammonia on the differentiation process. Ammonia has the effect of dramatically lowering the viscosity of water ice to the point where Stokes flow can differentiate the KBO at temperatures much lower than would be otherwise possible, and it is a powerful antifreeze.

The code of Desch et al. (2009) is the first code to include all of the relevant effects (time-dependence, ammonia, partial differentiation) on the thermal evolution of KBOs, although other models have incorporated a subset of these effects. Ruiz

(2003) estimated the depth of the ice layer on Triton's surface using a steady-state model. Hussman et al. (2006) created steady-state models for icy satellites and KBOs that were either fully differentiated or homogeneous. De Sanctis et al. (2001) modeled the thermal evolution of porous KBOs without consideration for differentiation, and Shchuko et al. (2006) did the same for the small, porous KBO, Varuna. These models were appropriate considering the small size of the objects that they were modeling. Ellsworth and Shubert (1983) developed thermal evolution models for icy satellites, but did not include changes to their structure due to differentiation. Prialnick and Bar-Nun (1990) modeled the thermal evolution of icy satellites due to long and short-lived radionuclides, but did not include the effects of differentiation or ammonia. McKinnon (2002) modeled the thermal evolution of KBOs without consideration of differentiation. The numerical code used by Schubert et al. (2007) to study Enceladus includes the effects of time evolution and differentiation but does not include ammonia. To our knowledge, the only other code that included all of the relevant effects is that used by Castillo-Rogez et al. (2007a) which included time evolution as well as the effects of ammonia and differentiation. While this code has been applied to Iapetus (Castillo-Rogez et al. 2007a), Rhea (Castillo-Rogez, 2006) and Ceres (Castillo-Rogez et al. 2007b), it has not yet been applied to KBOs.

The models of Desch et al. (2009) begin with the accretion of a mixture of rocky material ($\rho_{\rm rock} = 3.25\,{\rm g\,cm^{-3}}$) and ices ($\rho_{\rm ice} \sim 1\,{\rm g\,cm^{-3}}$). Heating due to long-lived radionuclides gradually warms the KBO. The inclusion of ammonia in the model with $\chi \geq 1\%$ (where χ is the weight fraction of ammonia relative to ammonia plus water) causes the viscosity of the ice to drop by 5 orders of magnitude when the temperature of any given layer rises above 176 K. This drop in viscosity facilitates Stokes flow, whereby meter-sized rocks separate from the ice and fall towards the core causing the body to differentiate as illustrated in Fig. 1.2. Differentiation eventually creates

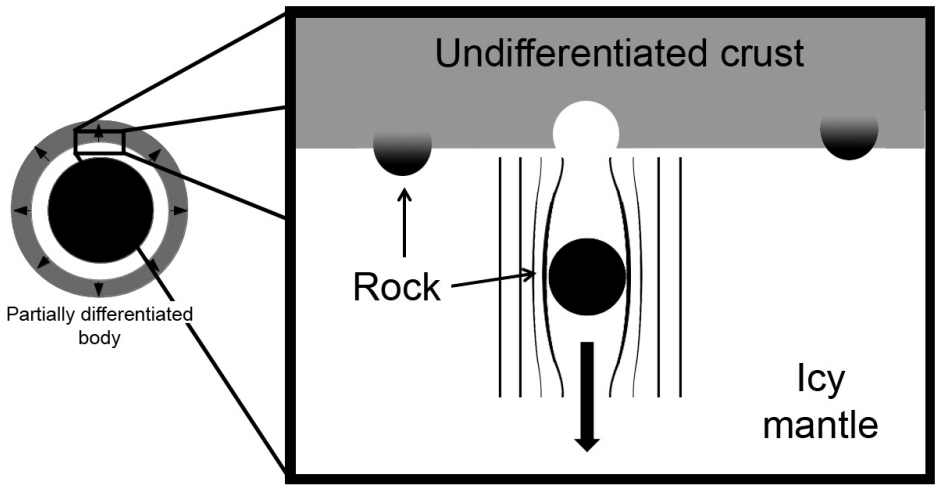

Figure 1.2: Stokes flow of meter-sized rock through the ice layer, causing differentiation to proceed outwards through the body. A 1-meter rock will fall ~ 10 km/Myr through the ice if $T > 176$ K, and less than 0.1 km/ 5 Gyr if $T < 176$ K.

a hot rocky core ($\rho \sim 3\,\mathrm{g\,cm^{-3}}$), surrounded by a liquid layer containing water and ammonia, which is in turn surrounded by a pure water ice mantle ($\rho \sim 1\,\mathrm{g\,cm^{-3}}$). The model predicts that for a Charon-sized body with $\bar{\rho} = 1.70\,\mathrm{g\,cm^{-3}}$, the outer crust will never rise above $T = 176$ K and will therefore never differentiate. This is due to the extremely low surface temperatures of KBOs which result in very high viscosities near their surfaces. This partial differentiation results in the formation of an undifferentiated rockk/ice crust with a depth of 85 km as illustrated in Fig. 1.3. The model also predicts the presence of subsurface liquid today that could be a source for current cryovolcanism on Charon.

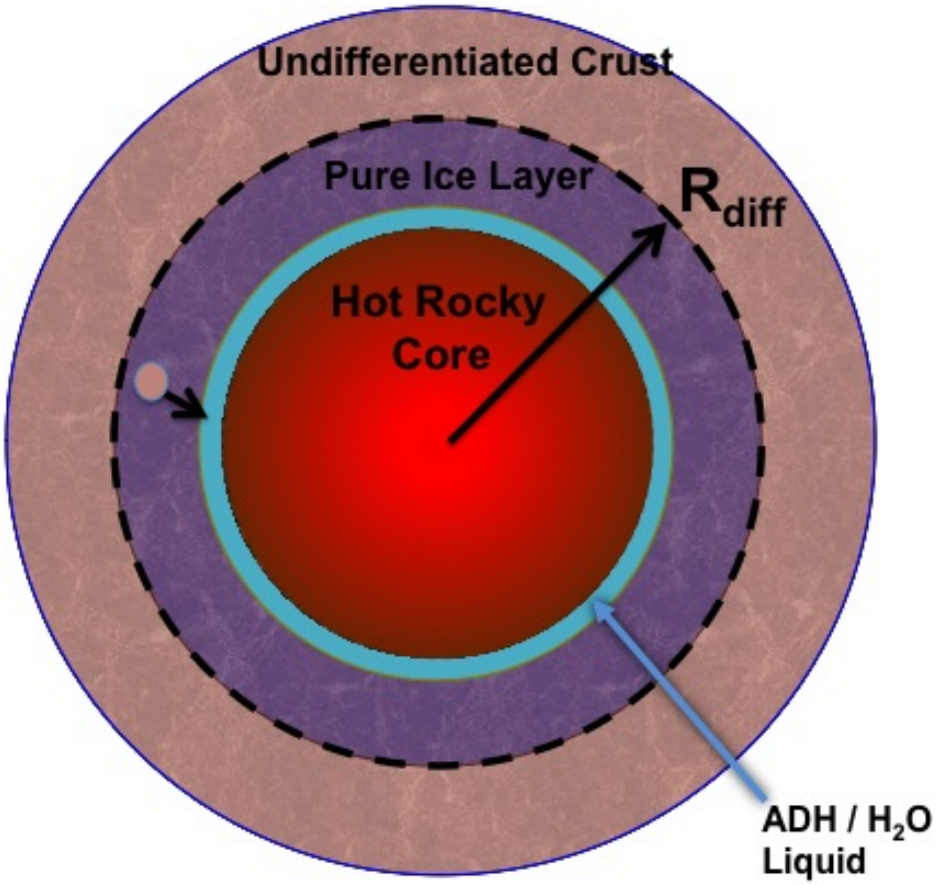

Figure 1.3: Depiction of the differentiation model of Desch et al. (2009). It is assumed that differentiation occurs from inside out, because temperatures decrease from the center of the body to its surface. As individual layers rise above 176 K, each layer will begin to differentiate via Stokes flow as 1 meter-sized rocks fall towards the core. This model predicts that a Charon-sized will only partially differentiate out to a radius of $R_{\rm diff}$, leaving an undifferentiated crust of ≈ 85 km.

1.3 Current Research

In this research I address two significant objections to the numerical models of Desch et al. (2009). The first is the assumption of differentiation due to the action of Stokes flow. If $\chi < 1\%$, the drop in viscosity of the ammonia-bearing ice at 176 K may be insufficient to cause the separation of ice from rock on geological timescales. Furthermore, if the rock that originally accreted to form the KBO is composed of centimeter-sized particles as opposed to meter-sized rock, the separation of rock from ice will only occur at much higher temperatures. In either case, differentiation is still likely inside the KBO, but might not begin until the temperature of any given shell reaches the melting point of water ice at 273 K. The second objection is that the existence of an undifferentiated crust with density $\bar{\rho} = 1.70\,\mathrm{g\,cm^{-3}}$ overlying a lower-density ice mantle with $\rho_{\mathrm{ice}} \sim 1\,\mathrm{g\,cm^{-3}}$ is gravitationally unstable, and therefore prone to Rayleigh-Taylor instabilities. It is conceivable that these instabilities could completely overturn the crust. This thesis quantifies the ability of Rayleigh-Taylor instabilities to overturn the undifferentiated crust of KBOs. In particular, I focus on the ability for a Charon-like object to maintain an undifferentiated crust, since we may be able to get observational verification for the model when the New Horizons probe reaches Charon in 2015.

To be clear, the models I developed for this research assume that some differentiation has already occurred, either via Stokes flow, or when the ice matrix has reached its melting point at 273 K. So we now have a partially differentiated body, where a rocky core is surrounded by a liquid layer and ice mantle and finally the undifferentiated crust. This crust may be unstable to gravitational overturn over geological time frames. My current research explores whether this partially differentiated body will now fully differentiate due to Rayleigh-Taylor instabilities.

This thesis is organized as follows. In Chapter 2, I perform a linear stability analysis on the boundary layer between the ice mantle and the overlying crust based on the work of Chandrasekhar (1961). I use this analysis to determine a critical viscosity η_{crit} for the ice layer at which a disturbance can grow in amplitude by a factor of 10 in 1.5 Gyr (roughly the time the interface will be at its maximum temperature for a body like Charon). If the viscosity of the ice layer is greater than η_{crit}, then we do not expect any disturbance to be strong enough to overturn the crust. Chapter 3 explores the distinctly non-Newtonian rheology of the water ice at the very low temperatures found in the ice mantle. Based on the work of Goldsby and Kohlstedt (2001), I determine a composite flow law for the ice which enables me to model the relationship between the viscosity of the ice and its temperature. From this I am able to determine a differentiation temperature T_{diff} which corresponds with the viscosity η_{crit} determined in Chapter 2. Chapter 4 reviews the thermal evolution code of Desch et al. (2009) which is the basis for my models. Chapter 5 is a summary and discussion of my results determined by using a T_{diff} appropriate for Rayleigh-Taylor instabilities. In this chapter I vary some of the material parameters for the model of Charon, and in each case I determine the thickness of the resulting undifferentiated crust. The final chapter concludes with the result that even with the inclusion of Rayleigh-Taylor instabilities, our Charon analog still retains an undifferentiated crust of at least 50 km up to the present.

Chapter 2

RAYLEIGH-TAYLOR INSTABILITIES

2.1 Derivation of Growth Rates

2.1.1 Overview

This chapter explores the effect of Rayleigh-Taylor instabilities on the evolution of an icy body. Here, I assume that the release of energy due to radiogenic sources, core formation and accretion have heated the body to the point where some differentiation has occurred. The heavier rocky material has settled to the center due to Stokes flow through ice, or outright melting of the ice, leaving a rocky core. This core is surrounded by a layer of liquid and ice, which is in turn surrounded by a primordial, undifferentiated layer of well-mixed rock and ice. The outermost layer is denser than the ice beneath it, and gravitational forces will make it unstable to mixing over geological time scales. Following closely upon the discussion of R-T instabilities in chapter 10 of S. Chandrasekhar's book, Hydrodynamic and Hydromagnetic Stability, this chapter attempts to model whether a disturbance, once created, can eventually overturn the undifferentiated crust of the body.

Consider a uniform horizontal layer of ice with density, ρ_1, and viscosity, η_1, underneath an undifferentiated layer of material with density, ρ_2, and viscosity, η_2. For the purpose of this discussion, both layers are considered to be incompressible fluids with a horizontal interface at $z = 0$, and are initially static. The only external force felt by the strata is the gravitational acceleration, g, due to material interior to the interface. At some time $t = 0$, the system is slightly disturbed. The resulting disturbance will have a wavelength λ parallel to the interface, with some initial amplitude

Δy perpendicular to the interface. Fig. 2.1 illustrates the initial disturbance, and Fig. 2.2 shows how this disturbance can grow in time, eventually overturning the crust. In the sections that follow I determine an exponential growth rate n for the disturbance which can then be used to model the likelihood for overturn.

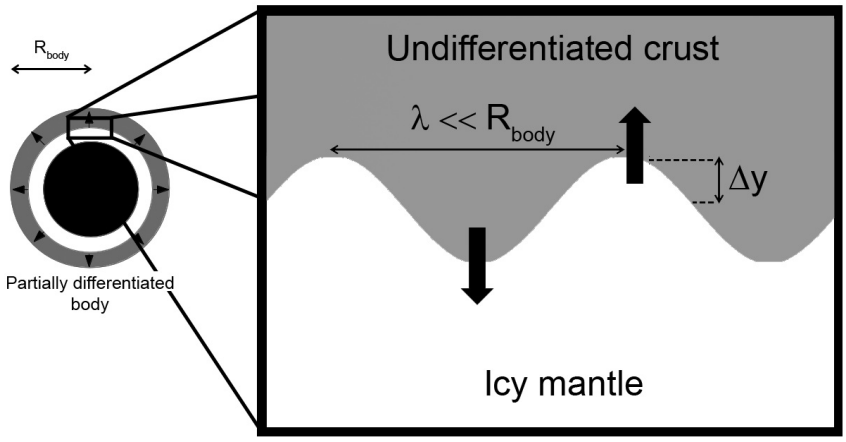

Figure 2.1: The initial disturbance between the ice mantle and overlying denser crust is modeled as a sinusoidal oscillation with wavelength λ, and initial amplitude Δy.

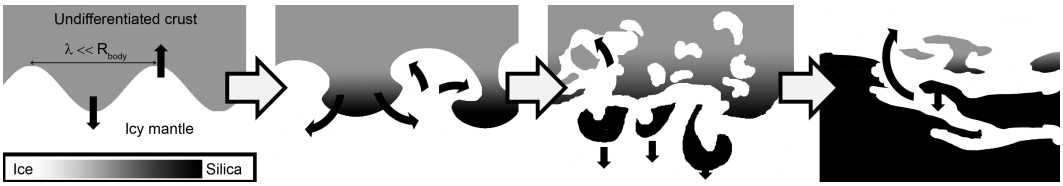

Figure 2.2: Schematic growth of the instability, eventually resulting in crustal overturn. Darker areas enriched in silicate grains.

Once the layer is perturbed, the actual density at any point (x, y, z) will be $\rho + \delta\rho$, with a corresponding increase in pressure, δp. We assume zero initial velocities at any given point, and once perturbed there will be some corresponding increase in local velocities, (u, v, w) or $u_i (i = 1, 2, 3)$ (considered small). The following subsections derive the evolution of the system, starting with such fundamentals as conservation of mass and momentum for the system.

2.1.2 Conservation of Mass

To derive the continuity equation for conservation of mass, consider a closed volume V, bounded by a surface S. Any increase in the mass interior to S must pass through the boundary. The mass inside the volume is given by $\int_V \rho\, dV$, and any change of the mass inside S is given by

$$\frac{d}{dt}\int_V \rho\, dV = \int_V \frac{\partial \rho}{\partial t}\, dV.$$

The rate of flow of mass through any surface element is given by $\rho\,\vec{v}\cdot d\vec{S}$. Thus, for the entire surface S, the rate of flow of material into the volume is given by

$$\int_S \rho\,\vec{v}\cdot d\vec{S} = \int_V \nabla\cdot(\rho\,\vec{v})dV$$

(by Green's Theorem). We can now set the rate of change in mass inside V equal to the rate of flow of mass into V. Noting this is equation is valid for any volume V, it follows that

$$\frac{\partial \rho}{\partial t} = \vec{\nabla}\cdot(\rho\,\vec{v}) \tag{2.1}$$

which is the Continuity Equation for Mass. If we use Cartesian coordinates, and define $\vec{v} = (u, v, w)$, we get

$$\begin{aligned}
\frac{\partial \rho}{\partial t} &= \vec{\nabla}\cdot(\rho\,\vec{v}) \\
&= \tfrac{\partial}{\partial x}(\rho u) + \tfrac{\partial}{\partial y}(\rho v) + \tfrac{\partial}{\partial z}(\rho w) \\
&= \rho\tfrac{\partial u}{\partial x} + u\tfrac{\partial \rho}{\partial x} + \rho\tfrac{\partial v}{\partial y} + v\tfrac{\partial \rho}{\partial y} + \rho\tfrac{\partial w}{\partial z} + w\tfrac{\partial \rho}{\partial w}.
\end{aligned}$$

Under the assumption that the ice layers are incompressible, ρ must be a constant in time and space within each layer, and our continuity equation becomes

$$\vec{\nabla}\cdot\vec{v} = \frac{\partial u}{\partial x} + \frac{\partial v}{\partial y} + \frac{\partial w}{\partial z} = 0.$$

This can be expressed using Einstein notation as

$$\frac{\partial v_i}{\partial x_i} = 0, \tag{2.2}$$

which corresponds with Eq. 2 of Chandrasekhar.

2.1.3 Conservation of Momentum

If we consider a volume of fluid V bounded by a material surface S that is moving with the flow, its momentum is given by $\int_V \rho\,\vec{v}\,dV$. The rate of change in momentum is then

$$\frac{d}{dt}\int_V \rho\,\vec{v}\,dV = \int_V \rho\,\frac{D\vec{v}}{Dt}\,dV. \tag{2.3}$$

This must be equal to the net force acting on each element.

Here D/Dt is the total (material) derivative, defined as follows.

If we have a function that is varying both in time and space, $f(x(t), y(t), z(t), t)$, we need to consider both the rate of change of f at a particular fixed point in space, $\partial f/\partial t$, and the rate of change of f for a given fluid element as it moves along its trajectory $\vec{x} = \vec{x}(t)$. The spatial part of the derivative is given by

$$\begin{aligned}\frac{d\left(f(\vec{x})\right)}{dt} &= \tfrac{dx}{dt}\tfrac{\partial f}{\partial x} + \tfrac{dy}{dt}\tfrac{\partial f}{\partial y} + \tfrac{dz}{dt}\tfrac{\partial f}{\partial z} \\ &= u\tfrac{\partial f}{\partial x} + v\tfrac{\partial f}{\partial y} + w\tfrac{\partial f}{\partial z} \\ &= \vec{v}\cdot\vec{\nabla} f\end{aligned}$$

Combining the spatial and time derivates yields the total derivative:

$$\frac{Df}{Dt} = \frac{\partial f}{\partial t} + \vec{v}\cdot\vec{\nabla} f.$$

Alternatively, using operator notation

$$Df = \left(\frac{\partial}{\partial t} + \sum_{i=1}^{k}\frac{dx_i}{dt}\frac{\partial}{\partial x_i}\right) f \text{ where } D \equiv \frac{d}{dt}.$$

The net force acting on each element can be broken down into two components. The first is composed of long range external forces that act equally on any element dV. In our case, we are only considering the gravitational force, $\rho\, g\, dV$. The second component includes short-ranged molecular forces internal to the fluid. For simplicity, we can consider a cubical volume element surrounded by a surface, S. Each of the 3 sets of surface planes bounding S experiences a 3-component force, giving 9 components in all. Together, these comprise the stress tensor, $\vec{\tau}$. The stress tensor is defined so that the force exerted per unit area across a surface element $d\vec{S} \equiv \hat{n}\, dS$ is $\vec{f} = \vec{\tau} \cdot \hat{n}$ (by the fluid on the side to which $\hat{n}$ points on the fluid on the other side).

Combining these terms, we find the total force (body + surface) $= \vec{F} = \int_V \rho\, g\, dV +$ $\int_S \vec{\tau} \cdot d\vec{S}$, or

$$\vec{F} = \int_V (\rho\, g + \vec{\nabla} \cdot \vec{\tau})\, dV. \tag{2.4}$$

Applying Newton's second law to Eqs. 2.3 and 2.4, and noting that the above is true for any volume V, we get

$$\rho \frac{D\vec{v}}{Dt} = \rho\vec{g} + \vec{\nabla} \cdot \vec{\tau} \tag{2.5}$$

Now, in Cartesian Coordinates:

$$\vec{\tau} \equiv \begin{pmatrix} \tau_{xx}\hat{x} & \tau_{xy}\hat{x} & \tau_{xz}\hat{x} \\ \tau_{yx}\hat{y} & \tau_{yy}\hat{y} & \tau_{yz}\hat{y} \\ \tau_{zx}\hat{z} & \tau_{zy}\hat{z} & \tau_{zz}\hat{z} \end{pmatrix}$$

and

$$\vec{\nabla} \cdot \vec{\tau} = \left(\frac{\partial}{\partial x}\hat{x} + \frac{\partial}{\partial y}\hat{y} + \frac{\partial}{\partial z}\hat{z} \right) \cdot \vec{\tau},$$

so in Cartesian coordinates Eq. (2.5) becomes the following equations:

$$\rho \frac{Du}{Dt} = \rho g_x + \frac{\partial}{\partial x}(\tau_{xx}) + \frac{\partial}{\partial y}(\tau_{xy}) + \frac{\partial}{\partial z}(\tau_{xz}) \tag{2.6}$$

$$\rho \frac{Dv}{Dt} = \rho g_y + \frac{\partial}{\partial x}(\tau_{yx}) + \frac{\partial}{\partial y}(\tau_{yy}) + \frac{\partial yz}{\partial z}(\tau_{yz}) \tag{2.7}$$

$$\rho\frac{Dw}{Dt} = \rho g_z + \frac{\partial}{\partial x}(\tau_{zx}) + \frac{\partial}{\partial y}(\tau_{zy}) + \frac{\partial}{\partial z}(\tau_{zz}). \tag{2.8}$$

For an incompressible flow (where $\vec{\nabla}\cdot\vec{v} = 0$) it can be shown that the components of the stress tensor are given by

$$\tau = \begin{pmatrix} -p + 2\mu\frac{\partial u}{\partial x} & \mu\left(\frac{\partial u}{\partial y} + \frac{\partial v}{\partial x}\right) & \mu\left(\frac{\partial u}{\partial z} + \frac{\partial w}{\partial x}\right) \\ \mu\left(\frac{\partial u}{\partial y} + \frac{\partial v}{\partial x}\right) & -p + 2\mu\frac{\partial v}{\partial y} & \mu\left(\frac{\partial v}{\partial z} + \frac{\partial w}{\partial y}\right) \\ \mu\left(\frac{\partial u}{\partial z} + \frac{\partial w}{\partial x}\right) & \mu\left(\frac{\partial v}{\partial z} + \frac{\partial w}{\partial y}\right) & -p + 2\mu\frac{\partial w}{\partial z} \end{pmatrix}.$$

Note that the stress tensor is symmetric, with $\tau_{xy} = \tau_{yx}$, $\tau_{zx} = \tau_{xz}$ and $\tau_{yz} = \tau_{zy}$. Componentwise, the stress tensor can be written as

$$\tau_{ik} = -p\delta_{ik} + \mu\left(\frac{\partial u_k}{\partial x_i} + \frac{\partial u_i}{\partial x_k}\right) \tag{2.9}$$

where $\vec{v} = (u_1, u_2, u_3), \vec{x} = (x_1, x_2, x_3)$ and δ_{ik} is the Kronecker delta.

We can now combine Eqs. 2.5 and 2.9 to get the equations for momentum. For the component of momentum in the x direction,

$$\begin{aligned} \rho\frac{Du}{Dt} = \quad & \rho g_x + \tfrac{\partial}{\partial x}\left(-p + 2\mu\tfrac{\partial u}{\partial x}\right) + \tfrac{\partial}{\partial y}\left(\mu\left(\tfrac{\partial u}{\partial y} + \tfrac{\partial v}{\partial x}\right)\right) \\ & + \tfrac{\partial}{\partial z}\left(\mu\left(\tfrac{\partial u}{\partial z} + \tfrac{\partial w}{\partial x}\right)\right) \\ = \quad & \rho g_x - \tfrac{\partial p}{\partial x} + \mu\left(\tfrac{\partial^2 u}{\partial x^2} + \tfrac{\partial^2 u}{\partial y^2} + \tfrac{\partial^2 u}{\partial z^2}\right) \\ & + \mu\tfrac{\partial}{\partial x}\left(\tfrac{\partial u}{\partial x} + \tfrac{\partial v}{\partial y} + \tfrac{\partial w}{\partial z}\right) \\ & + \tfrac{\partial \mu}{\partial x}\left(\tfrac{\partial u}{\partial x} + \tfrac{\partial u}{\partial x}\right) + \tfrac{\partial \mu}{\partial y}\left(\tfrac{\partial u}{\partial y} + \tfrac{\partial v}{\partial x}\right) + \tfrac{\partial \mu}{\partial z}\left(\tfrac{\partial u}{\partial z} + \tfrac{\partial w}{\partial x}\right) \end{aligned}$$

By Eq. 2.2 we have that $\frac{\partial u}{\partial x} + \frac{\partial v}{\partial y} + \frac{\partial w}{\partial z} = 0$; therefore the equation for the x component of momentum becomes

$$\rho\frac{Du}{Dt} = \rho g_x - \frac{\partial p}{\partial x} + \mu\nabla^2 u + \frac{\partial \mu}{\partial x}\left(\frac{\partial u}{\partial x} + \frac{\partial u}{\partial x}\right) + \frac{\partial \mu}{\partial y}\left(\frac{\partial u}{\partial y} + \frac{\partial v}{\partial x}\right) + \frac{\partial \mu}{\partial z}\left(\frac{\partial w}{\partial x} + \frac{\partial u}{\partial z}\right).$$

Now, if we make the assumption that both viscosity and gravity are only a function of z, then g_x, g_y, $\frac{\partial \mu}{\partial x}$ and $\frac{\partial \mu}{\partial y}$ all vanish and

$$\rho \frac{Du}{Dt} = -\frac{\partial p}{\partial x} + \mu \nabla^2 u + \frac{d\mu}{dz}\left(\frac{\partial w}{\partial x} + \frac{\partial u}{\partial z}\right).$$

2.1.4 Linearization

To get to Chandrasekhar's version of the equation, we need to linearize the momentum in the x-direction. Let us assume that our system is initially static but allow for a slight disturbance in the system. Locally, we will see a slight increase in density so that the density is now $\rho + \delta\rho$ and we have a small velocity u due to the disturbance as it propagates out. Then in our new state,

$$\rho \frac{Du}{Dt} \to (\rho + \delta\rho)\frac{Du}{Dt}$$
$$= (\rho + \delta\rho)\left(\frac{\partial u}{\partial t} + \frac{dx}{dt}\frac{\partial u}{\partial x} + \frac{dy}{dt}\frac{\partial u}{\partial y} + \frac{dz}{dt}\frac{\partial u}{\partial z}\right)$$
$$= (\rho + \delta\rho)\left(\frac{\partial u}{\partial t} + u\frac{\partial u}{\partial x} + v\frac{\partial u}{\partial y} + w\frac{\partial u}{\partial z}\right).$$

Now since u and $\delta\rho$ are small, we can ignore higher order terms to get

$$\rho \frac{Du}{Dt} \to \rho \frac{\partial u}{\partial t}.$$

Finally, if we assume that initially pressure, p, is only a function of z, then

$$\frac{\partial (p + \delta p)}{\partial x} = \frac{\partial \delta p}{\partial x}.$$

This yields Eq. 8 in Chandrasekhar for the **x-component of momentum**:

$$\rho \frac{\partial u}{\partial t} = -\frac{\partial \delta p}{\partial x} + \mu \nabla^2 u + \frac{d\mu}{dz}\left(\frac{\partial w}{\partial x} + \frac{\partial u}{\partial z}\right) \tag{2.10}$$

Similarly, it can be shown that the equations for the **y- and z-components of momentum** are:

$$\rho \frac{\partial v}{\partial t} = -\frac{\partial \delta p}{\partial y} + \mu \nabla^2 v + \frac{d\mu}{dz}\left(\frac{\partial w}{\partial y} + \frac{\partial v}{\partial z}\right) \tag{2.11}$$

$$\rho\frac{\partial w}{\partial t} = -\frac{\partial \delta p}{\partial z} + \mu\nabla^2 w + 2\frac{d\mu}{dz}\frac{\partial w}{\partial z} - g\delta\rho \tag{2.12}$$

A final condition we need is that the density of every particle remains unchanged as we follow its motion, a condition expressed as Eq. 12 in Chandrasekhar:

$$\frac{\partial}{\partial t}\delta\rho = -w\frac{d\rho}{dz} \tag{2.13}$$

These four equations, along with the condition for incompressibility, $\frac{\partial u}{\partial x} + \frac{\partial v}{\partial y} + \frac{\partial w}{\partial z} = 0$, make up the basic equations that needed to model Rayleigh-Taylor instabilities.

2.1.5 Decomposing the Disturbance into Normal Modes

To summarize, we are considering a flow, initially static, arising at the interface between two layers of material of differing densities, where there are small perturbations to the velocity, density and pressure. In this 2-D analysis, the density and pressure are functions of z only, and we are considering disturbances as small periodic waves propagating along the $z = 0$ plane (the interface between the two material layers). We seek solutions whose dependence on x, y and t are given by:

$$\exp(ik_x x + ik_y y + nt)$$

where k_x, k_y, and n are constants. Then

$$\rho = \rho_0(z) + \rho_1(z)\exp(ik_x x + ik_y y + nt)$$

$$\delta\rho = \rho_1(z)\exp(ik_x x + ik_y y + nt)$$

$$p = p_0(z) + p_1(z)\exp(ik_x x + ik_y y + nt)$$

$$\delta p = p_1(z)\exp(ik_x x + ik_y y + nt)$$

$$u = u_1(z)\exp(ik_x x + ik_y y + nt)$$

$$v = v_1(z)\exp(ik_x x + ik_y y + nt)$$

$$w = w_1(z)\exp(ik_x x + ik_y y + nt).$$

Here $\rho_0 \gg \rho_1$ and $p_0 \gg p_1$, and n represents the growth with time. Substituting these solutions into Eq. 2.10 yields

$$n\rho u = -ik_x\delta p + \mu\left(-k^2 u + D^2 u\right) + D\mu\left(ik_x w + Du\right)$$

where $D \equiv \frac{d}{dz}$ is an operator and $k^2 = k_x^2 + k_y^2$. Rearranging terms yields Eq. 14 of Chandrasekhar:

$$ik_x\delta p = -n\rho u + \mu\left(D^2 - k^2\right)u + (D\mu)\left(ik_x w + Du\right). \tag{2.14}$$

Similarly, Eqs. 2.11 - 2.13 become

$$ik_y\delta p = -n\rho v + \mu\left(D^2 - k^2\right)v + (D\mu)\left(ik_y w + Dv\right) \tag{2.15}$$

$$D\delta p = -n\rho w + \mu\left(D^2 - k^2\right)w + 2(D\mu)(Dw) - g\delta\rho \tag{2.16}$$

$$ik_x u + ik_y v = -Dw \tag{2.17}$$

$$n\delta\rho = -wD\rho. \tag{2.18}$$

Multiplying Eqs. 2.14 and 2.15 by ik_x and ik_y, respectively, adding, and then using equation 2.17, yields

$$k^2\delta p = [-n\rho + \mu(D^2 - k^2)]Dw + (D\mu)(D^2 + k^2)w. \tag{2.19}$$

Combining Eqs. 2.16 and 2.18 yields

$$D\delta p = -n\rho w + \mu(D^2 - k^2)w + 2(D\mu)(Dw) + \frac{g}{n}(D\rho)w. \tag{2.20}$$

Finally, eliminating δp from Eqs. 2.19 and 2.20 allows us to obtain our required equation of motion (which is Eq. 22 in Chandrasekhar):

$$\begin{aligned} &D\left\{\left[\rho - \frac{\mu}{n}(D^2 - k^2)\right]Dw - \frac{1}{n}(D\mu)(D^2 + k^2)w\right\} \\ &\quad = k^2\left\{-\frac{g}{n^2}(D\rho)w + \left[\rho - \frac{\mu}{n}(D^2 - k^2)\right]w - \frac{2}{n}(D\mu)Dw\right\} \end{aligned} \tag{2.21}$$

2.1.6 The Inviscid Case: $\mu = 0$

The Case of Two Uniform Fluids of Densities ρ_1 and ρ_2 Separated by a Horizontal Boundary at $z = 0$:

As a starting point, consider the limiting case where the fluid is inviscid. Eq. 2.21 then becomes

$$D(\rho Dw) - \rho k^2 w = -g\frac{k^2}{n^2}(D\rho)w \tag{2.22}$$

If we consider the fluid to be contained between two rigid planes then the boundary conditions are

$$w = 0 \text{ and } Dw = 0 \tag{2.23}$$

on the bounding surfaces.

Within each fluid, Eq. 2.22 reduces to:

$$\rho(D^2 - k^2)w = -g\frac{k^2}{n^2}(0)w$$

or

$$(D^2 - k^2)w = 0. \tag{2.24}$$

This has the general solution

$$w = Ae^{+kx} + Be^{-kx}. \tag{2.25}$$

To keep the solutions physical, we need $w \to 0$ as $z \to +\infty$ in the upper fluid and as $z \to -\infty$ in the lower fluid. Therefore, for $z > 0$,

$$w_2 = Ae^{-kz}, \tag{2.26}$$

and for $z < 0$,

$$w_1 = Ae^{+kz}. \tag{2.27}$$

Note that the same constant A is used in both equations to allow for continuity of w across the interface. On the boundary, all three components of velocity (u, v and w) must be continuous to maintain a solution that is physical. Also, the tangential viscous stresses must be continuous. The continuity of u and v in conjunction with Eq. 2.17, implies that Dw must be continuous across the boundary.

Having developed a solution within each of the fluid layers, we now need to find solutions that are consistent along the boundary at $z = 0$. The condition that tangential viscous stresses must be continuous leads Chandrasekhar to conclude that $\mu(D^2 + k^2)w$ must be continuous across the interface (Eq. 35 of Chandrasekhar). If we consider the equation

$$D(\rho Dw) - \rho k^2 w = -g\frac{k^2}{n^2}(D\rho)w$$

and apply it to an infinitesimal region of thickness $\triangle z$ that includes the boundary, we find

$$\frac{[\rho(Dw)]_2 - [\rho(Dw)]_1}{\triangle z} - \rho k^2 w = -g\frac{k^2}{n^2}\frac{\rho_2 - \rho_1}{\triangle z}w.$$

Multiplying by $\triangle z$ we find

$$[\rho(Dw)]_2 - [\rho(Dw)]_1 - \rho k^2 w \triangle z = -g\frac{k^2}{n^2}(\rho_2 - \rho_1)w,$$

and taking the limit as $\triangle z \to 0$, we get

$$\rho_2(Dw)_2 - \rho_1(Dw)_1 = -g\frac{k^2}{n^2}(\rho_2 - \rho_1)w_0,$$

where w_0 takes on a fixed value at the interface to allow for continuity across the boundary. This yields Eq. 49 of Chandrasekhar [with T set to zero since we are not considering surface tension forces]:

$$\triangle(\rho Dw) = -g\frac{k^2}{n^2}(\rho_2 - \rho_1)w_0. \tag{2.28}$$

For solutions 2.26 and 2.27, we need to consider Dw as $z \to 0$ at the interface. For the solution corresponding to $z > 0$ $Dw = -kAe^{-kz} \to -kA$; and for $z < 0$ $Dw = +kAe^{+kz} \to +kA$. Now using the condition specified in Eq. 2.28 we find

$$\triangle(\rho Dw) = \rho_2(-kA) - \rho_1(+kA)$$

$$= -kA(\rho_1 + \rho_2) = -g\frac{k^2}{n^2}(\rho_2 - \rho_1)A$$

$$\Rightarrow \boxed{n^2 = gk\frac{(\rho_2 - \rho_1)}{(\rho_2 + \rho_1)}}.$$

If we now define

$$\alpha_1 \equiv \frac{\rho_1}{\rho_1 + \rho_2},\ \alpha_2 \equiv \frac{\rho_2}{\rho_1 + \rho_2},\ \alpha_1 + \alpha_2 = 0,$$

then:

$$\boxed{n^2 = gk(\alpha_2 - \alpha_1)} \tag{2.29}$$

This is the dispersion relation for the inviscid case, with vanishing surface tension. We can see from Eq. 2.29 that the growth rate in time, n, is largest when k is large, and therefore λ is small. Also, $n^2 > 0$, and therefore has a solution that increases with time, when $\rho_2 > \rho_1$. This is the case when we have a denser fluid on top of a lighter fluid. Otherwise, the growth rate is imaginary, and the layers oscillate with time as a surface wave.

2.1.7 The Viscid Case

Two Viscous Fluids with Densities ρ_1 and ρ_2 Separated by a Horizontal Boundary at $z = 0$

Now we generalize the previous discussion for two layers of material with respective densities, ρ_1 and ρ_2, and viscosities, μ_1 and μ_2, with a horizontal interface at $z = 0$. Ignoring surface tension T_s again leads to the equation of motion given by Eq. 2.21.

Within each region of constant ρ and μ, Eq. 2.21 becomes

$$D\left[\rho - \frac{\mu}{n}(D^2 - k^2)\right] Dw = k^2\left[\rho - \frac{\mu}{n}(D^2 - k^2)\right] w \tag{2.30}$$

Noting that ρ and μ are constants within each layer and defining the **coefficient of kinematic viscosity** to be

$$\boxed{\nu \equiv \frac{\mu}{\rho}} \tag{2.31}$$

we get

$$\left[1 - \frac{\nu}{n}(D^2 - k^2)\right](D^2 - k^2)w = 0 \tag{2.32}$$

The general solution to this equation is a linear combination of $e^{\pm kz}$ *and* $e^{\pm qz}$ where $q^2 = k^2 + n/\nu$. In order for the equation to remain physical, we need $w \to 0$ as $z \to -\infty$ in the lower fluid, and $z \to +\infty$, in the upper fluid. The appropriate solutions are:

$$w_1 = A_1 e^{+kz} + B_1 e^{q_1 z}\ (z \leq 0) \tag{2.33}$$

and

$$w_2 = A_2 e^{-kz} + B_2 e^{-q_2 z}\ (z \geq 0), \tag{2.34}$$

where A_1, B_1, A_2 and B_2 are constants of integration and

$$q_1 \equiv \sqrt{k^2 + n/\nu_1}\ \text{ and }\ q_2 \equiv \sqrt{k^2 + n/\nu_2}. \tag{2.35}$$

Note that q_1 and q_2 are defined such that their real part is positive.

We can now perform a similar analysis as that done for the inviscid case. Again we require u, v, w, Dw and $\mu(D^2 + k^2)w$ are continuous across the boundary at $z = 0$. The general solution for this set of equations is given by solving Eq. 113 of Chandrasekhar:

$$-\left[\frac{gk}{n^2}(\alpha_1 - \alpha_2) + 1\right](\alpha_2 q_1 + \alpha_1 q_2 - k)$$
$$-4k\alpha_1\alpha_2 + \frac{4k^2}{n}(\alpha_1\nu_1 - \alpha_2\nu_2)\left\{(\alpha_2 q_1 - \alpha_1 q_2) + k(\alpha_1 - \alpha_2)\right\}$$

$$+\frac{4k^3}{n^2}(\alpha_1\nu_1 - \alpha_2\nu_2)^2(q_1 - k)(q_2 - k) = 0. \tag{2.36}$$

Eq. 2.36 is the required characteristic equation for n.

Two Viscous Fluids with Densities ρ_1 and ρ_2 Separated by a Horizontal Boundary at $z = 0$ Where $\nu_1 = \nu_2$

If the viscosities of the two layers are equal, then $q_1 = q_2 = \sqrt{k^2 + n/\nu} = q$ and Eq. 2.36 becomes

$$\begin{aligned} -\left\{\frac{gk}{n^2}(\alpha_1 - \alpha_2) + 1\right\}(q(\alpha_2 + \alpha_1) - k) - 4k\alpha_1\alpha_2 \\ +\frac{4k^2\nu}{n}(\alpha_1 - \alpha_2)\{q(\alpha_2 - \alpha_1) - k(\alpha_2 - \alpha_1)\} \\ +\frac{4k^3\nu^2}{n^2}(\alpha_1 - \alpha_2)^2(q - k)^2 = 0. \end{aligned} \tag{2.37}$$

Simplifying, and noting that $(\alpha_1 + \alpha_2) = 1$, we get:

$$\begin{aligned} -\left\{\frac{gk}{n^2}(\alpha_1 - \alpha_2) + 1\right\}(q - k) - 4k\alpha_1\alpha_2 \\ -\frac{4k^2\nu}{n}(\alpha_1 - \alpha_2)^2(q - k) \\ +\frac{4k^3\nu^2}{n^2}(\alpha_1 - \alpha_2)^2(q - k)^2 = 0. \end{aligned} \tag{2.38}$$

If we now define

$$Q = \frac{g}{k^3\nu^2} \text{ and } y = \frac{q}{k} = \left(\sqrt{1 + n/k^2\nu}\right), \tag{2.39}$$

then

$$k = \left(\frac{g}{Q\nu^2}\right)^{\frac{1}{3}} \tag{2.40}$$

and

$$n = k^2\nu(y^2 - 1) = \left(\frac{g^2}{\nu}\right)^{1/3}\frac{y^2 - 1}{Q^{2/3}}. \tag{2.41}$$

Then Eq. 2.38 reduces to

$$y^4 + 4\alpha_1\alpha_2 y^3 + 2(1 - 6\alpha_1\alpha_2)y^2 - 4(1 - 3\alpha_1\alpha_2)y$$

$$+(1 - 4\alpha_1\alpha_2) + Q(\alpha_1 - \alpha_2) = 0. \tag{2.42}$$

Only if $\alpha_2 > \alpha_1$ can n be real and positive so that the disturbance **will grow exponentially with time. This arrangement is therefore formally unstable, for disturbances of all wavenumbers, k.**

The relationship between n and k, determined through Eq. 2.42 is complicated, but simplifies in two limits. In the first, as $y \to \infty$, $Q \to y^4/(\alpha_2 - \alpha_1)$. By Eqs. 2.40 and 2.41, we get that:

$$k \to \left(\frac{g}{\nu^2}\right)^{1/3} y^{-4/3}(\alpha_2 - \alpha_1)^{1/3}, \tag{2.43}$$

and

$$n \to \left(\frac{g^2}{\nu}\right)^{1/3} y^{-2/3}(\alpha_2 - \alpha_1)^{2/3} \tag{2.44}$$

and finally we get the dispersion relation for n and k as $y \to \infty$

$$\boxed{n^2 \to g(\alpha_2 - \alpha_1)k \ \text{ as } \ (k \to 0)} \tag{2.45}$$

Note, that as $k \to 0$ and therefore $\lambda \to \infty$ it is clear that the system acts as if there were no viscosity. This makes sense as we would expect that viscosity would play very little role for disturbances of very long wavelengths, over which velocity shear is minimized.

Next, we consider the case where $k \to \infty$ (in the short wavelength limit as $\lambda \to 0$). This case requires $y = q/k \to 1$. In this case it can be shown that $Q \to 4(y-1)/(\alpha_2 - \alpha_1)$. In this case the dispersion relation becomes

$$\boxed{n \to \frac{g(\alpha_2 - \alpha_1)}{2k\nu} \ \text{ as } \ (k \to \infty)} \tag{2.46}$$

Note that for both of these solutions n approaches 0 as $(k \to \infty)$ and $(k \to 0)$. Since n is always real and positive, **there must be an intermediate-wavelength mode of maximum instability for the system.**

Using values appropriate for a KBO similar to Charon, the Fig. 2.3 shows the relationship between the wavelength of the disturbance λ, and the exponential growth factor n, for the disturbance (where ν_1 assumed to be equal to ν_2).

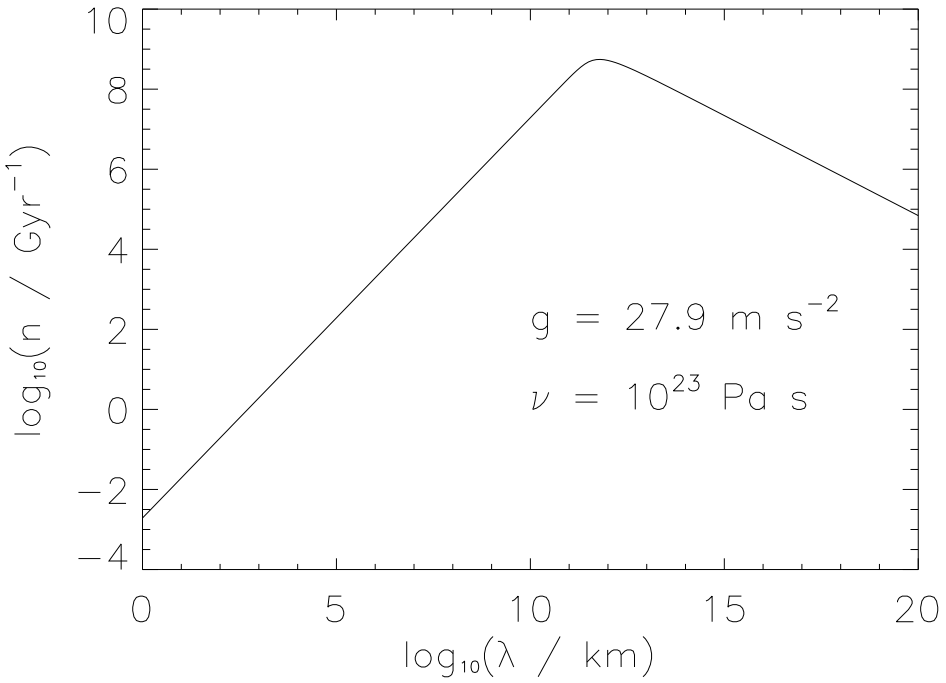

Figure 2.3: Growth rate n vs. wavelength of disturbance λ. Note that the wavelength for the maximum disturbance is on the order of 10^{12} km. The radius of Charon is about 6×10^2 km. Clearly, RT instabilities on KBOs operate in the regime where $k \gg k_{\max}$, the regime where Eq. 2.46 applies.

Two Viscous Fluids with Densities ρ_1 and ρ_2 Separated by a Horizontal Boundary at $z = 0$ Where $\nu_1 \neq \nu_2$

The most general case I consider is where both the densities and viscosities of the two layers are unequal. This case is not explicitly considered in Chandrasekhar's work, so I'd like to approach the problem in a slightly different way. In the limit as $k \to \infty$ (small wavelength regime) $n/k^2\nu_1$ must be small, allowing one to apply the binomial approximation to get

$$q_1 = \sqrt{k^2 + k/\nu_1} = k\left(1 + \frac{n}{k^2\nu_1}\right)^{1/2}$$

$$\approx k\left(1 + \frac{1}{2}\frac{n}{k^2\nu_1}\right) = k + \frac{1}{2}\frac{n}{k\nu_1}.$$

Plugging this result into Eq. 2.36 we find

$$-\left\{\frac{gk}{n^2}\left[(\alpha_1 - \alpha_2)\right] + 1\right\}\left\{\alpha_2\left(k + \frac{n}{2k\nu_1}\right) + \alpha_1\left(k + \frac{n}{2k\nu_2}\right) - k\right\}$$

$$-4k\alpha_1\alpha_2 + \frac{4k^2}{n}(\alpha_1\nu_1 - \alpha_2\nu_2)\left\{\alpha_2\left(k + \frac{n}{2k\nu_1}\right) - \alpha_1\left(k + \frac{n}{2k\nu_2}\right) + k(\alpha_1 - \alpha_2)\right\}$$

$$+\frac{4k^3}{n^2}(\alpha_1\nu_1 - \alpha_2\nu_2)^2\left(k + \frac{n}{2k\nu_1} - k\right)\left(k + \frac{n}{2k\nu_2} - k\right) = 0. \tag{2.47}$$

Simplifying, and noting that $(gk/n^2)(\alpha_1 - \alpha_2) + 1 \approx (gk/n^2)(\alpha_1 - \alpha_2)$ for large k yields

$$-\frac{gk}{n^2}(\alpha_1 - \alpha_2)\frac{n}{2k}\left(\frac{\alpha_2}{\nu_1} + \frac{\alpha_1}{\nu_2}\right) - 4k\alpha_1\alpha_2 + \frac{4k^2}{n}(\alpha_1\nu_1 - \alpha_2\nu_2)\frac{n}{2k}\left(\frac{\alpha_2}{\nu_1} - \frac{\alpha_1}{\nu_2}\right)$$
$$+ \frac{4k^3}{n^2}(\alpha_1\nu_1 - \alpha_2\nu_2)^2\frac{n^2}{4k^2}\left(\frac{1}{\nu_1\nu_2}\right) = 0. \tag{2.48}$$

Further simplification yields

$$n = \frac{g}{2k}(\alpha_2 - \alpha_1)\left(\frac{\alpha_2}{\nu_1} + \frac{\alpha_1}{\nu_2}\right)\left[4\alpha_1\alpha_2 - 2(\alpha_1\nu_1 - \alpha_2\nu_2)\left(\frac{\alpha_2}{\nu_1} - \frac{\alpha_1}{\nu_2}\right) - \frac{(\alpha_1\nu_1 - \alpha_2\nu_2)^2}{\nu_1\nu_2}\right]^{-1}, \tag{2.49}$$

and the quantity on the RHS in brackets becomes:

$$= \left[\frac{\left(\alpha_1\nu_1 + \alpha_2\nu_2\right)^2}{\nu_1\nu_2} \right]^{-1}.$$

Therefore

$$n = \frac{g}{2k}(\alpha_2 - \alpha_1)\left(\frac{\alpha_2}{\nu_1} + \frac{\alpha_1}{\nu_2}\right)\frac{\nu_1\nu_2}{\left(\alpha_1\nu_1 + \alpha_2\nu_2\right)^2}, \tag{2.50}$$

and we finally get the new dispersion relation for the regime where $(k \to \infty)$:

$$\boxed{n \to \frac{g(\alpha_2 - \alpha_1)}{2k}\frac{1}{\alpha_1\nu_1 + \alpha_2\nu_2} \text{ as } k \to \infty}. \tag{2.51}$$

This final equation describes the situation where $\nu_1 \neq \nu_2$. If we compare this with Eq. 2.46 for the case where $\nu_1 = \nu_2$, we find that they are nearly identical except that ν is replaced by $\alpha_1\nu_1 + \alpha_2\nu_2$ in Eq. 2.51.

2.1.8 Effective Viscosity of a Mixture of Ice and Rock

The quantity $\alpha_1\nu_1 + \alpha_2\nu_2$ in Eq. (2.51) can be considered an effective viscosity replacing the kinematic viscosity, ν, in Eq. (2.46).

$$\alpha_1\nu_1 + \alpha_2\nu_2 = \left(\frac{\rho_1}{\rho_1 + \rho_2}\right)\frac{\eta_1}{\rho_1} + \left(\frac{\rho_2}{\rho_1 + \rho_2}\right)\frac{\eta_2}{\rho_2} = \frac{\eta_1 + \eta_2}{\rho_1 + \rho_2} \tag{2.52}$$

Based on the work of Friedson & Stevenson (1983), the viscosity of a mixture of ice and rock is equal to the viscosity of the ice enhanced by a factor of $f(\phi)$ where

$$f(\phi) \equiv 1 + 2.5\phi + 10.06\phi^2 + 0.00273\exp(16.6\phi) \tag{2.53}$$

and ϕ is defined to be the volume fraction of rock particles in the ice. To determine ϕ we need to first find the mass fraction of the rock particles in the ice, f_{rock}, where

$$f_{\text{rock}} = \left(\frac{\rho_{\text{rock}}}{\bar{\rho}}\right)\frac{\bar{\rho} - \rho_{\text{ice}}}{\rho_{\text{rock}} - \rho_{\text{ice}}}. \tag{2.54}$$

and then

$$\phi = f_{\text{rock}}\frac{\bar{\rho}}{\rho_{\text{rock}}}, \tag{2.55}$$

and finally we get

$$\eta_{\text{ice/rock mixture}} = \eta_{\text{ice}} \times f(\phi). \tag{2.56}$$

Combining Eqs. 2.52 and 2.56 results in

$$\alpha_1\nu_1 + \alpha_2\nu_2 = \eta_1 \left(\frac{1 + f(\phi)}{\rho_1 + \rho_2} \right) = \eta_{\text{ice}} \left(\frac{1 + f(\phi)}{\rho_{\text{ice}} + \bar{\rho}} \right) \tag{2.57}$$

This result can be folded into Eq. 2.51 to get

$$n \to \frac{g\,(\alpha_2 - \alpha_1)}{2\,k\,\eta_{\text{ice}}} \left(\frac{\rho_{\text{ice}} + \bar{\rho}}{1 + f(\phi)} \right) \quad \text{as} \quad k \to \infty, \tag{2.58}$$

Noting that

$$\alpha_2 - \alpha_1 = \frac{\rho_2 - \rho_1}{\rho_1 + \rho_2} = \frac{\bar{\rho} - \rho_{\text{ice}}}{\rho_{\text{ice}} + \bar{\rho}},$$

Eq. 2.57 simplifies to

$$\boxed{n \to \frac{g\,(\bar{\rho} - \rho_{\text{ice}})}{2\,k\,\eta_{\text{ice}}\,(1 + f(\phi))} \quad \text{as} \quad k \to \infty}, \tag{2.59}$$

which replaces Eq. 2.51. Since $k \equiv 2\pi/\lambda$, then Eq. 2.59 can be rewritten in terms of λ to get

$$\boxed{n \to \frac{\lambda\, g\,(\bar{\rho} - \rho_{\text{ice}})}{4\pi\,\eta_{\text{ice}}\,(1 + f(\phi))}}, \tag{2.60}$$

when λ is small.

2.2 Determination of Critical Viscosities for Overturn

In the previous discussion I determined a relationship between the density and viscosity of two superposed fluids, and the growth rate of a disturbance as it propagates along the boundary between these two layers. So I am now in a position to evaluate the original question. We have two layers of material, the outer, a crust consisting of an undifferentiated mixture of rock and ice, and the inner, a pure water ice mantle. Since the outer layer has a higher density than the inner one, it is gravitationally unstable and may eventually overturn. I would like to determine under what conditions this will occur.

Eq. 2.60 clearly shows that the growth rate of a disturbance is inversely proportional to the ice viscosity $\eta_{\rm ice}$ and the related viscosity of the overlying crust. If the viscosities are too high, the layers will not overturn on geologically relevant timescales. To be conservative, I consider a small disturbance such as a pocket of frozen brine or a diapir, with an initial amplitude of $1 - 10$ km. For the largest disturbance in that range of 10 km, if the disturbance is able to grow by a factor of 10 over some relevant time period τ, I assume that it can overturn a crust with a thickness ≤ 100 km.

The viscosity of the ice/rock mixture is in turn related to its temperature, with higher temperatures resulting in lower viscosities. Therefore, the time period τ over which the boundary layer between the ice mantle and crust can overturn must be comparable to the time it remains at its maximum temperature. With these considerations in mind, I arbitrarily assume that the layers will mix, overturning the crust, if a disturbance is able to grow by a factor of 10 over this time period τ. Remembering that the growth rate, n, is an exponential factor, this condition is equivalent to

$$n > n_{\rm crit} = \frac{\ln 10}{\tau}. \tag{2.61}$$

For $n > n_{\rm crit}$, it is assumed that the layers will overturn. For comparison, if we require that the instability must grow by a factor of 100 to overturn the crust, then $n_{\rm crit}$ increases by a factor of 2. From Eq. 2.60 we know that for small λ

$$n \approx \frac{\lambda\, g\, (\bar{\rho} - \rho_{\rm ice})}{4\pi\, \eta_{\rm ice}\, (1 + f(\phi))};$$

therefore, the growth rate n corresponding to overturn is

$$n = \frac{\lambda\, g\, (\bar{\rho} - \rho_{\rm ice})}{4\pi\, \eta_{\rm ice}\, (1 + f(\phi))} > n_{\rm crit} = \frac{\ln 10}{\tau}, \tag{2.62}$$

and the ice viscosity corresponding with $n_{\rm crit}$ is

$$\frac{\lambda\, g\, (\bar{\rho} - \rho_{\rm ice})}{4\pi\, n_{\rm crit}\, (1 + f(\phi))} > \eta_{\rm ice} \equiv \eta_{\rm crit}. \tag{2.63}$$

So the condition for overturn of the crust is that $\eta_{\rm ice} < \eta_{\rm crit}$. The most generous conditions for overturn are those with small n/large τ and large λ. The largest λ physically possible is the radius of the planet, $R_{\rm p}$, and the largest τ depends on how long we can keep the boundary layer at a temperature high enough to keep the viscosity below $\eta_{\rm crit}$.

2.2.1 Application of Equal Viscosity Case to a Charon-like Object

To give a concrete example of how one can apply the previous discussion on Rayleigh-Taylor instabilities, consider the case of Pluto's moon, Charon. Assuming a radius $R_{\rm p} = 600$ km, and a mean density $\bar{\rho}_{\rm Charon} = 1.65\,{\rm g\,cm^{-3}}$, it can serve as a typical example of the type of icy body found in the Kuiper belt. Applying the models of Desch et al. (2009) (which will be discussed more fully in Chapter 4) to the case of Charon, we find that a given shell of material near the ice/crust boundary will generally stay within 10 K of its maximum temperature for 1.5 Gyr. This defines the time period τ over which overturn must occur. Only within this time period are the temperature high enough and the viscosities low enough too support conditions for overturn. Thus $n_{\rm crit} = \ln(10)/1.5\,{\rm Gyr} = 4.86 \times 10^{-17}\,{\rm s^{-1}}$.

For the case of Charon, the ice mantle has a density of $\rho_1 = \rho_{\rm ice} = 0.935\,{\rm g\,cm^{-3}}$, and the superposed undifferentiated crust has a density on the order of the mean density of Charon, $\bar{\rho}_{\rm Charon} = 1.65\,{\rm g\,cm^{-3}}$. The surface gravity for a body the size of Charon is of $g = 0.277\,{\rm m\,s^{-2}}$. If we assume a mean density for the rocky component of $\rho_{\rm rock} = 3.25\,{\rm g\,cm^{-3}}$, then Eq. 2.54 implies that $f_{\rm rock} = 0.608$, Eq. 2.55 implies that $\phi = 0.309$, and Eq. 2.53 implies that $f(\phi) = 3.19$. Finally, as discussed in 2.2, the most generous condition for overturn is if $\lambda = R_{\rm p} = 600$ km. Thus the critical

viscosity will be

$$\eta_{\rm crit} = \frac{\lambda\, g\, (\bar{\rho} - \rho_{\rm ice})}{4\pi\, n_{\rm crit}\, (1 + f(\phi))} = 4.63 \times 10^{22}\,{\rm Pa\,s}. \tag{2.64}$$

If $\eta_{\rm ice} > \eta_{\rm crit}$ then the crust will not be able to overturn over the time period τ.

Alternatively, if we assume that the density of the rocky component $\rho_{\rm rock} = 2.35\,{\rm g\,cm^{-3}}$, then $f_{\rm rock} = 0.719$, $\phi = 0.505$, and $f(\phi) = 16.82$. This results in a new critical viscosity of $1.089 \times 10^{22}\,{\rm Pa\,s}$.

Chapter 3

NON-NEWTONIAN ICE RHEOLOGY

3.1 Overview

Icy bodies are ubiqitous in the outer solar system, including many of the moons of Jupiter and Saturn, Pluto and Charon, and most of the Kuiper belt objects. They are commonly composed of greater than 50 percent water and water ice by mass (Durham and Stern 2001). When modeling the thermal evolution and differentiation of these objects, it is therefore critical to understand the rheology of ice (Ellsworth and Schubert 1983; Kirk and Stevenson 1987; McKinnon 1998; Mueller and McKinnon 1988; Reynolds and Cassen 1979; Schubert et al. 1981, 1986). In particular, the effect of Rayleigh-Taylor instabilities on the differentiation of icy bodies ultimately depends on how the ice deforms under stress, and therefore on its rheology.

Viscosity (η) is a measure of the ability of a material to flow under stress, and is modeled as the ratio of the strain ($\dot{\varepsilon}$) produced for a given amount of stress (σ): $\eta \propto \sigma/\dot{\varepsilon}$. If stress is applied to a solid body, it will initially respond via an elastic deformation, and then via a viscous deformation or strain. The viscous strain has a viscoelastic component, which can be recovered when the strain is released, and an inelastic component which results in permanent deformations. In the outer shells of icy bodies, large strains are produced under conditions of relatively low stress, acting on geological timescales. Under these conditions, elastic strains are fairly insignificant (Durham and Stern 2001). Additionally, the strains considered in this paper are ductile in nature, which implies that they are volume conservative and allow materials to retain their strength (as opposed to brittle strains).

3.2 The Relationship between Stress and Strain

The relationship between stress and strain in ductile materials is usually modeled by the Levy-Mises equations (Hill 1950) wherein each component of the strain rate tensor, $\dot{\varepsilon}_{ij}$, is proportional to a corresponding component of the the stress tensor, σ'_{ij}

$$\dot{\varepsilon}_{ij} = \lambda \sigma'_{ij}. \tag{3.1}$$

Here σ'_{ij} is a measure of the deviatoric stress, the non-hydrostatic portion of the stress which causes changes to the shape of a material but not its volume. A scalar representation of this flow law is given by

$$\dot{\varepsilon} = A' f(\sigma), \tag{3.2}$$

where σ is an appropriate scalar representation of the state of deviatoric stress and is a function of the geometry of the system. Here, A' represents all of the relevant environmental conditions in the relationship between $\dot{\varepsilon}$ and σ. The steady-state flow of planetary ices can be modeled by a power-law form of the flow law given by

$$\boxed{\dot{\varepsilon} = A \frac{\sigma^n}{d^p} \exp\left(-\frac{Q^* + PV^*}{RT}\right)}, \tag{3.3}$$

where A is a material parameter, σ is the differential stress, n is the stress exponent, d is the grain size, p is the grain size exponent, Q^* is the activation energy for the creep, P is the hydrostatic pressure, V^* is the activation volume for the creep, R is the gas constant, and T is the absolute temperature (Goldsby and Kohlstedt 2001). Note that this functional relationship is indicative of a thermally activated process.

3.2.1 Laboratory Measurements of Rheological Properties of Ice

In 2001 Golsdby and Kohlstedt reported the rheology results of their laboratory experiments on the deformation of ice I. From these experiments they determined a

composite flow law for ice I which is far more comprehensive than previous works in the field. In particular, using extremely small grain sizes allowed them to measure the effects of the grain boundary slip mechanism under laboratory conditions, which had not been possible before.

The experiments involve placing a sample of ice into a cylinder confined under high hydrostatic pressure. The purpose of the confinement is to minimize the effects of brittle fracturing, which are not typical of the more ductile deformation found in planetary environments. A load is applied to the sample via a moving piston at the end of the cylinder. The strain rate is the measured rate of shortening of the cylinder. When measured this way, the stress is referred to as a differential stress. It is experimentally determined as the difference between the maximum stress, σ_1, applied at the ends of the cylinder, and the gas pressure applied to the outside of the sample (Durham et al. 2010). Under this geometry, the relationship of strain to stress is represented by an axisymmetric flow law.

There are two common approaches to experimentally determining the flow law. The first is the "constant displacement rate" experiment in which a strain rate is imposed by the deforming piston, and the dependent variable is the stress required to maintain that rate. The stress is defined as the load divided by the cross-sectional area of the sample. The results of this measurement are typically portrayed in either an Arrhenius plot of $\log \sigma$ vs. inverse temperature, or a plot of $\log \dot{\varepsilon}$ vs. $\log \sigma$. The second approach is the constant stress or"creep" experiment in which the load is prescribed, and the displacement rate required to maintain the load is measured (Durham et al. 2010).

What made the experiments of Goldsby and Kohldstedt unique was their ability to synthesize samples composed of ice crystals with exceedingly small crystal grain sizes (down to $\sim 3\,\mu$m). Since the strain rate in the grain size sensitive flow regime

increases with decreasing grain size, Goldsby and Kohlstedt focused their investigation of grain size sensitive creep mechanisms on fine-grained samples. Thus they were able to observe and quantify the effects of the grain boundary sliding mechanism on ice at the low stresses typical of planetary environments.

3.2.2 Mechanisms of Deformation

On a molecular level, deformation is accomplished through the coordinated motion of crystal defects. Defects can include point defects, such as vacancies and interstitials; line defects such as dislocations; and planar defects along grain or subgrain boundaries. Each of these defects has a unique dependence on the external environmental variables (σ, P and T), and intrinsic variables such as grain size and activation energy for a given process. For a given combination of temperature and stress, all potential mechanisms for deformation are available, and multiple mechanisms can occur simultaneously. Each mode can be represented by its own flow law in the form of Eq. 3.3. However, it is likely that a single mode will dominate the rheology of the ice, and contribute the majority of the strain rate.

Two deformation mechanisms are considered independent if they operate simultaneously such that

$$\dot{\varepsilon}_{\mathrm{tot}} = \dot{\varepsilon}_a + \dot{\varepsilon}_b. \tag{3.4}$$

At a given temperature, the mechanism with the higher stress exponent, n, will dominate at higher levels of stress. In contrast, two mechanisms are considered dependent if mechanisms a and b cannot operate independently. Under these conditions, $(\dot{\varepsilon}_{\mathrm{tot}})^{-1} = (\dot{\varepsilon}_{\mathrm{a}})^{-1} + (\dot{\varepsilon}_{\mathrm{b}})^{-1}$, and $n_b > n_a$ requires that $\dot{\varepsilon}_b < \dot{\varepsilon}_a$ for higher stresses.

According to the experimental work of Goldsby and Kohlstedt (2001), "the constitutive equation for the flow of ice is composed of at least 4 individual flow laws of the form of Eq. 3.3, one each for dislocation creep, GBS-accommodated basal slip

(i.e., "superplastic flow"), basal slip-accommodated GBS, and diffusional flow." In total, the composite strain rate accommodated by all four mechanisms is given by the semi-empirical constitutive equation

$$\boxed{\dot{\varepsilon} = \dot{\varepsilon}_{\text{diff}} + \left(\frac{1}{\dot{\varepsilon}_{\text{basal}}} + \frac{1}{\dot{\varepsilon}_{\text{gbs}}} \right)^{-1} + \dot{\varepsilon}_{\text{disl}}}. \tag{3.5}$$

It is clear in this composite flow law that the grain boundary sliding (GBS) and basal slip (BS) creep regimes must operate dependently, whereas the mechanisms of diffusion and dislocation creep operate independently.

Dislocation creep is a grain size insensitive (GSI) mechanism that occurs through the motion of lattice dislocations. "When a stress of sufficient magnitude is applied to a polycrystalline sample, grains within the sample that are well-oriented for slip deform via dislocation glide." (Durham et al. 2010) These lattice glide dislocations may encounter an obstacle that they need to 'climb' over before the glide can resume. In practical terms, this means that the rate of dislocation creep may be either glide- or climb-limited depending on which process is the slower of the two.

The other three creep mechanisms referenced in Eq. 3.5 are collectively considered grain size sensitive (GSS) as their flow laws have a dependence on grain size, d. In particular, at the lower stresses typical of icy planetary bodies, grain boundary sliding (GBS) mechanisms can dominate the rate of creep in ice. Here, sliding can occur along grain boundaries. This sliding will continue until pressure builds up at the triple junctions. This stress is initially accommodated by elastic deformation. But to maintain a steady state flow, material must be moved away from these junctions via a diffusional or dislocation flow of the material. Therefore, GBS creep cannot occur in isolation, but must act in coordination with other creep mechanisms. Grain boundary slip and basal slip creep must occur together in order to allow deformation to occur. They are dependent mechanisms and their rate is limited by the slower of

the two processes.

Diffusional flow is accomplished by the motion of atoms through vacancies interior to the crystal grain in response to stress applied. In Nabarro-Herring creep, stress drives bulk diffusion within grains in a manner to accommodate the stress. Thus if a vertical compression stress is applied to the grain, atoms will diffuse horizontally and flatten the crystal. Coble creep is a similar diffusional process whereby diffusion occurs along the grain boundaries as opposed to the interior of the grain. Nabarro-Herring creep is also known volume diffusion creep, and Coble creep as grain boundary diffusion creep. For both of these mechanisms there is a linear dependence of stress on strain.

Goldsby and Kohlstedt (2001) experimentally determined the flow laws for all of the mechanisms described in Eq. 3.5, except for diffusional flow, which was out of the range of their experimental techniques; however, they were able to use their experimental data to constrain the parameters for this mechanism. The creep rate due to diffusional flow (Nabarro, 1948; Herring, 1950; Coble, 1963) is given by

$$\dot{\varepsilon} = \frac{42\sigma V_m}{3RTd^2}\left(D_v + \frac{\pi\delta}{d}D_b\right), \tag{3.6}$$

where $D_v = D_{0,v}\exp(-Q/RT)$ and $D_b = D_{0,b}\exp(-Q/RT)$ are the coefficients for volume and grain boundary diffusion, respectively. The parameters that Goldsby and Kohlstedt (2001) used are reproduced in Table 3.1. Note that the very small value for δ implies that the second term relating to D_b can be ignored for all practical purposes.

Table 3.1: Diffusion Creep Parameters

Parameter	Value
Molar volume, V_m	1.97×10^{-5} m^3 mol^{-1}
Preexponential, volume diffusion, $D_{0,v}$	9.10×10^{-4} m^2 s^{-1}
Preexponential, grain boundary diffusion, $D_{0,b}$	$\leq 8.4 \times 10^{-4}$ m^2 s^{-1}
Activation energy, volume diffusion, Q_v	59.4 kJ mol^{-1}
Grain boundary width, δ	9.04×10^{-10} m
Activation energy, boundary diffusion, Q_b	49 kJ mol^{-1}

Constitutive Equation

The flow laws for each of the remaining deformation mechanisms are of the following form

$$\dot{\varepsilon} = A\frac{\sigma^n}{d^p}\exp\left(-\frac{Q+PV}{RT}\right).$$

The parameters that Goldsby and Kohlstedt (2001) experimentally determined for each mechanism are reproduced in Table 3.2.

Table 3.2: Constitutive Equation Parameters

Creep regime	A, units	n	p	Q (kJ/mol)
Dislocation creep[a]	4.0×10^5 MPa$^{-4.0}$ s^{-1}	4.0	0	60
GBS - accomm. basal slip[b, c]	3.9×10^{-3} MPa$^{-1.8}$ m$^{1.4}$ s^{-1}	1.8	1.4	49
BS - accomm. GBS[d]	5.5×10^7 MPa$^{-2.4}$ s^{-1}	2.4	0	60
Volume Diffusion	3.02×10^{-14} MPa^{-1} m^2 s^{-1}	1	2	59.4

[a] $T < 258$ K

[b] $T < 255$ K

[c] GBS = Grain Boundary Sliding

[d] BS = Basal Slip

Note that these parameters were derived from experiments performed with limited grain sizes, d ($.003\,\mathrm{mm} \leq d \leq 0.175\,\mathrm{mm}$), differential pressures, σ ($0.1\,\mathrm{MPa} \leq \sigma < 7\,\mathrm{MPa}$), and temperatures, T ($170\,\mathrm{K} \leq T \leq 273\,\mathrm{K}$). The empirical fits represented by this flow law must be extrapolated to the conditions of low temperature and larger grain sizes appropriate for our models.

3.2.3 Application of the Flow Law

Having developed a flow law that can be applied to the stresses and strains appropriate to our planetary models, we now need to determine what conditions will allow the boundary of the ice mantle to achieve the critical viscosity, η_{crit}, necessary for overturn determined in Chapter 2. As described above, the rheology of ice is highly dependent on the temperature, stress and grain sizes found within the ice shell. In general, the stresses found for planetary ices can vary over many orders of magnitude, and no direct measurements of grain size are possible for icy bodies in the outer solar system. To model the viscosity the ice mantle for a typical icy body, I choose a stress of 1 MPa, with grains sizes on the order of 1 mm. Later in this chapter I consider the case where the stress applied is not known a priori.

Given an average grain size and stress applied, the ice viscosity is critically dependent on temperature and can vary over more than 10 orders of magnitude. In Fig. 3.1 below, I applied the composite flow law of Goldsby and Kohlstedt (2001) to find the relationship between stress and strain over a range of temperatures from 50 to 250 K. The plot assumes a grain size $d = 1\,\mathrm{mm}$. As can be seen in the figure, the lowest temperatures correspond with the largest amount of stress required to produce a given amount of strain. Since $\eta \approx \sigma/\dot{\varepsilon}$ this means that the lowest temperatures correspond with the highest viscosities. A stress of 1 MPa is plotted with a horizontal red line, and the strain rate $\dot{\varepsilon} = 2.11 \times 10^{-17}\,\mathrm{s}^{-1}$ (corresponding to movement over

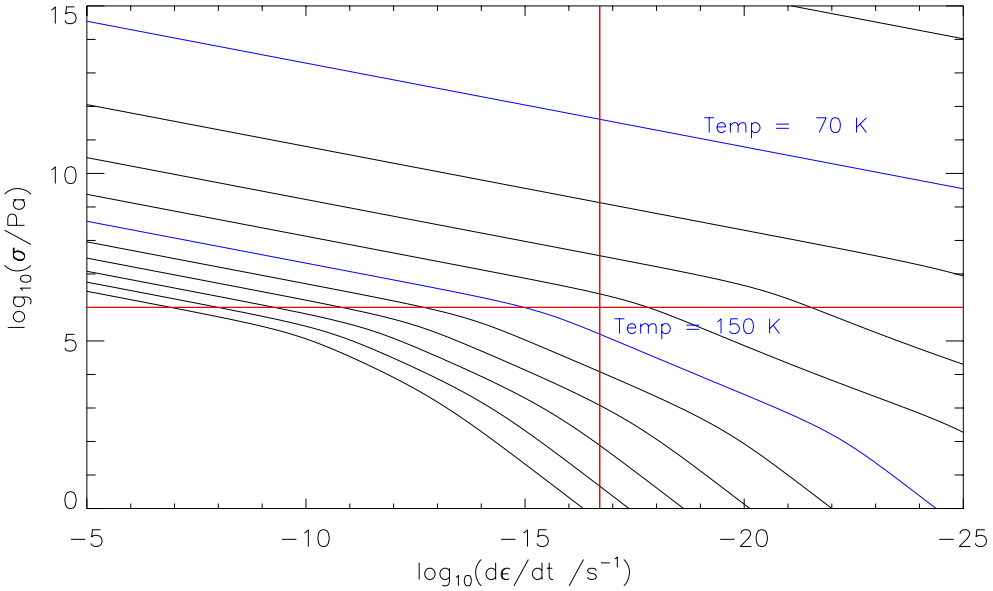

Figure 3.1: The relationship between stress and strain as a function of temperature. This plot shows the relationship between stress and strain for temperatures ranging from $T = 250\,\mathrm{K}$ to $T = 50\,\mathrm{K}$, in 20 degree increments. Two of the temperatures have been highlighted for reference. Note that for a given stress, the strain rate can vary by over 10 orders of magnitude depending on temperature. The horizontal red line demarcates a stress level of 1 MPa and the vertical line shows the strain rate corresponding to movement over 1.5 Gyr.

1.5 Gyr) is plotted with a vertical red line. The temperature contour at which these lines intersect is the temperature at which a stress of 1 MPa can produce a strain rate corresponding to 1.5 Gyr. This temperature is unique and occurs at $\sim$ 135 K. As discussed in section 2.2, this is the strain rate used to determine the critical growth rate n_{crit} required for overturn, and thereby the critical viscosity η_{crit} of the ice mantle. For this set of parameters, when the temperature is at least 135 K, the viscosity of the ice mantle will be $\leq \eta_{\mathrm{crit}} = 4.63 \times 10^{22}\,\mathrm{Pa\,s}$, yielding conditions favorable for overturn of the crust. I define this temperature at the ice mantle/undifferentiated

crust boundary as the differentiation temperature, or more simply just T_{diff}.

Note that the exact functional relationship between stress, strain and viscosity depends on the geometry of the system, and how the stress is applied. For the purposes of this research, I have adopted the definition of effective viscosity given in Barr and Pappalardo (2005)

$$\eta_{\text{eff}} = \frac{\sigma}{2\dot{\varepsilon}_{II}}. \tag{3.7}$$

Here σ is the effective shear stress, and $\dot{\varepsilon}_{II}$ is the second invariant of the strain rate tensor.

One final note, the viscosity calculations above specifically apply to pure water ice. This is appropriate when considering the conditions of the ice mantle where volatiles such as ammonia and ADH have been removed from solution as the ice layer differentiates, forming the pure water ice layer. However, as described in subsection 2.1.8, the viscosity of the ice/rock matrix found in the undifferentiated crust can be directly related to the viscosity of the pure water ice by the factor of $f(\phi)$, which is in turn dependent on the mass fraction of rock particle found in the ice matrix (Friedson & Stevenson 1983).

3.2.4 Sensitivity of Viscosity on Grain Size and Stress

Next, I consider the effect of grain size, d, on the viscosity of the system. In Fig. 3.2, I explore the relationship of viscosity to temperature as a function of grain size. For a fixed stress of $\sigma = 1$ MPa, the temperature required to yield a viscosity of 4.63×10^{22} Pa s is about 140 K for grain sizes of 1 mm and 10 cm. For a grain size of $d = 10^{-2}$ mm, the temperature needs to drop to about 128 K to maintain the same viscosity.

Finally, I consider the effect of stress on the viscosity/temperature relationship for a given grain size. In Fig. 3.3, the grain size is fixed at $d = 1$ mm while the applied

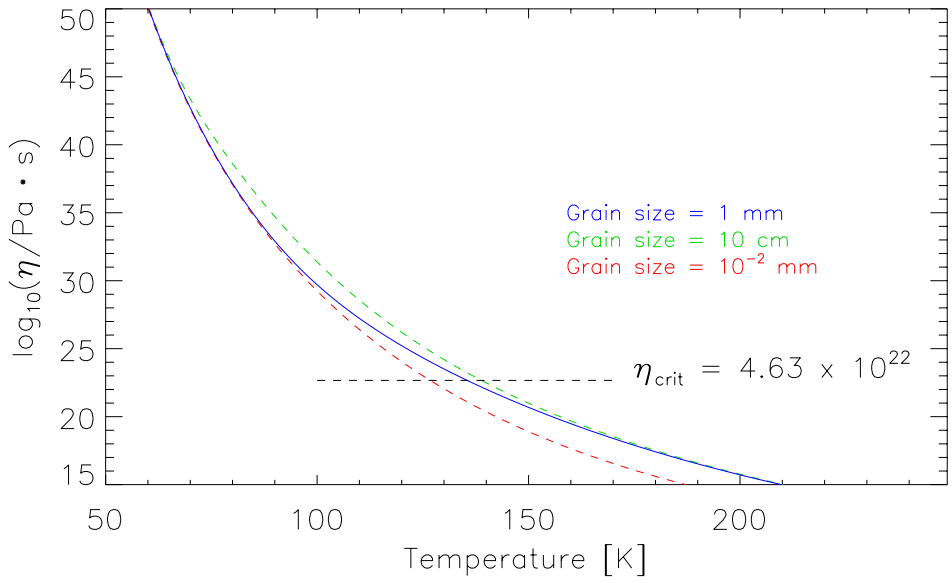

Figure 3.2: The relationship between viscosity and temperature as a function of grain size. In this plot, three different grain sizes have been chosen, ranging from 10^{-2} mm to 10^{2} mm, while maintaining a fixed value for stress of 1 MPa. Although the grain sizes have been allowed to vary over 4 orders of magnitude, their effect on viscosity is limited. The horizontal line corresponds to our critical viscosity, $\eta_{\rm crit} = 4.63 \times 10^{22}$ Pa s.

stress is allowed to vary from 0.1 MPa to 10 MPa. In this plot it can be seen that the minimum temperature required to yield a viscosity of $\eta_{\rm crit} = 4.63 \times 10^{22}$ Pa s varies from about 123 K at a stress of 10 MPa to about 143 K at a stress of 0.1 MPa.

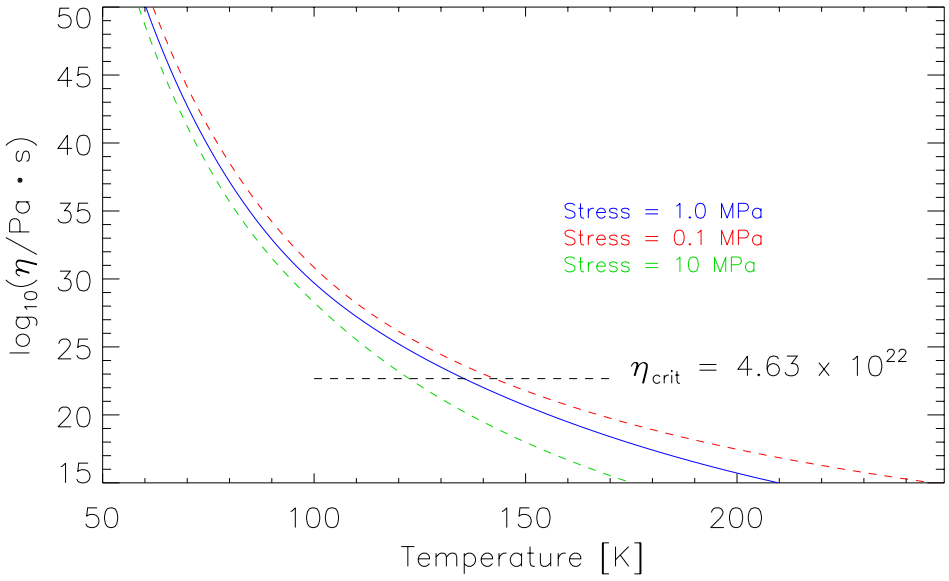

Figure 3.3: The relationship between viscosity and temperature as a function of stress (assuming a grain size, $d = 1\,\mathrm{mm}$).

3.2.5 *Determination of Differentiation Temperature When Stress is Not Known*

It is not possible to know, a priori, what stress (σ) the ice is experiencing at the boundary layer between the ice mantle and crust, because we do not know what process is creating the initial disturbance. It could be a general contraction of the KBO as the body cools and the liquid freezes, or it could be a diapir that forms along the boundary, or some other process not previously considered. Therefore it became clear during the research that it is unwise to assume what value of σ to use in the ice rheology equations. Instead, I decided to focus on a strain rate ($\dot{\varepsilon}$) favorable for overturn. As will be demonstrated in the model simulations discussed in Chapter 5, the boundary layer between the ice mantle and the undifferentiated crust can generally remain within 10 K of the minimum temperature required for overturn ($T_{\rm diff}$) for a period of $\tau \sim 1.5$ Gyr. Given the uncertainties in the model and in particular in the effect of grain size, we allow for the possibility that the process of overturn can begin as long as the layer remains within 10 K of $T_{\rm diff}$. If we are more than 10 K below $T_{\rm diff}$, the viscosity of the ice is simply too high to allow any further differentiation to occur.

Therefore for overturn of the crust to occur, we require that it must complete within $\tau = 1.5$ Gyr. This corresponds with a minimum strain rate required for overturn of $\dot{\varepsilon} = 1/\tau = 2.11 \times 10^{-17}\,\mathrm{s}^{-1}$. This strain rate is the most generous condition for overturn, as it requires the lowest possible differentiation temperature. Over this same time period τ, the critical viscosity required for overturn is $\eta_{\rm crit} = 4.63 \times 10^{22}\,\mathrm{Pa\,s}$ for $\rho_{\rm rock} = 3.25\,\mathrm{g\,cm}^{-3}$, and $\eta_{\rm crit} = 1.089 \times 10^{22}\,\mathrm{Pa\,s}$ for $\rho_{\rm rock} = 2.35\,\mathrm{g\,cm}^{-3}$ based on the linear stability analysis of Chapter 2. Combining these two conditions yields the most generous conditions required for overturn in the model.

Since $\eta_{\rm crit} \equiv \sigma / 2\,\dot{\varepsilon}$, combining $\eta_{\rm crit} = 4.63 \times 10^{22}\,\mathrm{Pa\,s}$ and $\dot{\varepsilon} = 2.11 \times 10^{-17}\,\mathrm{s}^{-1}$

requires that $\sigma = 2.97$ MPa (for $\rho_{\rm rock} = 3.25\,{\rm g\,cm^{-3}}$). Similarly, in the case of more hydrated rocky material where $\rho_{\rm rock} = 2.35\,{\rm g\,cm^{-3}}$, $\eta_{\rm crit} = 1.089 \times 10^{22}\,{\rm Pa\,s}$ and σ must be 0.46 MPa. Again, please note that this is the threshold or critical σ required for overturn. Overturn can occur more quickly for larger values of σ, but this will require higher temperatures as well.

Finally, once σ and $\dot{\varepsilon}$ are known, I applied the composite flow law of Goldsby and Kohlstedt (2001) using a bracketing technique to determine the unique temperature at which this combination of stress and strain can occur. I found that the time period $\tau = 1.5$ Gyr over which the boundary layer between the ice mantle and the undifferentiated crust can sustain temperatures high enough to allow for overturn is fairly consistent across all the model runs. Therefore I chose $\dot{\varepsilon} = 2.11 \times 10^{-17}\,{\rm s^{-1}}$ as my threshold strain rate for all of the models. I also assume a grain size of 1 mm for all of my calculations. Using the bracketing technique mentioned above, I found that the $T_{\rm diff} = 143\,{\rm K}$ when $\eta_{\rm crit} = 1.089 \times 10^{22}\,{\rm Pa\,s}$.

Fig. 3.4, graphically illustrates the methodology I used to determine $T_{\rm diff}$ for the models. The black contours show isotherms of temperature similar to those found in Fig. 3.1. Along these contours the temperature remains constant, but the paired values of σ and $\dot{\varepsilon}$ vary according to the composite flow law of Goldsby and Kohlstedt (2001). A strain rate of $2.11 \times 10^{-17}\,{\rm s^{-1}}$ is highlighted in blue corresponding with our time period τ. As described above, combining this strain rate with $\eta_{\rm crit} = 1.089 \times 10^{22}\,{\rm Pa\,s}$ requires that $\sigma = 0.46$ MPa (which is plotted as a horizontal red line). The thermal contour upon which these lines intersect is $T_{\rm diff}$ for this set of parameters. It can be seen to occur at $T = 143$ K, which is highlighted in red as well.

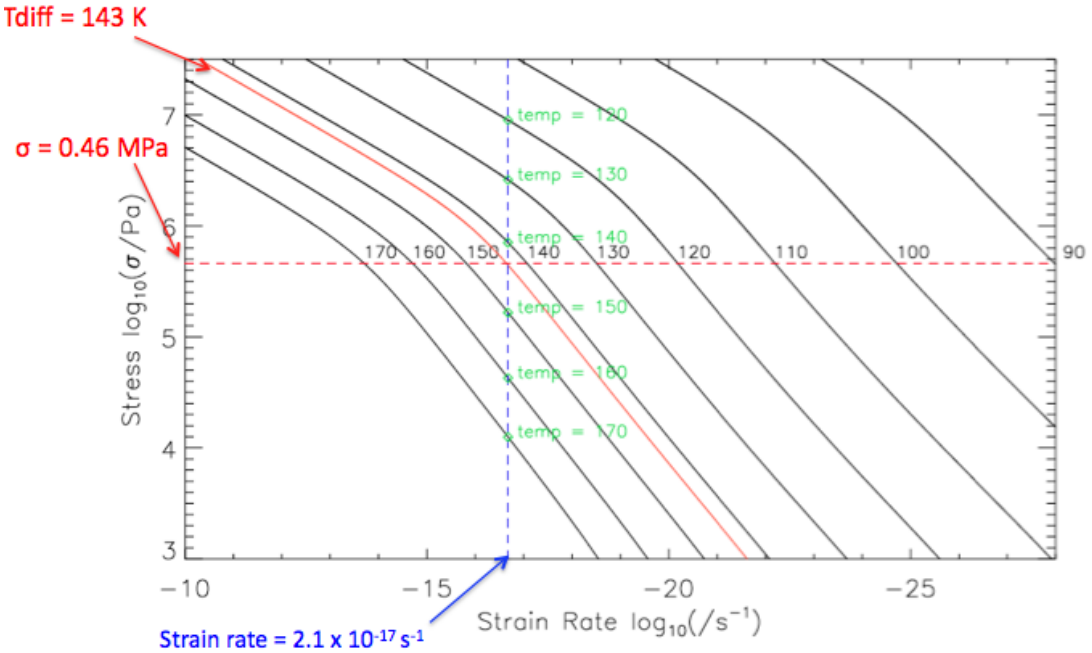

Figure 3.4: The relationship between stress and strain based on the models of Goldsby and Kohlstedt (2001) assuming a fixed grain size $d = 1$ mm. The contours of constant temperature are marked in black. As explained in more detail in the text, combining $\eta_{\rm crit} \equiv \sigma/2\,\dot{\varepsilon} = 1.089 \times 10^{22}$ Pa s, with the threshold strain rate $\dot{\varepsilon} = 2.11 \times 10^{-17}\,{\rm s}^{-1}$ determines a unique stress $\sigma = 0.46$ MPa. The temperature contour at which these values intersect is the differentiation temperature, $T_{\rm diff} = 143$ K.

Fig. 3.5, illustrates the relationship between viscosity and temperature for a fixed strain rate $\dot{\varepsilon} = 2.11 \times 10^{-17}$. Again we see the correlation between the critical viscosity $\eta_{\text{crit}} = 1.089 \times 10^{22}$ Pa s, and the temperature $T_{\text{diff}} = 143$ K required to produce this viscosity.

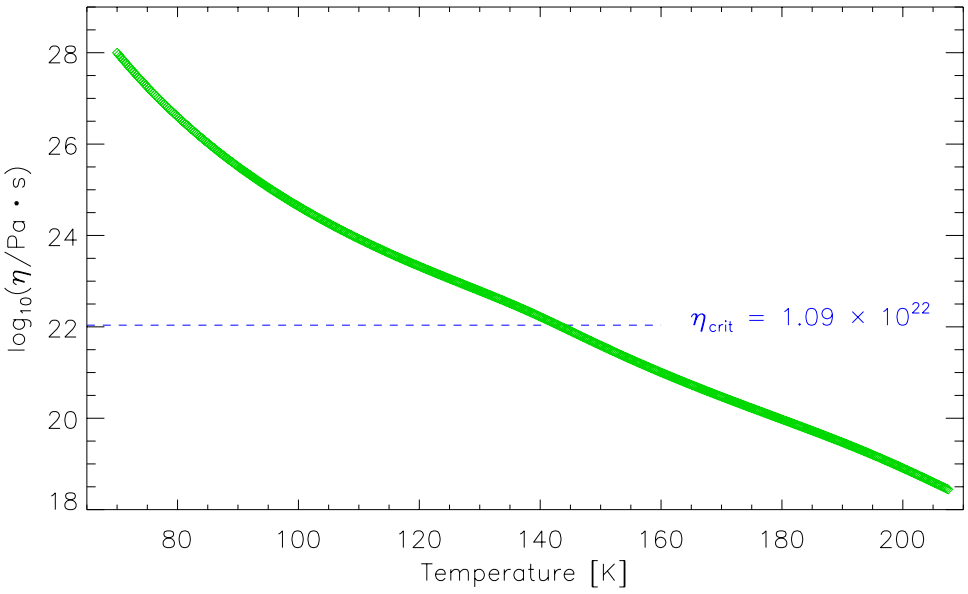

Figure 3.5: The relationship between viscosity and temperature where $\dot{\varepsilon} = 2.11 \times 10^{-17}\,\text{s}^{-1}$ and $d = 1$ mm, based on the composite flow law of Goldsby and Kohlstedt (2001). $\eta_{\text{crit}} = 1.089 \times 10^{22}$ Pa s crosses the curve at $T_{\text{diff}} = 143$ K.

Chapter 4

THERMAL EVOLUTION MODEL OF DESCH ET AL. 2009

4.1 Overview

Here we review the thermal evolution code described by Desch et al. (2009) in "Thermal evolution of Kuiper belt objects, with implications for cryovolcanism." This code was specifically designed to model the thermal evolution of outer solar system icy bodies whose very low surface temperatures ($\ll 100\,\mathrm{K}$) and high water content (near 50% by weight) make them unique in the solar system. The code solves the 1-D (spherical) heat conduction equation while addressing a number of concerns that have not been collectively modeled before. Chief among these is time dependence, as well as the inclusion of the effects of differentiation and ammonia on their thermal evolution. Taken together these considerations indicate that KBOs of sufficient radius can maintain internal liquid water reservoirs to the present day, which is not predicted by static models.

4.2 Description of Model

The code assumes a spherical geometry, evenly dividing the object into N radial zones labelled by index i whose outer radii obey $r_i = R_{\mathrm{p}}(i/N)$, where R_{p} is the KBO radius. At time t, the energy for each zone is calculated to be $E_i(t)$. The model assumes cold accretion; therefore $E_i(0)$ is initially set to an energy corresponding to the surface temperature T_{surf} for all i. After each increment of time Δt, the energy of each zone is updated by considering the heat produced within the zone and the heat

flux into and out of the zone from neighboring regions

$$\frac{E_i(t+\Delta t) - E_i(t)}{\Delta t} = Q_i(t) + 4\pi r_{i-1}^2 F_{i-1} - 4\pi_i^2 F_i, \tag{4.1}$$

where F_{i-1} is the heat flux into zone i from zone $i-1$, F_i is the heat flux out of zone i into zone $i+1$, and $Q_i(t)$ is the radiogenic heating produced within zone i during the time interval Δt.

An "equation of state" is used to convert the energy $E_i(t)$ into an appropriate temperature T_i for each zone. By symmetry $F = 0$ at $r = 0$. The temperature at the surface is fixed at $T_N = T_{\rm surf}$ under the assumption that absorption of sunlight and emission of radiation far overwhelms the thermal flux. The system is allowed to evolve so long as the Courant stability condition is met, $\Delta t < \min\left[(\Delta r)^2/(2\kappa)\right]$, where $\kappa = k/(\rho c_{\rm p})$ is the thermal diffusivity. In practice, maintaining a time step of $\Delta t = 1000$ is usually sufficient to meet the Courant stability condition in a reasonable (CPU) time. The thermal evolution is then completely determined once the rate of radiogenic heating and the heat fluxes are determined, and once an equation of state for the matter, $T(E)$, can be established. For each zone these quantities depend on the amount of rock , ice and liquid present, which are in turn affected by differentiation.

4.3 Radiogenic Heating

The model considers the radiogenic heating due to four radionuclides: ^{40}K, ^{232}Th, ^{238}U, and ^{235}U. The heat energy released per decay of isotope x is modeled to be $(\Delta E)_X(\ln 2/t_{1/2})/m_X$, where $t_{1/2}$ is the half-life and m_X is the mass of an atom of isotope x. The heat energy is considered to be due to both α and β particles as well as γ rays, but the neutrino flux is explicitly excluded as neutrinos generally pass through matter without depositing any energy. The total mass of each isotope will decrease exponentially with time in accordance with their half lives. Initially, the rate

of radiogenic heating is found to be 44.6 pW/kg of rock, dominated by the decay of ^{40}K; whereas the rate at present day is calculated to be 5.6 pW/kg.

4.4 Fluxes

The heat flux is modeled to be carried by conduction, so that $F = -k\,\partial T/\partial r$, and is represented by the finite difference formula

$$F_i = -\frac{k_i + k_{i+1}}{2}\frac{T_{i+1} - T_i}{(r_{i+1} - r_{i-1})/2}. \tag{4.2}$$

In reality, heat flux can also be carried via convection under the right conditions, particularly within the layer of pure water ice typically predicted to be created by the model in KBOs between the rocky core and $r = R_{\rm diff}$. Convection is modeled to occur if the Rayleigh number between the top and bottom of the layer exceed a critical value $\mathrm{Ra_c} \approx 1100$ (Spohn and Schubert, 2003). The Rayleigh number is given by

$$\mathrm{Ra} = \frac{\alpha\rho_{\rm ice} g(\Delta T)(\Delta r)^3}{\kappa\,\eta}, \tag{4.3}$$

where $\Delta r = R_{\rm diff} - R_{\rm base}$, and $\Delta T = T(R_{\rm base}) - T(R_{\rm diff})$. The other quantities of thermal expansivity α, gravitational acceleration g, thermal diffusivity κ, and viscosity η are calculated at the midpoint of the layer. The thermal diffusivity is defined to be $\kappa = k/(\rho_{\rm ice} c_{\rm P})$ where k is the thermal conductivity and $c_{\rm P}$ is the heat capacity.

According to a number of models of icy satellites, the potentially convecting layer of ice is capped at the top and bottom by a by a stagnant lid of ice that transports heat through conductive flux alone (Solomatov, 1995; McKinnon 1998, 1999; Multhaup and Spohn, 2007). However, for the purposes of the model, we are only interested in the total drop in temperature across the layer, and not details about the internal thermal structure of the layer. In the case where stagnant lid convection is initiated, we assume there is a nearly isothermal layer at ($T = T_c$), capped at

the top and bottom by thermally conducting ice layers (e.g. Ellsworth and Shubert, 1983; Multhaup and Spohn, 2007). The thickness of the boundary layers is given by $\delta = (\Delta r)/\mathrm{Nu}$, where Nu is the Nusselt number of the convecting layer. The temperature difference across the potentially convecting layer is given by the temperature drop between the stagnant lids $\Delta T = F\delta/k_{\mathrm{eff}} = F(\Delta r)/(k \times \mathrm{Nu})$, where k is the thermal conductivity. The code implements this relationship by increasing the thermal conductivity of the convecting layer k by the Nusselt number so that,

$$k_{\mathrm{eff}} = k \times \mathrm{Nu}. \tag{4.4}$$

The Nusselt number is parametrized as $\mathrm{Nu} = (\mathrm{Ra}/\mathrm{Ra_c})^{0.25}$ for $\mathrm{Ra} > \mathrm{Ra_c}$ (Spohn and Schubert 2003) where the Rayleigh number, Ra, is calculated at the midpoint of the ice layer.

4.5 Ice Viscosity

Viscosity of ice is a key factor in determining that rate of parametrized convection. In this thesis I have modified the manner in which the viscosity of pure water ice is determined from the one used in the model of Desch et al. (2009). The implementation used in Desch et al. is one in which viscosity is determined by volume diffusion alone. The strain rate is given by

$$\dot{\varepsilon} = 9.3\frac{\sigma b^3 D v}{d^2 k T} \approx \frac{42\sigma V_m}{R\,T\,d^2} D_v, \tag{4.5}$$

where $b = 4.52 \times 10^{-10}$ m is the Burgers vector, $D_v = D_{0v}\exp(-Q/RT)$ is the lattice diffusion frequency, $D_{0v} = 9 \times 10^{-4}\,\mathrm{m^2\,s^{-1}}$, $Q = 59.4\,\mathrm{kJ\,mol^{-1}}$ is the activation energy for self-diffusion, and R is the gas constant (Song et al. 2006). Defining $\eta_{\mathrm{eff}} \equiv \sigma/(3\dot{\varepsilon})$ yields

$$\eta \approx 3 \times 10^{14} \left(\frac{d}{1\,\mathrm{mm}}\right)^2 \frac{T}{T_m} \exp\left[26.2\frac{T_m - T}{T}\right]\ \mathrm{Pa\,s}, \tag{4.6}$$

with $T_m = 273\,\mathrm{K}$. For grain sizes on the order of 1 mm, this equation matches well with the following equation found in Thomas et al. (1987)

$$\eta(T) = \eta_0 \left[25 \times \left(\frac{273}{T} - 1 \right) \right], \tag{4.7}$$

(where $\eta_0 = 1.0 \times 10^{14}\,\mathrm{Pa\,s}$). Therefore, Eq. 4.7 was chosen to parametrize ice viscosity for the model runs of Desch et al. (2009).

For the model used in this thesis, I parametrize the convection of the pure water ice mantle based on the composite flow law of Goldsby and Kohlstedt (2001) and the definition of viscosity used in Barr and Pappalardo (2005) [see subsection 3.2.2 for more detail]. Here $\eta \equiv \sigma / 2\dot{\varepsilon}$, and the total strain rate is

$$\dot{\varepsilon} = \dot{\varepsilon}_{\mathrm{diff}} + \left(\frac{1}{\dot{\varepsilon}_{\mathrm{basal}}} + \frac{1}{\dot{\varepsilon}_{\mathrm{gbs}}} \right)^{-1} + \dot{\varepsilon}_{\mathrm{disl}}\,,$$

where $\dot{\varepsilon}$ for each deformation mechanism is given by

$$\dot{\varepsilon} = A \frac{\sigma^n}{d^p} \exp\left(-\frac{Q + PV}{RT} \right).$$

I parametrized the relationship of viscosity to temperature assuming a stress $\sigma = 1\,\mathrm{MPa}$, and a grain size $d = 1\,\mathrm{mm}$. I then fit a 9th-order polynomial to this relationship between viscosity to temperature, and used this to parametrize ice convection in the models.

In Fig. 4.1 the functional relationship of viscosity to temperature used in Desch et al. (2009) is compared with the one used in the current model. The 9th order polynomial fit used to parametrize convection in the current model is plotted as a dashed black line, and can be seen to fit well with the curve based on the Goldsby and Kohlstedt composite flow law. I found the fit to be good to within 1% in the temperature range being considered. For reference η_{crit} is also plotted to demonstrate the variance in temperature required to produce a given viscosity based on the two models.

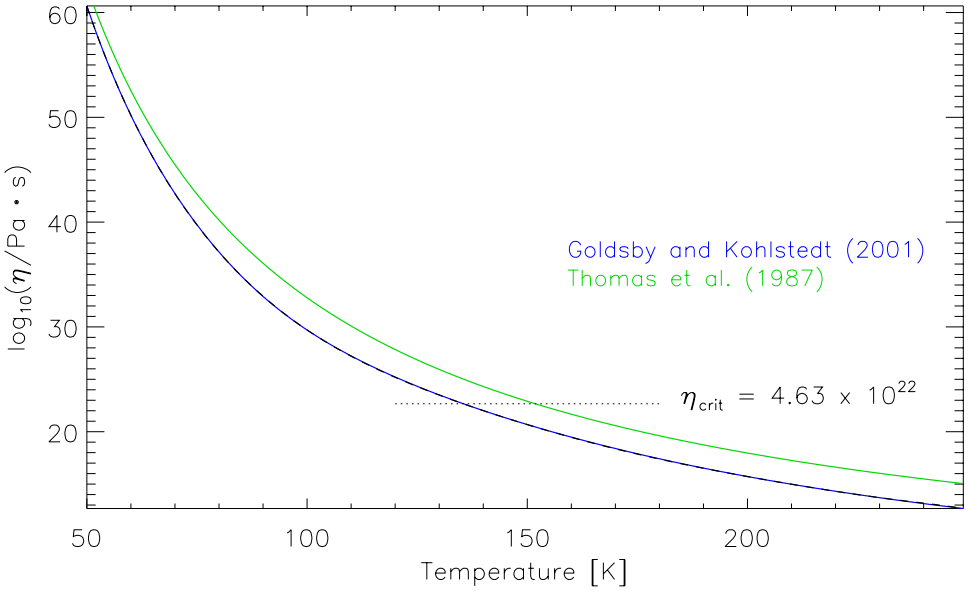

Figure 4.1: The relationship between viscosity and temperature for pure water ice based on two different models. The green curve is based on the viscosity characterization of Thomas et al. (1987), and the blue curve is based on the composite flow law of Goldsby and Kohlstedt (2001). For a given temperature, the composite flow law always produces a lower viscosity. For reference, the 9th-order polynomial fit that I used to parametrize convection in the models is over-plotted with a dashed black line.

In principle, different viscosities could change the thermal evolution of the KBO models. However in practice, the only implementation of viscosity in the code is to determe the likelihood of convection within the ice layer through its effect on the Rayleigh number. Ice convection only happens relatively early on in the evolution of the model, and basically just acts to change the effective thermal conductivity of the ice layer. This limited application of viscosity in the code for the ice layer, was not found to have much impact on the thermal evolution of the model in Desch et al. (2009).

One final note, the addition of ADH/ammonia to pure water ice drops the viscosity of the mixture by five orders of magnitude at the eutectic point of 176 K. This lowers the overall viscosity of the mixture to $< 10^{12}$ Pa s when the mass fraction of ammonia to ammonia plus water $> 1\%$ (Arakawa and Maeno, 1994). It is this lowering of viscosity in the undifferentiated layers that allow Stokes flow to occur within geologically relevant timescales. However, this should not have any effect on the viscosity of the ice mantle, since ADH and ammonia have already been removed from solution when the ice layer formed.

4.6 Thermal Conductivities and Other Relevant Physical Properties

The determination of thermal conductivities is critical to understanding the thermal gradients essential to modeling the differentiation of icy bodies. Chief among these is the thermal conductivity of rock. In this research, we assume that the composition of rock in KBOs is similar to that of ordinary chondrites. Therefore, we adopt the thermal conductivity of chondrites as measured by Yomogida and Matsui (1983) to model that of rock. These measurements show little variation between temperatures of 100 to 500 K, and typically have a conductivity of $k_{\mathrm{rock}} = 1.0\,\mathrm{W\,m^{-1}\,K^{-1}}$, which is the value adopted in Desch et al. (2009).

An alternative hypothesis is that the rocky material that accreted to form the KBO may have become hydrated through interactions with water prior to its inclusion in the KBO. Under this assumption, the rock in KBOs would likely have a density and thermal conductivity closer to that of a CM chondrite than an ordinary chondrite. Based on the experimental measurements of Opeil et al. (2010) for the thermal conductivity of CM chondrites at very low temperatures, the thermal conductivity for the rock in KBOs is expected to be $\sim 0.5\,\mathrm{W\,m^{-1}\,K^{-1}}$. Also, the density of CM chondritic material is closer to $\sim 2.35\,\mathrm{g\,cm^{-3}}$ as opposed to the value of $3.25\,\mathrm{g\,cm^{-3}}$

adopted in Desch et al. (2009).

In the models that follow, I adopt the values of $k_{\rm rock} = 0.5\,{\rm W\,m^{-1}\,K^{-1}}$ and $\rho_{\rm rock} = 2.35\,{\rm g\,cm^{-3}}$ for my new canonical model of Charon. Here I assume that the rocky material that accreted to form Charon was initially hydrated. I also explore the effect that varying the parameters of $k_{\rm rock}$ and $\rho_{\rm rock}$ have on the KBO differentiation process, both individually on collectively.

The thermal conductivity of water ice adopted for this research is $k_{\rm H_2O(s)} = 5.67\,(T/100\,{\rm K})^{-1}\,{\rm W\,m^{-1}\,K^{-1}}$ (Klinger, 1980); and that adopted for ammonia dihydrate is $k_{\rm ADH} = 1.2\,{\rm W\,m^{-1}\,K^{-1}}$ based on the experiments of Lorenz and Shandera (2001) and Kargel (1992). The thermal conductivity of a water ice-ADH mixture is taken to be the geometric mean of the two such that

$$k_{\rm ice} = k_{\rm H_2O(s)}^{\rm g_{H_2O(s)}} k_{\rm ADH}^{1-{\rm g_{H_2O(s)}}}, \tag{4.8}$$

where $\rm g_{H_2O(s)}$ is defined to be the volume fraction of H_2O(s) in the H_2O(s)-ADH mixture. The thermal conductivity of an intimate mixture of rock and ice is found by solving

$$2k_{\rm tot}^2 - \left[k_{\rm rock}(3f_{\rm rock}^V - 1) + k_{\rm ice}(2 - 3f_{\rm rock}^V)\right] k_{\rm tot} - k_{\rm rock}k_{\rm ice} = 0, \tag{4.9}$$

where $f_{\rm rock}^V$ is the volume fraction of ice in the combined ice-rock mixture. This formulation is motivated by the percolation theory of Sirono and Yamamoto (1997). Based on a comparison with alternate methods of modeling the appropriate conductivities, Desch et al. (2009) find that "Significant differences in temperature gradient can arise depending on how the thermal conductivity is modeled. In particular, the inclusion of rock in an undifferentiated crust is insulating."

At temperatures appropriate to the interior of KBOs ($\sim 100\,{\rm K}$) the density of pure water ice is about 935 kg m^{-3} (Croft et al. 1988), which is the value adopted

here. The value adopted for the density of ammonia dihydrate(ADH) is 965 kg m^{-3} (Croft et al. 1988). Assuming a porosity of $\approx 10\%$, Yomogida and Matsui (1983) find an average bulk density for chondritic rock of $\rho_{\rm rock} = 3250\,{\rm kg\,m^{-3}}$, and an intrinsic density on the order of $3600\,{\rm kg\,m^{-3}}$, which are the values adopted here.

The heat capacity for water is determined via the approximation

$$c_{\rm H_2O(s)}(T) = 773.0\left(\frac{T}{100\,{\rm K}}\right){\rm J\,kg^{-1}\,K^{-1}}, \tag{4.10}$$

which matches the exact expression of Shulman (2004) over the range $40 < T < 273$ to within a maximum deviation of 15%. The heat capacity for ADH is approximated by

$$c_{\rm ADH(s)}(T) = 1120\left(\frac{T}{100\,{\rm K}}\right){\rm J\,kg^{-1}\,K^{-1}}, \tag{4.11}$$

which matches the exact expression of Fortes et al. (2003) over the range $40 < T < 176$ to within a maximum deviation of 4%. The heat capacity of rock can be inferred from the data of Yomogida and Matsui (1983) for ordinary chondrites and is approximated by

$$c_{\rm rock}(T) = \begin{cases} 770\,\left(\frac{T}{275\,{\rm K}}\right)\,{\rm J\,kg^{-1}\,K^{-1}}, & 0\,{\rm K} \leq T < 275\,{\rm K} \\ 607 + 163\,\left(\frac{T}{275\,{\rm K}}\right)\,{\rm J\,kg^{-1}\,K^{-1}}, & 275\,{\rm K} \leq T < 1000\,{\rm K} \\ 1200\,{\rm J\,kg^{-1}\,K^{-1}}, & 1000\,{\rm K} \leq T. \end{cases} \tag{4.12}$$

The expansivity of ice, α, comes into play when determining the Rayleigh Criterion, and is important in determining whether ice will convect. At temperatures less than 60 K, ice contracts when heated and therefore cannot undergo solid-state convection, regardless of its viscosity. Desch et al. (2009) model the expansivity of ice as $\alpha\,/(10^{-5}\,{\rm K^{-1}}) = 1.5(T\,/50\,{\rm K}) - 2.0$ for $T > 50$ K, and $= -0.5(T\,/50\,{\rm K})$ for $T < 50\,{\rm K}$.

4.7 Equation of State

The code tracks the mass of 5 phases within each of the radial zones of the KBO. These include: rock; water ice, H_2O(s); solid ammonia dihydrate, ADH(s); liquid water, H_2O(l); and liquid ammonia, NH_3(l). The initial mass of all these constituents, as well as the total combined internal energy of all the phases, E_i, is tallied at the beginning of each timestep within each radial zone. Additionally, the mass of rock, the total mass of H_2O (including water ice, liquid water and bound in ADH), and the total mass of NH_3 (in liquid ammonia and bound in ADH) are specified at the beginning of each timestep in each zone. Also tracked is the non-rock mass that is in ammonia, X_i, [either as NH_3(l) or the ammonia portion of ADH(s)], the fraction of the total mass contained within the rock ($f_{\mathrm{rock}\,i}$), and the total mass within each zone M_i.

Once the values for M_i, X_i, $f_{\mathrm{rock},\,i}$ are known for a given timestep, it is assumed that the temperature can be determined by finding how much energy is required to raise the mix of chemicals from 0 K to T, including the temperature-dependent heat capacities and the latent heats of fusion. A phase diagram is used to determine the mass fraction that is in each of the phases of non-rock constituents [H_2O(s), ADH(s), H_2O(l), and NH_3(l)] at a given temperature. It is also used to determine the total specific energy $e(T)$ required to raise a water-ammonia mixture (characterized by X_i), from 0 K to a temperature T. The formulas used to approximate the phase diagram are complicated and can be found in Appendix B of Desch et al. (2009), but won't be reproduced here. They provide a way to numerically calculate the phase diagram for all of the non-rock constituents in each zone.

With this calculated, the total energy required to raise the temperature of all

constituents from 0 K to a temperature T is given by

$$E(T) = f_{\mathrm{rock,i}} M_i \int_{0\,\mathrm{K}}^{T} c_{\mathrm{rock}}(T')\, dT' + (1 - f_{\mathrm{rock,i}}) M_i e(T), \tag{4.13}$$

where M_i is the total mass contained within each zone. However, what we actually have are the values for f_{rock}, X and E for each shell, and from these we must determine the temperature, T_i, at which $E(T) = E_i$. This is accomplished by using a bracketing techniques (Press et al. 1992). Using the bracketing technique, a temperature $T(E)$, and an apportionment of non-rock material into ices and liquids can be found that is consistent with that internal energy and temperature. For this model, volume changes are explicitly neglected in the calculations.

4.8 Differentiation

The code of Desch et al. (2009) models the evolution of a homogeneous body consisting of a mixture of rock and ice as it responds to the effects of radiogenic heating. As the body heats up, ices are allowed to melt as described in section 4.7, causing rock to differentiate from the ice and liquid. This differentiation of the rock, liquid and ice mixture is treated as a two-step process. First, we consider the separation of rock from the other components, with the resulting formation of a rocky core. This may involve melting of the ice, but not necessarily. Second, we consider the separation of liquid water, ammonia and ammonia dihydrate from the water ice. Once the appropriate conditions are met for a given shell of material, the differentiation is effectively instantaneous, generally occurring within a single timestep of 1000 years.

The separation of rock and ice without melting the ice is assumed to occur by a process of solid-state creep of ice around the denser rock. This process is described by Stokes flow, with velocity

$$V = \frac{1}{18} \frac{(\rho_{\mathrm{rock}} - \rho_{\mathrm{ice}}) g D_{\mathrm{rock}}^2}{\eta}. \tag{4.14}$$

Here $D_{\rm rock}$ is the diameter of the rocky particules, $\rho_{\rm rock}$ is its density, and g is the gravitational acceleration appropriate for the shell ($\sim 0.30\,{\rm m\,s^{-2}}$ for a typical KBO). For differentiation to occur, we require that the rock must drop one grid zone ($\sim 2\,{\rm km}$) on timescales $< 10^6\,{\rm yr}$. For viscosities typical of water ice at temperatures less than 176 K, the timescale required for a 1 m - diameter rock to drop is then on the order of a Gyr. In that case, we would assume that differentiation will not occur until the ice melts. However, if the ice consists of a mixture of water and ADH with $X \geq 1\%$, an entirely different result is possible. Once the ADH beings to melt, it will produce liquid H_2O and NH_3, and the viscosity of the mixture will drop to $< 10^{12}\,{\rm Pa\,s}$ (Arakawa and Maeno, 1994). This drop in viscosity is sufficient to differentiate the rock/ice mixture on timescales consistent with the model. Still, we are left with a number of uncertainties in the model. We do not know, a priori, the size of individual rock components, and for rocks considerably less than 1 m in size, the rate of Stokes flow is insufficient to allow differentiation to occur on geological timescales even with ammonia. Additionally, values of $X < 1\%$ are not known with certainty to produce a sufficient drop in viscosity of the ice/rock mixture, and again Stokes flow alone will not be sufficient to allow for differentiation.

Once material has reached temperatures sufficient to allow for the differentiation of rock from the other components, the liquids and ices can separate fairly rapidly via convection. Convection is expected to occur when the Rayleigh number (see Eq. 4.3) exceeds a critical value, $R_{\rm c} \sim 10^3$. Assuming typical parameters of $\alpha \sim 3 \times 10^{-5}\,{\rm K^{-1}}$, $\rho_{\rm ice} \sim 1000\,{\rm kg\,m^{-3}}$, $g \sim 0.10\,{\rm m\,s^{-2}}$, $\kappa \sim 10^{-6}\,{\rm m^2\,s^{-1}}$, $\Delta T \sim 100\,{\rm K}$, and $\Delta r \sim 100\,{\rm km}$, we find ${\rm Ra} \sim 3 \times 10^{20}\,{\rm Pa\,s}/\eta$. Once the melt of the ADH has begun, we expect viscosities $< 10^{12}\,{\rm Pa\,s}$. This viscosity is more than sufficient to allow rapid convection to occur. It is expected that within 40 Myr, the remaining phases should separate according to density, with pure water ice rising to the top and ammonia concentrated

in the liquid layer at the bottom. The ADH and liquids are expected to be chemically and energetically well-mixed within the "slush" layer at the base (Desch et al. 2009).

Once a shell at some radius r reaches a temperature of 176 K, the code assumes that the entire shell differentiates instantaneously. The radius, $R_{\rm diff}$, is defined to be the maximum radius within a KBO at which the temperature has ever exceeded 176 K. It is expected that all the rock within this radius will settle to form a rocky core. The remaining phases will settle depending on their densities, with liquid water and ammonia directly above the rock, and pure water ice above the liquid. At radii greater than $R_{\rm diff}$, it is assumed that the material remains undifferentiated.

The implementation of differentiation in the code proceeds as follows. At each timestep, the equation of state is used to determine the effective temperatures of each shell. From this, $R_{\rm diff}$ is determined. Then, working from the innermost zone outward, all of the mass and internal energy of the rock interior to $R_{\rm diff}$ is moved to the core. After all of the rock has been moved, the slush layer of ammonia and liquid water is moved above the core, bringing with it the appropriate mass and internal energy taken from each zone. Finally, the movement of the remaining water ice completes the process as it is moved above the slush layer until it fills all the shells out to $R_{\rm diff}$. This is used to create and fill a new grid up to exactly $R_{\rm diff}$. All of the material is moved in a volume conservative way that is independent of the chemical phases. Outside of $R_{\rm diff}$, the undifferentiated material remains unchanged.

The final piece to consider at this point is the determination of the gravitational energy released by the movement of all of the phases of material. This is done by calculating the gravitational potential energy U_g immediately before and after each timestep with

$$U_{\rm g} = -G \int_0^{R_{\rm p}} 4\pi\xi^2 \rho(\xi) \frac{M(\xi)}{\xi}\, d\xi, \tag{4.15}$$

where $M(\xi)$ is the mass enclosed within a sphere of radius ξ. Any gravitational

energy released during the timestep is uniformly distributed as heat throughout all shells interior to $R_{\rm diff}$. We find that this release of gravitational energy only results in an increase in temperature of a few degrees K in the core during the differentiation process (Desch et al. 2009).

4.9 Thermal Evolution of Charon

Having considered the methodology and implementation of the thermal evolution code, we can now apply it to our canonical case of Pluto's largest moon, Charon. Based on some of the most recent observations, Charon's radius $R_{\rm C} = 603.6 \pm 1.5$ km (Person et al. 2006). Estimates of Charon's mean density vary from $\bar{\rho} = 1720 \pm 150\,{\rm kg\,m^{-3}}$ (Gulbis et al. 2006) assuming a mass of $1.60 \pm 0.12 \times 10^{21}$ kg (Olkin et al. 2003), to $\bar{\rho} = 1630 \pm 70\,{\rm kg\,m^{-3}}$ (Person et al. 2006) assuming a mass $1.52 \pm 0.064 \times 10^{21}$ kg (Buie et al. 2006). Rather than fix particular values of mass and radius, here we consider the more generic case of a body with radius 600 km, and mean density $\bar{\rho} = 1700\,{\rm kg\,m^{-3}}$ (yielding a total mass 1.538×10^{21} kg). Since the process of differentiation is accelerated for objects with high ammonia content, we assume a low value of $X = 0.01$, to be conservative. With this choice of values, our Charon analog has a rock mass fraction $f_{\rm rock} = 0.63$, and a total rock mass of 0.97×10^{21} kg. As explained in section 4.3, the rate of heat production at present day is then determined to be $S \approx 5.66\,{\rm pW\,kg^{-1}}$. Based on a number of different kinds of observations (Cook et al. 2007), we adopt a surface temperature of 60 K; although this value is somewhat uncertain.

4.9.1 Numerical Results

Simulations created using the code of Desch et al. (2009) track a fascinating time evolution for our canonical Charon. We begin with the cold accretion of homogeneous

chondritic material, and are left with a partially differentiated body which may, even now, contain enough liquid water to allow for cryovolcanism. The following describes the results of the numerical modeling.

It takes roughly 75 Myr of evolution for the temperatures in the core to rise above 176 K, the melting point of ADH. At this point, the viscosity within the ice can drop by 5 orders of magnitude, and differentiation begins in earnest. As early as 80 Myr, the core contains all of the rock within a radius of $R_{\rm diff} = 420$ km, consuming half the rocky mass of the body, with a radial extent of about 292 km. This process continues at a more gradual rate for another 700 Myr. By $t \approx 0.75$ Gyr, $R_{\rm diff}$ has reached its maximum extent of 516 km, with a core radius of 356 km. The slush layer of liquid water and ammonia now extends from the top of the rocky core to the base of the pure water ice layer at 368 km. The water ice layer then continues to the outer edge of the differentiated zone, $R_{\rm diff} = 516$ km, surrounding by a crust of undifferentiated material.

The thermal evolution of our Charon analog is tracked in Fig. 4.2. As shown in the Figure, the temperature in the core is initially set to $T_{\rm surf}$, and rises gradually over the next 2 Gyr. The energy from the decay of long-lived radionuclides is initially concentrated within the rocky core, primarily serving to heat it, which only allows for a reduced flux outside the core. At about 2 Gyr, the core reaches its maximum temperature of 1418 K. From this time onward the heat flux exterior to the core is enhanced by the release of energy previously stored in the core. The "slush" layer between 356 and 396 km is partially liquid and highly convective, allowing heat to pass through efficiently. Convection also carries heat efficiently through the ice layer, where the Nusselt number is 4.4 at $t = 1$ Gyr, gradually dropping to 1.0 at $t = 4$ Gyr, after which convection turns off.

The distribution of the different constituents of the body is shown in Fig. 4.3.

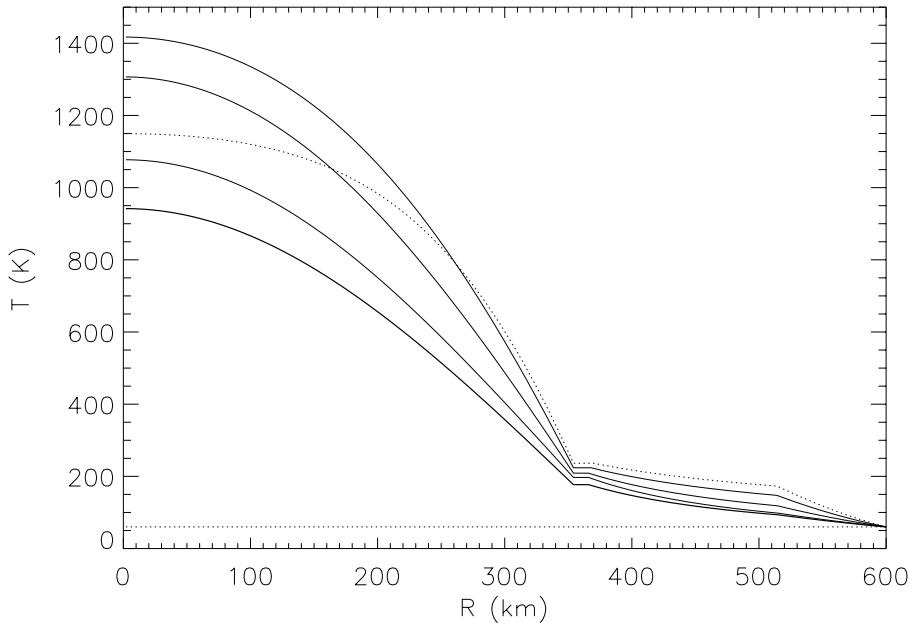

Figure 4.2: Temperatures within a Charon analog, at times $t = 0$ (dotted line), $t = 1$ Gyr (dotted curve), and (solid curves, from top to bottom) $t = 2$ Gyr, 3 Gyr, 4 Gyr and the present day, $t = 4.56$ Gyr (Reproduced with permission from Desch et al. 2009.)

At 2 Gyr the differentiation is fairly complete, with the values for $R_{\rm core}$ and $R_{\rm diff}$ only changing slightly with time; however, the relative extent of the ice and slush layers evolves over a longer period of time. $R_{\rm diff}$ and $R_{\rm core}$ do not change after 2 Gyr, but much of the liquid water in the slush layer evenually freezes to water ice. This simulation predicts that the liquid layer will extend from 356 to about 362 km at present day.

Fig. 4.4 depicts the time evolution of the liquids tracked in the Charon analog. The total mass of ice is 0.57×10^{21} kg, and that of ADH is 0.0177×10^{21} kg. After 80 Gyr all of the ADH within $R_{\rm diff} = 420$ km has melted as the temperature rises beyond 176 K. The result is the production of 0.0061×10^{21} kg of liquid. Initially, the liquid has an ammonia content near the eutectic as is displayed in Fig. 4.5. Over

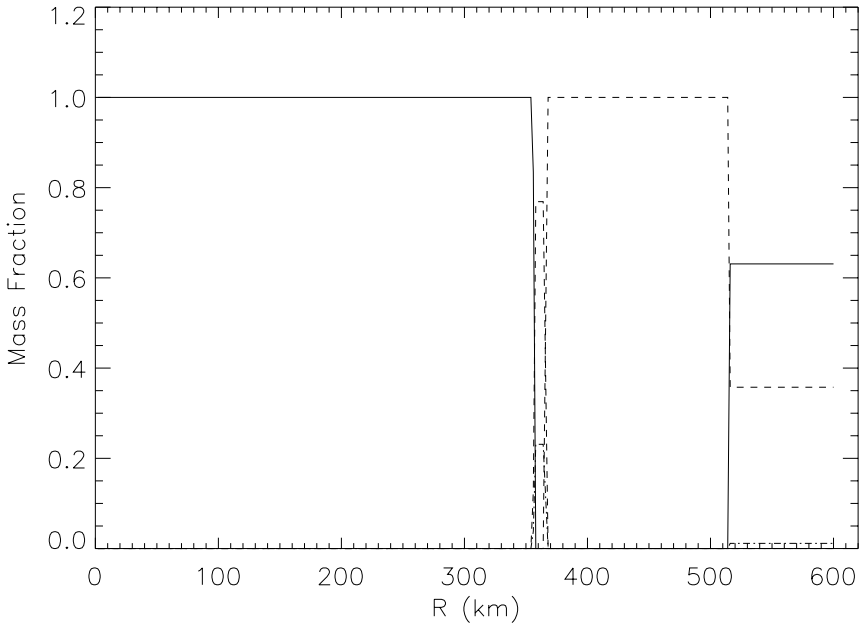

Figure 4.3: Distribution of phases within a Charon analog at time $t = 2\,\mathrm{Gyr}$. The lines represent rock (solid line), solid or liquid water (dashed lines), and ammonia dihydrate or liquid ammonia (dash-dot lines). A core of pure rock exists within 355 km. Between 355 km and 362 km there is a layer of water/ammonia liquid, and from 362 km to 515 km there is a layer of pure water ice. From 515 km to the surface at 600 km there is an undifferentiated crust of rock, water ice and ADH. (Reproduced with permission from Desch et al. 2009.)

the next few 100 Myr the water ice melts, diluting the ammonia. The liquid content peaks at about 1 Gyr, with a mass of 1.8×10^{19} kg (or about 1% of the mass of the KBO). At this point we have an ammonia fraction of $X \approx 0.2$. Thereafter the overall heat flux out of the core begins to decrease, causing the liquid to refreeze. When the last of the water ice has frozen out, the ammonia concentration reaches the eutectic. The current model shows this happening around 4.5 Gyr, or present day.

The final two plots in this chapter demonstrate how pressure is distributed throughout the Charon analog, and how the heat flux through the surface evolves through time. Pressure is plotted as a function of depth in Fig. 4.6 at time $t = 4.56$ Gyr. This is calculated through a simple integration of mass at different radii from the surface

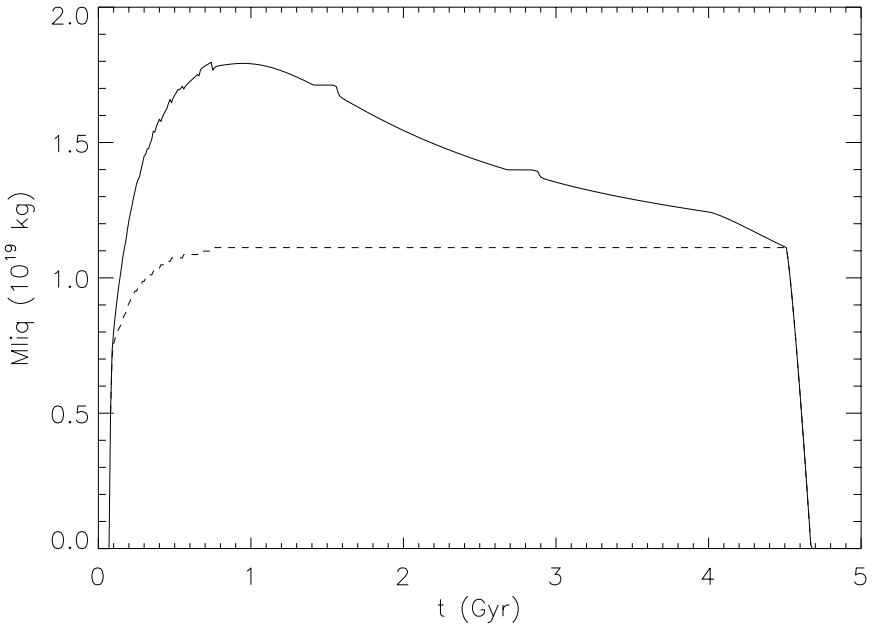

Figure 4.4: Total mass of liquids within a Charon analog (solid curve), and that mass of liquids derived from melting of ADH (dashed curve), as a function of time. The first liquid arises from ADH suddenly melted at $t \approx 75$ Myr during initial differentiation. Continued heating melts water, but it eventually refreezes. By $t = +4.5$ Gyr, the remaining liquid refreezes as ADH, until by $t = 4.61$ Gyr it is completely frozen. (Reproduced with permission from Desch et al. 2009.)

inward

$$\frac{dP}{dr} = -\frac{GM(r)\rho(r)}{r^2}. \tag{4.16}$$

Here it can be seen that the pressure at the center is elevated from 135 MPa, which is the value it would have without differentiation, to its current value of 269 MPa. The pressure in the liquid layers is around 78 MPa, and the pressure in the ice layer varies from 78 MPa to about 38 MPa. The undifferentiated crust has lower pressures still, on the order of 20 MPa. Noting that the transition from Ice I to Ice II doesn't occur until pressures of at least 100 MPa (Durham and Stern 2001), it is clear that the ice within this body will all have the structure and density of Ice I. For larger icy bodies (such as those found in the Jovian system or even Pluto where $R_{\rm P} \geq 1000$km),

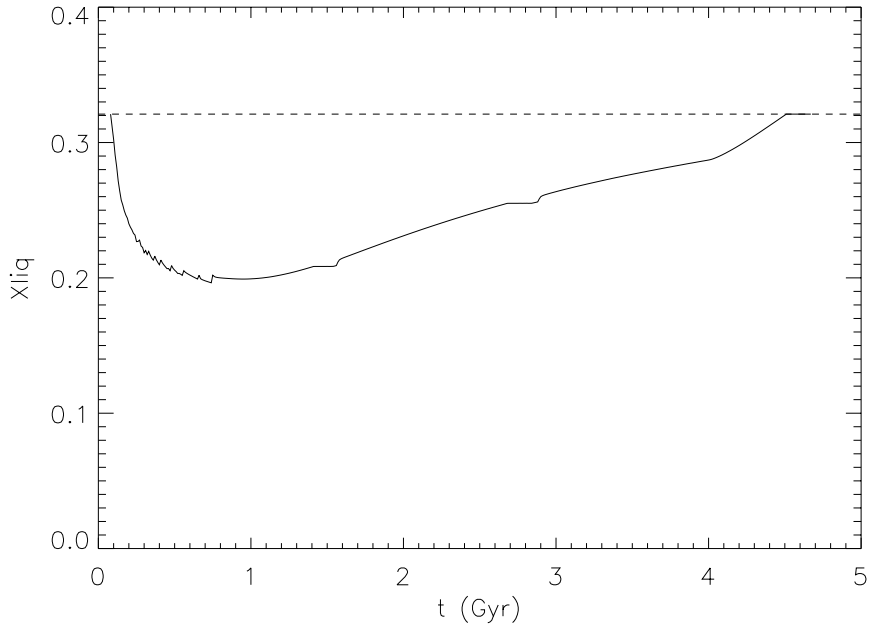

Figure 4.5: Mass fraction X of ammonia in the liquid inside a Charon analog, as a function of time. The eutectic concentration, 0.321, is plotted for comparison. (Reproduced with permission from Desch et al. 2009.)

higher pressures in the ice layer are possible, and are beyond the scope of this work. Additionally, the ammonia-phase diagram used in the paper is not valid beyond 200 MPa; therefore other considerations need to be taken into account for icy bodies with pressures that high.

Finally, Fig. 4.7 plots the surface flux for our KBO simulation as a function of time. As shown in the plot, the amount of heat flux through the surface is less than the total heat produced in the core. This is because much of the radiogenic heat initially produced within the core is retained there as it heats up. After the core reaches a maximum temperature at 2 Gyr, the core begins to release its stored heat, and the heat flux through the surface is increased relative to the total amount of radiogenic heat produced in the core. This process continues to present day, with the result that the current heat flux through the surface is enhanced by a factor of 1.42, or

$\epsilon = 0.42$, over the instant radiogenic heat flux. This shows the critical importance of considering the prior thermal evolution of a KBO when trying to ascertain its current thermal structure. Without considering this effect, the current temperature at $R_{\rm diff}$ would only be 81 K, and the temperature at the base of the ice layer would only be 120 K. Thus, there would be no liquid present in our simulated present-day Charon.

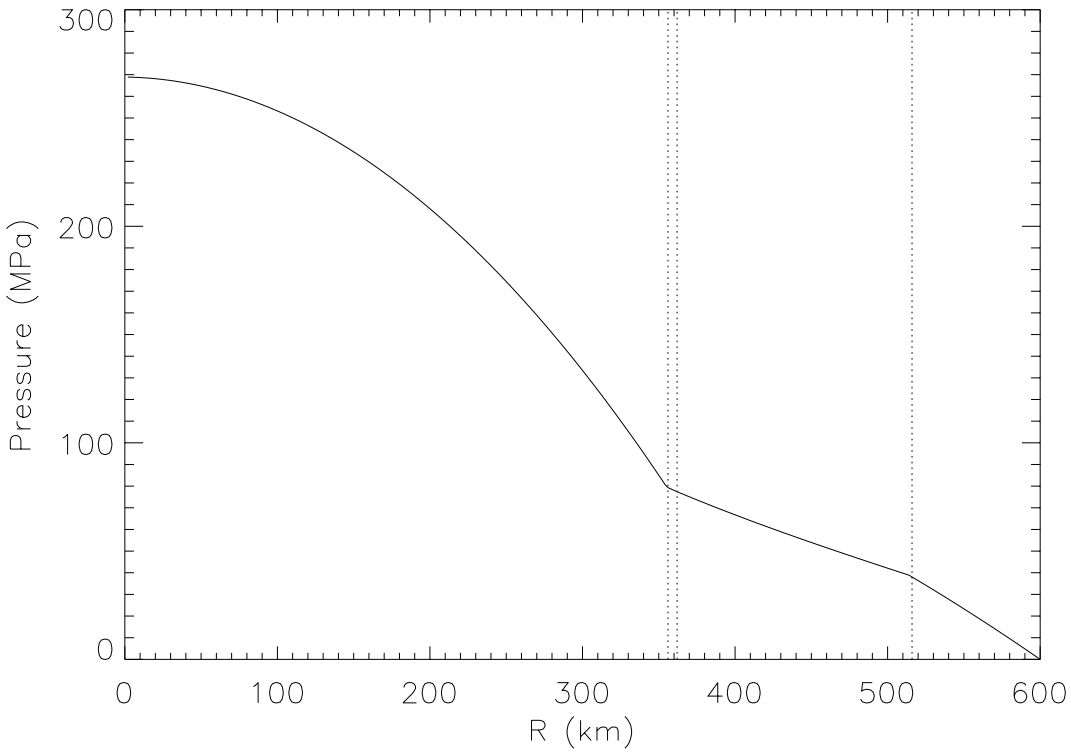

Figure 4.6: Pressures inside a Charon analog, as a function of radius within the body, at a time $t = +2\,\mathrm{Gyr}$, when differentiation is complete. The vertical dotted lines represent (from left to right) the boundaries between the rocky core, the liquid layer, the water ice layer, and the undifferentiated ice/rock crust. Reproduced with permission from Desch et al. 2009.)

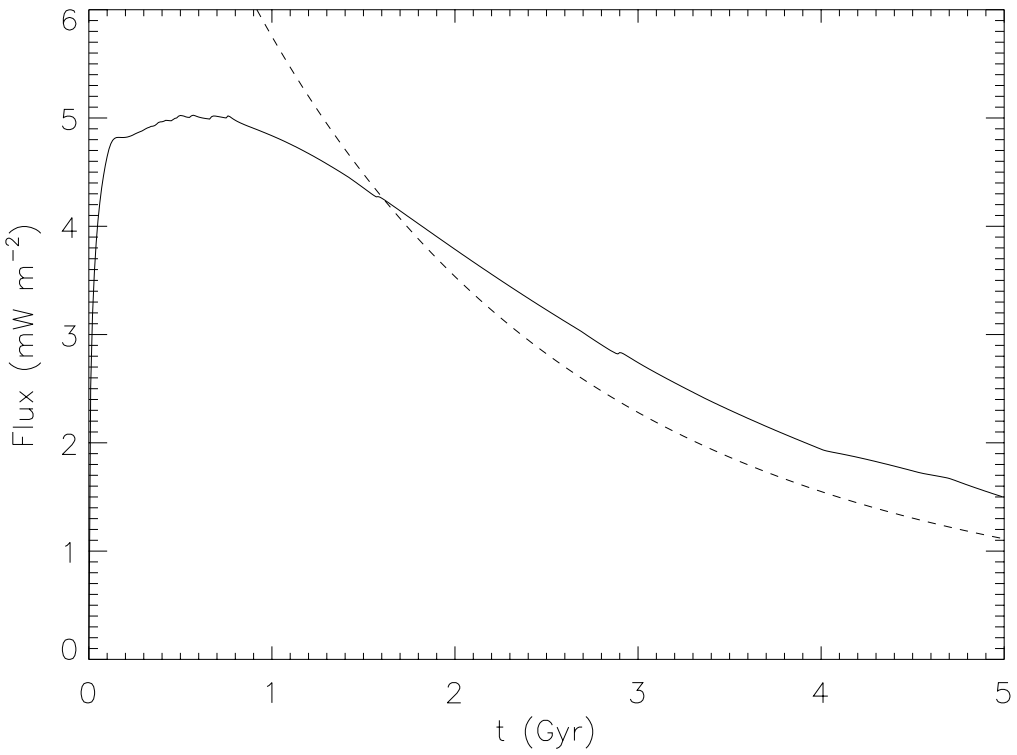

Figure 4.7: Heat flux at the surface of a Charon analog, as a function of time (solid curve). For comparison we plot the flux that would arise from the instantaneous rate of radioactive decay (dashed line). During the first 1.6 Gyr, the rocky core absorbs more heat than it emits, but thereafter the core releases heat and enhances the heat flux. Reproduced with permission from Desch et al. 2009.)

Chapter 5

RESULTS AND DISCUSSION

5.1 Overview

The numerical models of Desch et al. (2009) assume a body that accretes cold, heats up through radiogenic heating, and then partially differentiates via Stokes flow, leaving an undifferentiated crust. In the models that follow, I assume that the body has already partially differentiated due to the action of Stokes flow, or an actual melting of the ice at 273 K. Differentiation can then be expected to proceed via Rayleigh-Taylor instabilities. The question addressed in this thesis is whether the additional consideration of Rayleigh-Taylor instabilities in the boundary layer between the ice mantle and the overlying crust will allow further differentiation, perhaps even full differentiation. As described in Chapters 2 and 3, the extent of Rayleigh-Taylor instabilities is dependent on both the temperature of the boundary layer and how long that layer sees an elevated temperature. The purpose of this chapter is to present numerical models to calculate the temperatures and duration of heating of these layers within a small icy body.

5.2 Change in Model Parameters

The results following are based on the numerical code found within Desch et al. (2009). However, I have added a few refinements to the code to better reflect the material parameters and physics of our Charon analog. The first change regards the parametrization of ice convection within the code. As described in section 4.4, the modeling of convection within the ice layer depends on its Rayleigh number.

The Rayleigh number in turn depends on the ice viscosity, which must be modeled properly. The original model of Desch et al. (2009) determines the value for ice viscosity based solely on the mechanism of volume diffusion found in Thomas et al. (1987). A more accurate model for the viscosity of ice requires the inclusion of all of the four deformation mechanisms described in section 3.2.2. Based on the model parameters of Goldsby and Kohlstedt (2001), I developed a ninth-order polynomial fit for the relationship of viscosity to temperature that includes all four mechanisms. This new model for ice viscosity replaces that of Thomas et al. (1987) used in the original code.

Second, I have attempted better model the composition of the original undifferentiated material which accreted to form our Charon analog. The model of Desch et al. (2009) assumes a rocky material similar in composition to olivine, with a density of $3.25\,\mathrm{g\,cm^{-3}}$, and a thermal conductivity $k = 1\,\mathrm{W\,m^{-1}\,K^{-1}}$. In our new models, we consider the possibility that the rocky material originally accreted to form Charon was closer in composition to that of a CM chondrite, and had been substantially thermal aqueously altered prior to Charon's formation. Therefore we consider rocky material with a density of $2.35\,\mathrm{g\,cm^{-3}}$ and a thermal conductivity $k = 0.5\,\mathrm{W\,m^{-1}\,K^{-1}}$ (Opeil et al. 2010). Finally, to more accurately reflect observations of the size and mass of Charon, we now adopt a mean density $\bar{\rho} = 1.65\,\mathrm{g\,cm^{-3}}$ for Charon, as opposed to that used in Desch et al. of $\bar{\rho} = 1.70\,\mathrm{g\,cm^{-3}}$.

5.3 Reproduction of Prior Results

The first task I completed before initiating any of the new model runs was to replicate the results from the previous work. I converted the code used in Desch et al. (2009) from Fortran 77 to Fortran 90, and made some other modifications to the code to allow for modeling of additional parameters, if desired. To determine whether

any of the changes in the code might impact the final results, I re-ran the simulation of Desch et al., using the same parameters as were originally included in that model. In particular, I used a value of $\bar{\rho} = 1.70\,\mathrm{g\,cm^{-3}}$ for the mean density of Charon along with $\rho_{\mathrm{rock}} = 3.25\,\mathrm{g\,cm^{-3}}$, and $k_{\mathrm{rock}} = 1\,\mathrm{W\,m^{-1}\,K^{-1}}$. What I found was that my results varied by less than a percent from those of the prior model outlined in section 4.9.1. The new core radius remains unchanged at 356 km, and R_{diff} nominally changed from 515 km in the old model, to 514 km. The maximum temperature reached in the core of 1414 K was achieved at 2.03 Gyr in my new model run, as opposed to 1418 K at 2.07 Gyr in the previous model. The thermal history remains virtually unchanged, as does the mass of the core, the total mass of the crust, and the peak amount of liquid found in the body. Additionally, the time at which the final remaining liquid freezes remains unchanged. The new Fortran 90 code therefore matched the previous Fortran 77 code.

5.4 Effect of Change in Mean Density of Charon analog

Changing the density of the Charon analog from $\bar{\rho} = 1.70$ to $1.65\,\mathrm{g\,cm^{-3}}$ has a significant effect on the results of the model. Having fixed the density of the rocky material and the ice, a decreased overall mean density requires a greater ratio of ice to rock. Additionally, the model assumes that all of the radioactive material is bound to the rocky material within the body; therefore, an increased ratio of ice to rock implies that there is a corresponding decrease in the amount of radiogenic material available to heat the body. This results in a proportional decrease in the rate of heating in the body.

The two effects combined result in a decrease in the final radius of the core from 356 to 342 km, and the differentiation radius R_{diff} decreases from 514 to 504 km. The maximum temperature of the core decreases slightly from 1414 K to 1364 K, and the

time at which the last liquid freezes decreases from 4.67 to 4.55 Gyr. This implies that the last of the liquid may have just finished freezing at the current epoch. The decrease in R_{diff} results in an increase in the total mass of the undifferentiated crust from 38.26% to 40.73% of the total mass.

5.5 Effect of Changing Model Parameters in our Base Model

Before attempting to model the effect of lowering the differentiation temperature from one reflecting Stokes flow to one considering the additional effect of Rayleigh-Taylor instabilities, I needed to ascertain how changing each of the physical parameters listed above affected the simulations. My starting point was the previous simulation with $\bar{\rho} = 1.65\,\text{g}\,\text{cm}^{-3}$, and $T_{\text{diff}} = 176$ K. To determine the effects, I ran a unique simulation for each of the following parameters: the parametrization of ice convection, the density of the rocky component in the mixture, and the thermal conductivity of the rocky component.

5.5.1 Parametrization of Convection

Changing the parametrization of convection from one in which viscosity is solely modeled through volume diffusion, to one which includes all four deformation mechanisms, has a limited effect on the results of the model. The final radius of the core remains unchanged at 342 km, and the radius of differentiation for the body marginally increases from 504 to 506 km. The maximum temperature in the core decreases slightly from 1364 to 1357 K, and occurs at 1.91 Gyr as opposed to 1.93 Gyr in the previous model.

One noticeable change was the the time at which the last liquid freezes, which occurs at 4.26 Gyr in the current simulation, as opposed to 4.55 Gyr in the base model. This result is not particularly surprising, for the following reason. The net

effect of changing the flow law used to determine ice viscosity from volume diffusion to one including all four mechanisms, is to lower the overall viscosity of the ice. This is because volume diffusion is the slowest of the four deformation mechanisms considered here. Therefore, adding in the other three ice flow mechanisms results in a higher strain rate for a given stress and a lower viscosity. A lower viscosity, in turn, results in a higher rate of convection in the ice layer. Therefore, heat can be released from the ice mantle more efficiently allowing the underlying liquid layer to cool more rapidly. In general, the model is fairly insensitive to changes in viscosity because the convecting ice layer is already almost isothermal.

5.5.2 Density of Rocky Component

Next, I evaluated the effect of changing the density of the rocky component of our Charon analog from $\rho_{\text{rock}} = 3.25$ to $2.35\,\text{g}\,\text{cm}^{-3}$. This change is to better reflect the density of the hydrated rocky material found in CM chondrites, which may have originally accreted to form Charon. The immediate effect of this change is to require an increase in the proportion of rocky material to ice in our model to maintain a fixed mean density for the KBO. Additionally, since the chemical composition of the rocky component has changed, we needed to reflect this in our modeling of the radioactive decay rate. What we found was that the overall instantaneous rate of radiogenic heating needed to decrease to be consistent with the composition of the hydrated rock. Therefore, although the overall amount of rocky material containing radionuclides increases in this model, the net expected increase in the rate of radiogenic heating is decreased.

The results of the simulation using a decreased $\rho_{\text{rock}} = 2.35\,\text{g}\,\text{cm}^{-3}$ are as follows. There is a marked increase in the size of the core from 342 to 420 km, which reflects the higher overall ratio of rocky material to ice. The final differentiation radius also

increases from 504 to 526 km. The increase in the size results in an increase in its mass decreases from 5.38×10^{20} to 7.23×10^{20} kg. The increased differentiation radius results in a decrease in the total mass of the undifferentiated crust from 6.08×10^{20} to 4.87×10^{20} kg, with a corresponding decrease in the percent of the mass of the crust from 40.73% to 32.82%.

The maximum temperature of the core decreases from 1364 to 1192 K and occurs at 1.99 Gyr as opposed to 1.93 Gyr in our base model. Since the gross amount of ice/liquid in the body has decreased, we find that the highest amount of liquid ever present in the body decreases from 1.76×10^{19} kg to 1.33×10^{19} kg. This may be also be due to a decrease in the overall rate of heating in the body. Also, the time at which the last liquid freezes now occurs much sooner, at 3.75 Gyr as opposed to 4.55 Gyr in the base model.

5.5.3 Thermal Conductivity of Rocky Component

The final parameter change considered in the new models is a change in the presumed thermal conductivity of the rocky material. We now consider a new thermal conductivity $k_{\text{rock}} = 0.5\,\text{W}\,\text{m}^{-1}\,\text{K}^{-1}$ as measured for CM chondrites at low temperatures (Opeil et al. 2010). The simulation results with this value for k_{rock} display relatively minor changes to the final core and differentiation radii, but a significant effect in the overall thermal history of the body. The radius of the core decreases from 342 to 338 km, resulting in a concurrent decrease in the mass of the core from 5.38×10^{20} to 5.19×10^{20} kg. The radius of maximum differentiation also decreases slightly from 504 to 498 km, resulting in a concurrent increase in the mass of the crust from 6.08×10^{20} to 6.39×10^{20} kg. Finally, the percent of the total mass of the body found in the crust increases from 40.73% to 42.82%.

The relatively low thermal conductivity of the rocky material implies that it is

more difficult for heat to escape from the developing core. Heat is therefore retained longer in the core, which is reflected in a higher maximum temperature for the core of 1770 K. This maximum temperature now occurs at 2.92 Gyr, a full billion years later than in the base model. The thermal evolution of our Charon analog with $k_{\rm rock} = 0.5\,{\rm W\,m^{-1}\,K^{-1}}$ and $\rho_{\rm rock} = 3.25\,{\rm g\,cm^{-3}}$ is displayed in Fig. 5.1. The maximum

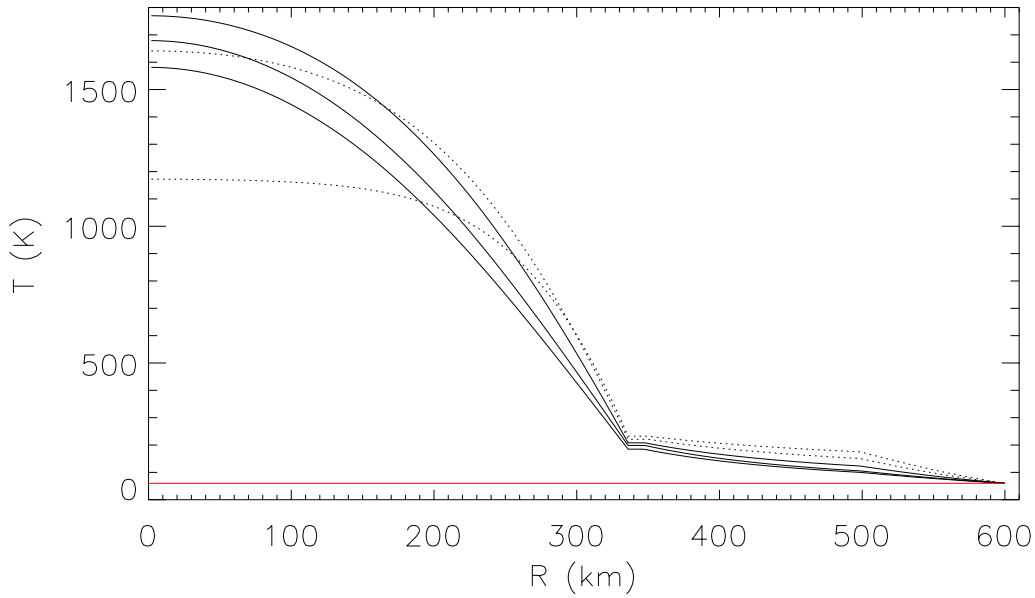

Figure 5.1: Temperatures within a Charon analog with $k_{\rm rock} = 0.5\,{\rm W\,m^{-1}\,K^{-1}}$ and $\rho_{\rm rock} = 3.25\,{\rm g\,cm^{-3}}$, at times $t = 0$ (dotted line), $t = 1\,{\rm Gyr}$ and $2\,{\rm Gyr}$ (dotted curves), and (solid curves, from top to bottom) $t = 3\,{\rm Gyr}$, $4\,{\rm Gyr}$ and the present day, $t = 4.56\,{\rm Gyr}$

instantaneous amount of liquid found in the body decreases somewhat from $1.76 \times 10^{19}\,{\rm kg}$ to $1.60 \times 10^{19}\,{\rm kg}$. However, the liquid does not fully freeze in this model until 4.99 Gyr, which reflects both the higher temperatures in the core, and the delayed

release of this energy from the core.

5.5.4 New Base Stokes Flow Model Including all Parameter Changes

The final simulation for this group of models combines all of the parameter changes listed above at a temperature $T_{\text{diff}} = 171$ K consistent with differentiation via Stokes flow. Specifically, $k_{\text{rock}} = 0.5\,\text{W}\,\text{m}^{-1}\,\text{K}^{-1}$, $\rho_{\text{rock}} = 2.35\,\text{g}\,\text{cm}^{-3}$, $\bar{\rho} = 1.65\,\text{g}\,\text{cm}^{-3}$, and the new parametrization for ice convection follows from the viscosity flow laws of Goldsby and Kohlstedt (2001). In the results of this simulation, the radius of the core increases from 342 to 422 km, with a concurrent increase in the mass of the core from 5.38×10^{20} to 7.4×10^{20} kg. The radius of maximum differentiation also increases from 504 to 530 km, resulting in a concurrent decrease in the mass of the crust from 6.08×10^{20} to 4.64×10^{20} kg. Finally, the percent of the total mass of the body found in the crust decreases from 40.73% to 31.08%. Fig. 5.2 graphically displays the structure of this model at 2 Gyr. At this point differentiation is complete; however, the liquid layer has not completely frozen yet.

Due to the lowered thermal conductivity of the rocky material, the core does not reach its peak temperature of 1541 K until 3.08 Gyr. In comparison, the maximum temperature of 1364 K is achieved at 1.93 Gyr in the prior base model. The maximum instantaneous amount of liquid found in the body decreases from 1.76×10^{19} kg to 1.07×10^{19} kg. In this simulation the liquid freezes fairly early on at 3.89 Gyr. Fig. 5.3 portrays the thermal history for the new Stokes flow base model and Fig. 5.4 shows the amount of liquid present in the model over time.

The final plot for this model (Fig. 5.5) graphically illustrates the temperature evolution for individual shells experiencing differentiation via Stokes flow. For clarity, only the outermost shells are displayed in this plot, beginning with one at a radius of 420 km. The interior shells are the hottest, and as we move outwards from the core,

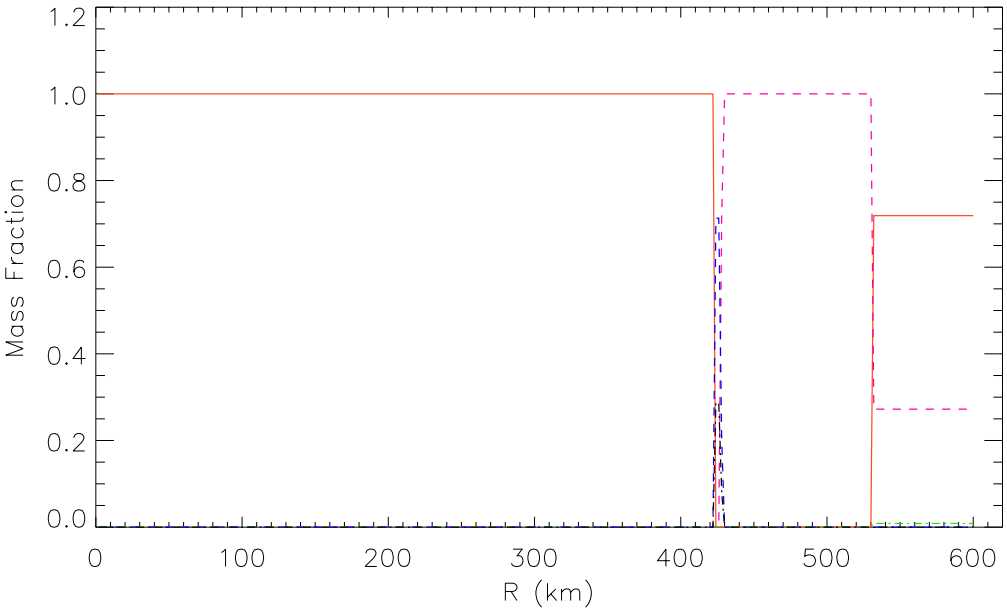

Figure 5.2: Distribution of phases for the new Stokes flow base model at $t = 2$ Gyr. The lines represent rock (orange), solid or liquid water (dashed lines), and ammonia dihydrate or liquid ammonia (dash-dot lines). A core of pure rock exists within 422 km. Between 422 and 428 km there is a layer of water/ammonia liquid, and from 428 to 530 km there is a layer of pure water ice. From 530 km to the surface at 600 km there is an undifferentiated crust of rock, water ice and ADH.

we reach a shell that just barely crosses the threshold temperature for differentiation of $T_{\rm diff} = 171$ K. Our model assumes that the differentiation process for this shell will be initiated once it is within 10 K of $T_{\rm diff}$ (green line) and will continue until the shell is fully differentiated. This shell (shown in red) has an outer radius of 530 km, which is the maximum radius for differentiation, $R_{\rm diff}$, of this model. Any shell outside of this radius will never rise above $T_{\rm diff}$, and will therefore never differentiate. Note that the time period, τ, for which the shell remains within 10 K of $T_{\rm diff}$ is ≈ 1.5 Gyr.

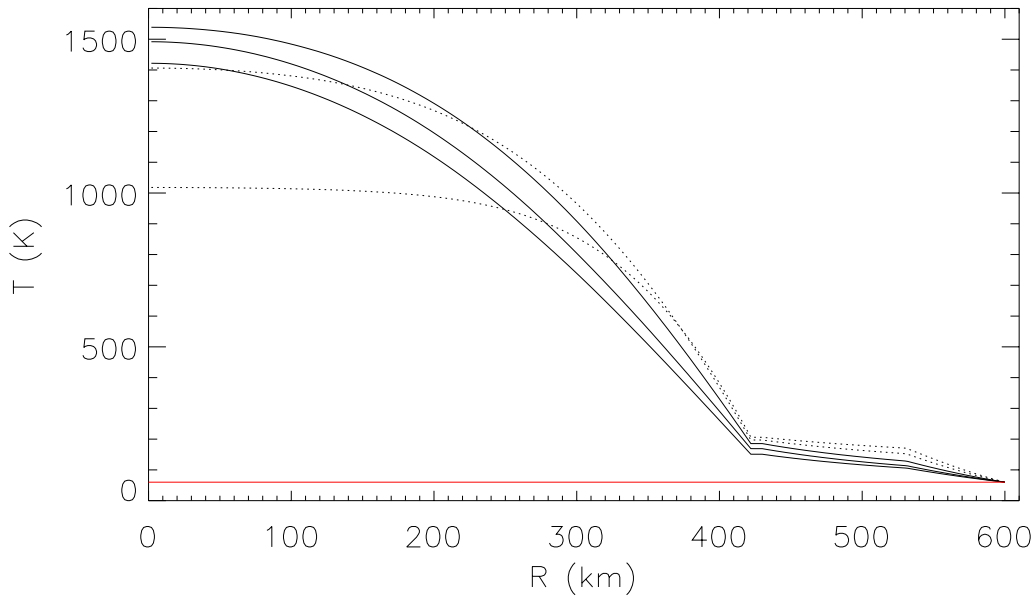

Figure 5.3: Temperatures within a combined Stokes flow model, at times $t = 0$ (red line), $t = 1\,\mathrm{Gyr}$ and $2\,\mathrm{Gyr}$ (dotted curves), and (solid curves, from top to bottom) $t = 3\,\mathrm{Gyr}$, $4\,\mathrm{Gyr}$ and the present day, $t = 4.56\,\mathrm{Gyr}$

5.6 The New Canonical Model for Charon Including Rayleigh-Taylor Instabilities

Having reviewed the effects of parameter changes with respect to the models of Desch et al. (2009), it is now time to consider the effect of the inclusion of Rayleigh-Taylor instabilities in the new model. Rayleigh-Taylor instabilities are incorporated in the simulations by lowering the differentiation temperature used in the model runs. As described previously, this new differentiation temperature, $T_{\mathrm{diff}} = 143$ K, is the critical temperature at which a disturbance in the boundary layer between the ice mantle and the overlying crust can be expected to grow by at least a factor of 10 over

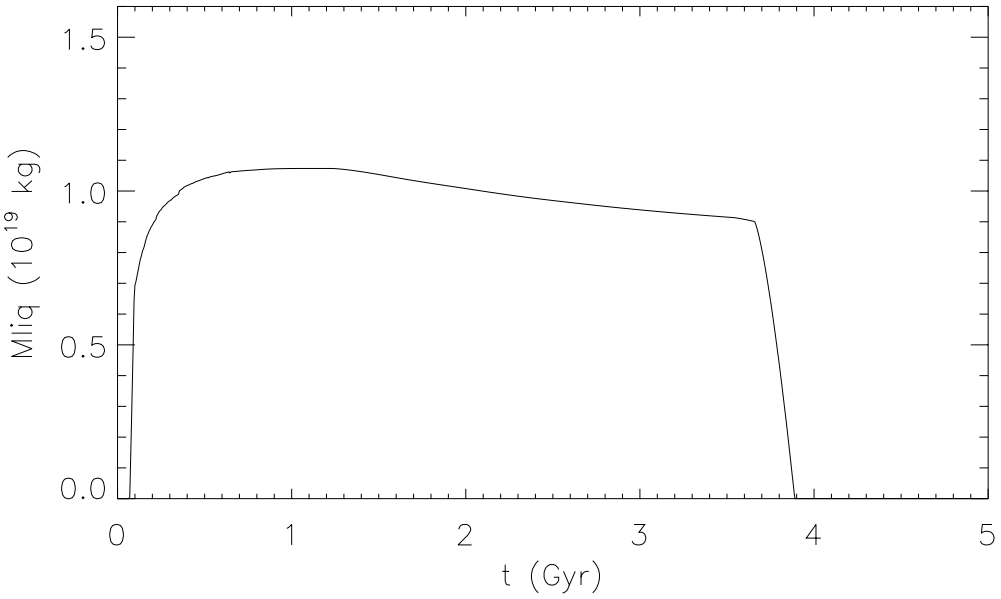

Figure 5.4: Total mass of liquids within the combined Stokes flow model as a function of time.

a time period $\tau = 1.5\,\mathrm{Gyr}$. τ is determined by measuring how long the boundary layer is able to stay within 10 K of T_{diff} in our simulations. As implemented in the code, any layer which ever sees a temperature above T_{diff} is expected to differentiate due the effect of Rayleigh-Taylor instabilities.

The simulation which represents our new canonical model for Rayleigh-Taylor instabiltiies is one in which $T_{\mathrm{diff}} = 145$ K with $k_{\mathrm{rock}} = 0.5\,\mathrm{W\,m^{-1}\,K^{-1}}$, $\rho_{\mathrm{rock}} = 2.35\,\mathrm{g\,cm^{-3}}$, $\bar{\rho} = 1.65\,\mathrm{g\,cm^{-3}}$, and using the new parametrization for ice convection. In the discussion that follows, I will be comparing this model to the base model which only considers differentiation via Stokes flow.

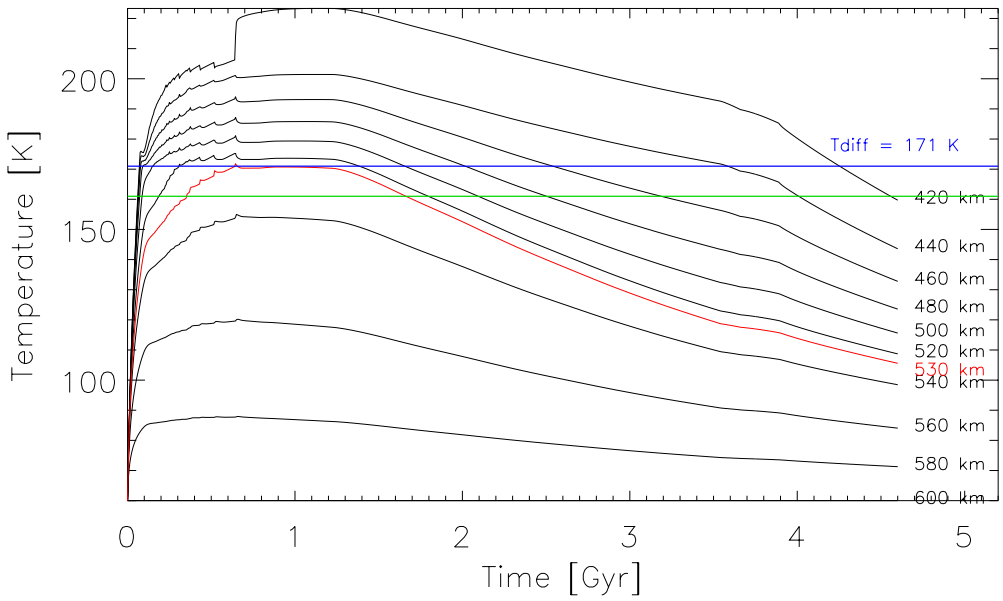

Figure 5.5: Temperature evolution for specific shells found within the new base model for Stokes flow. The innermost shells are the hottest, and the shells decrease in temperature as we move outward from the core. The blue line represents the threshold temperature for differentiation of $T_{\rm diff} = 171$ K. The outermost shell which is expected to differentiate just barely crosses this threshold temperature. This shell, $R_{\rm diff}$, is at 530 km, and is depicted in red. As explained in the text, this shell remains within 10 K of $T_{\rm diff}$ for about 1.5 Gyr.

In the results of the new canonical simulation for Rayleigh-Taylor instabilities, the radius of the core increase from 422 to 432 km, with a concurrent increase in the mass of the core from 7.4×10^{20} to 7.91×10^{20} kg. The radius of maximum differentiation also increases from 530 to 542 km, with a resulting concurrent decrease in the mass of the crust from 4.64×10^{20} to 3.92×10^{20} kg. Finally, the percent of the total mass of the body found in the crust decreases from 31.08% to 26.29%. For comparison with the Stokes flow model, Fig. 5.6 displays the compositional structure of this model at

2 Gyr, before the liquid has had a chance to fully freeze.

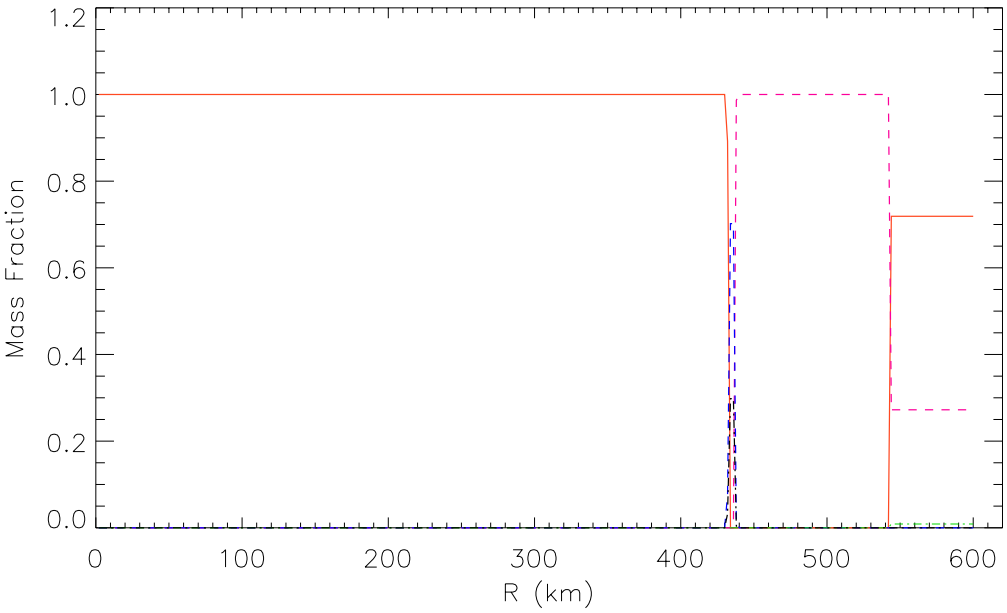

Figure 5.6: Distribution of phases for the new canonical model representing the effects of Rayleigh-Taylor instabilities at $t = 2\,\mathrm{Gyr}$. The lines represent rock (orange), solid or liquid water (dashed lines), and ammonia dihydrate or liquid ammonia (dash-dot lines). A core of pure rock exists within 432 km. Between 432 and 438 km there is a layer of water/ammonia liquid, and from 438 to 542 km there is a layer of pure water ice. From 542 km to the surface at 600 km there is an undifferentiated crust of rock, water ice and ADH.

In comparison with the base model for differentiation due to Stokes flow alone, the inclusion of Rayleigh-Taylor instabilities raises the maximum temperature of the core from 1541 to 1566 K. Additionally, the core now reaches its peak temperature a little later at 3.14 versus 3.08 Gyr. These two effects are probably the result of the lowered differentiation temperature at which Rayleigh-Taylor instabilities can take effect. Differentiation now takes place at greater radii than is possible in a

model which includes the effects of Stokes flow alone. This increase in the outermost differentiation radius, $R_{\rm diff}$, allows more bulk rocky material to sink to the core. Since this rocky material contains the radioactive nuclei, then not only does the size of the core increase, but its overall production of radiogenic heating increases as well. In Fig. 5.7, we see the thermal history for the new canonical model which now includes the effect of Rayleigh-Taylor instabilities.

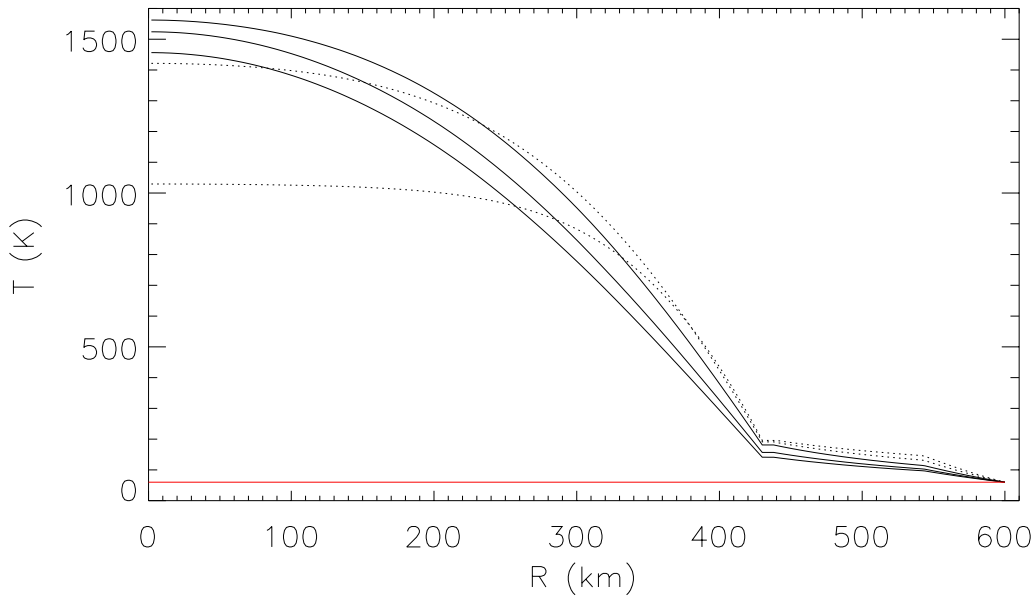

Figure 5.7: Temperatures within the new canonical model showing the effect of the inclusion of Rayleigh-instabiltiies, at times $t = 0$ (red line), $t = 1\,\mathrm{Gyr}$ and $2\,\mathrm{Gyr}$ (dotted curves), and (solid curves, from top to bottom) $t = 3\,\mathrm{Gyr}$, $4\,\mathrm{Gyr}$ and the present day, $t = 4.56\,\mathrm{Gyr}$

There is no change in the instantaneous maximum amount of liquid found in the body as compared with a model including the effects of Stokes flow alone. However,

the last of the liquid now freezes at 3.52 Gyr as opposed to 3.89 Gyr. For comparison, Fig. 5.8 shows the amount of liquid present in the model over time.

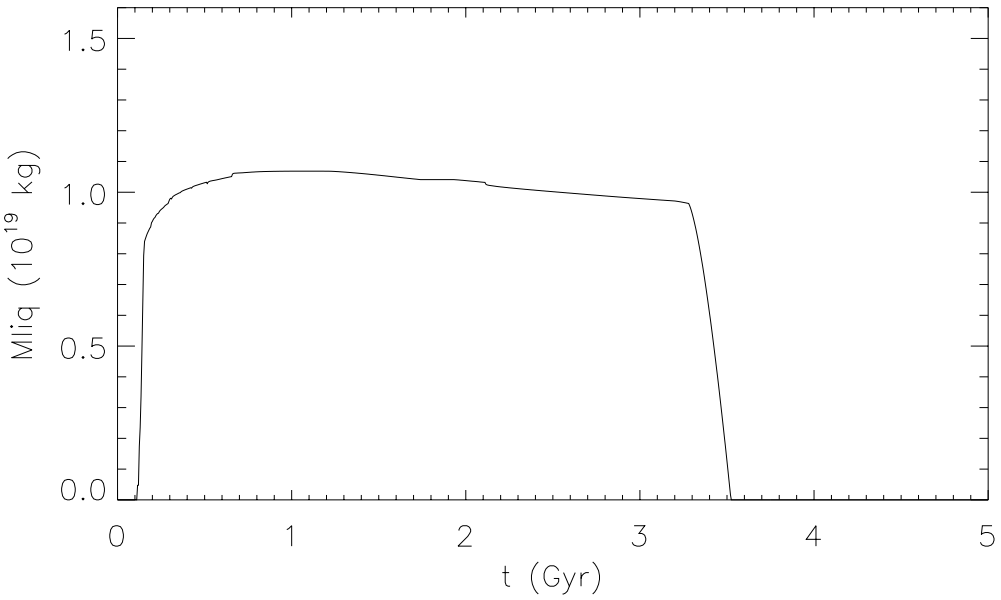

Figure 5.8: Total mass of liquids within the new canonical model as a function of time, showing the inclusion of the effects of Rayleigh-Taylor instabilities.

The final plot for this model (Fig. 5.9) graphically illustrates the temperature evolution for individual shells experiencing differentiation through the combined effects of Stokes flow and Rayleigh-Taylor instabilities. As in the plot for Stokes flow alone, only the outermost shells are displayed in this plot, beginning with one at a radius of 420 km. The innermost shells are the hottest, and as we move outwards from the core, we reach a shell that just barely crosses the threshold temperature for differentiation via Rayleigh-Taylor instabilities of $T_{\text{diff}} = 145$ K. Our model assumes

that this shell at the boundary layer between the ice mantle and the undifferentiated crust will begin to experience Rayleigh-Taylor instabilities once it is within 10 K of $T_{\rm diff}$ (green line), and these will continue until the shell is fully differentiated. This shell (shown in red) has an outer radius of 542 km, which is the maximum radius of differentiation, $R_{\rm diff}$, for this model. Any shell outside of this radius never rises above $T_{\rm diff}$, and will therefore never differentiate. Note that the time period, τ, for which the shell remains within 10 K of $T_{\rm diff}$ is again on the order of 1.5 Gyr.

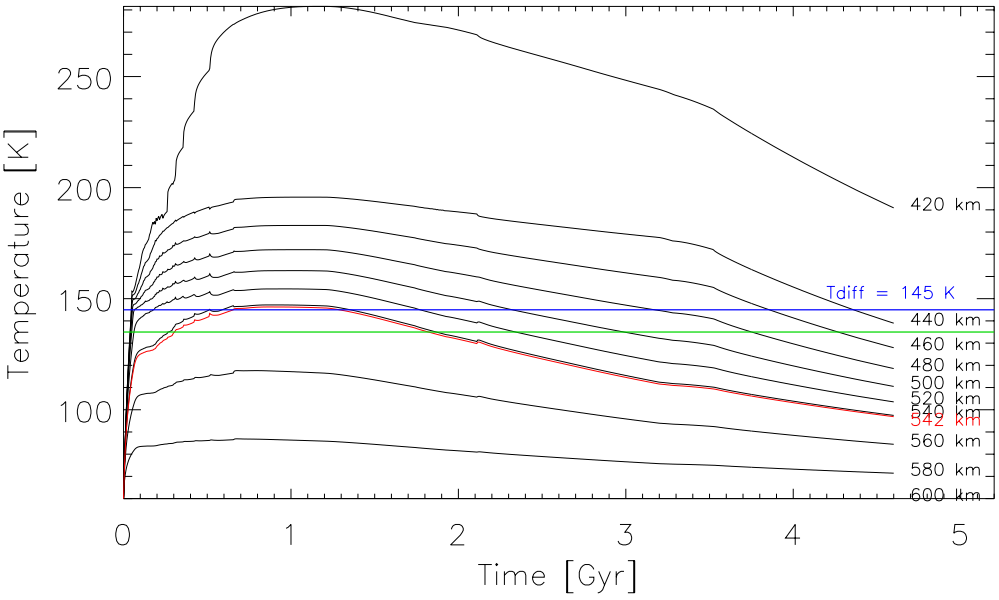

Figure 5.9: Temperature evolution for specific shells found within the new canonical model including the effects of Rayleigh-Taylor instabilities. The innermost shells are the hottest, and the shells decrease in temperature as we move outward from the core. The blue line represents the threshold temperature for differentiation of $T_{\rm diff} = 145$ K. The outermost shell which is expected to differentiate just barely crosses this threshold temperature. This shell, $R_{\rm diff}$, is at 542 km, and is depicted in red. As explained in the text, this shell remains within 10 K of $T_{\rm diff}$ for about 1.5 Gyr.

5.6.1 *Effect of Varying the Differentiation Temperature for the New Canonical Model*

For completeness, we reviewed the new canonical model which includes Rayleigh-Taylor instabilities for two other differentiation temperatures close to $T_{\rm diff} = 143$ K. This is to take into account the fact that the differentiation temperature depends on parameters such as ice grain size, which cannot presently be fixed via observation. For $T_{\rm diff} = 140$ K as opposed to 145 K, the maximum radius of the core increases by 4 km, to 436 km, with a concurrent increase in the mass of the core from 7.91×10^{20} to 8.09×10^{20} kg. The differentiation radius increases from 542 to 546 km, with a resulting concurrent decrease in the mass of the crust from 3.92×10^{20} to 3.68×10^{20} kg. The percent of the total mass of the body found in the crust decreases from 26.29% to 25.47%.

For a $T_{\rm diff} = 135$ K, the maximum radius of the core increases by 6 km to 438 km, with a concurrent increase in the mass of the core from 7.91×10^{20} to 8.18×10^{20} kg. The differentiation radius increases from 542 to 548 km, with a resulting concurrent decrease in the mass of the crust from 3.92×10^{20} to 3.55×10^{20} kg. The percent of the total mass of the body found in the crust decreases from 26.29% to 23.81%. There is relatively little change in the other results, except that the time at which the final liquid freezes steadily decreases with decreasing $T_{\rm diff}$ from 3.52 to 3.35 to 3.26 Gyr, for $T_{\rm diff} = 145$, 140 and 135 K, respectively. Therefore it is clear that the models are not too sensitive to $T_{\rm diff}$ over this 10 K range of differentiation temperatures.

5.7 Parameter Study for the New Canonical Model

For models with differentiation temperatures appropriate for the inclusion of the effects of Rayleigh-Taylor instabilities, we explored varying two of the model param-

eters.

5.7.1 Change in Thermal Conductivity

The first parameter varied was the thermal conductivity of rock changing it from $k_{\rm rock} = 0.5$ to $1.0\,{\rm W\,m^{-1}\,K^{-1}}$, while maintaining the density of that rock at $\rho_{\rm rock} = 2.35\,{\rm gm\,cm^{-3}}$. This change has little effect on the maximum extent of the core as compared with the model where $k_{\rm rock} = 0.5\,{\rm W\,m^{-1}\,K^{-1}}$. For $T_{\rm diff} = 135$ K and 145 K there is no change; and for $T_{\rm diff} = 140$ K, the radius decreases slightly from 436 to 434 km. Similarly, the radius of differentiation remains unchanged for $T_{\rm diff} = 135$ K and 145 K, and again decreases slightly from 546 to 544 km for $T_{\rm diff} = 140$ K.

The increased value for the thermal conductivity does lower the maximum temperature achieved by the core from about 1570 K to 1220 K, and causes this temperature change to occur about 1 billion years earlier in these models. This again reflects the increased ability for heat to escape from the core as a result of the increased value of thermal conductivity. Finally, the time at which the liquid freezes for these models decreases somewhat from the prior values of 3.26, 3.35 and 3.52 Gyr, to 3.19, 3.28 and 3.34 Gyr; respectively, for $T_{\rm diff} = 135$, 140 and 145 K.

5.7.2 Change in Density of Rock

The second is to change the value for the density of the rocky material from $\rho_{\rm rock} = 2.35$ to $3.25\,{\rm g\,cm^{-3}}$ in conjunction with changing the thermal conductivity from $k_{\rm rock} = 0.5$ to $1.0\,{\rm W\,m^{-1}\,K^{-1}}$. These two changes combined return our values for the density and thermal conductivity of the rocky material back to values similar to that of the olivine-type rock found in the models of Desch et al. (2009). This change has the overall effect of increasing the proportion of ice to rock in the simulations, thereby decreasing the size of both the rocky core and the differentiation radius. For

$T_{\rm diff}$ = 135, 140 and 145 K, the sizes of the core decrease from 438, 436 and 432 km to 360, 358 and 356 km, respectively. Similarly, for $T_{\rm diff}$ = 135, 140 and 145 K, the differentiation radii decrease from 548, 546 and 542 km to 530, 528 and 524 km, respectively.

The maximum temperature achieved by the core for each of these models decreases by about 150 K, and again occurrs about 1 billion years earlier in these models as compared with our new canonical model. Finally, the time at which the liquid freezes for these models increases significantly from the prior values of 3.26, 3.35 and 3.52 Gyr, to 4.08, 4.08 and 4.14 Gyr; respectively, for $T_{\rm diff}$ = 135, 140 and 145 K.

5.8 Summary

In summary, we found that for all of the models with differentiation temperatures appropriate to Rayleigh-Taylor instabilities, there remains a significant undifferentiated crust with a thickness of at least 52 km. This is despite the consideration of the effect of the inclusion of Rayleigh-Taylor instabilities on the differentiation process. We have been conservative in our approach, allowing R-T instabilities to overturn the crust if they are able to grow by only a factor of 10 in 1.5 Gyr. This result is significant and implies that many Kuiper belt objects in the size range of Charon may only partially differentiate, leaving a sizable undifferentiated crust. Table 5.8 summarizes the differentiation extent for all of the models considered above.

Table 5.1: Summary of differentiation radii for all models

Model				R_{diff}
T_{diff}	ρ_{rock}	k_{rock}	Visc Param	
174[a]	3.25	1.0	Th	514 km
174[b]	3.25	1.0	Th	504 km
176	3.25	1.0	GK	506 km
174	2.35	1.0	Th	526 km
176	3.25	0.5	Th	498 km
171[c]	**2.35**	**0.5**	**GK**	**530 km**
135	2.35	0.5	GK	548 km
140	2.35	0.5	GK	546 km
145[d]	**2.35**	**0.5**	**GK**	**542 km**
135	2.35	1.0	GK	548 km
140	2.35	1.0	GK	544 km
145	2.35	1.0	GK	542 km
135	3.25	1.0	GK	530 km
140	3.25	1.0	GK	528 km
145	3.25	1.0	GK	524 km

[a] $\bar{\rho} = 1.70\,\mathrm{g\,cm^{-3}}$

[b] $\bar{\rho} = 1.65\,\mathrm{g\,cm^{-3}}$

[c] Combined Stokes Flow Model

[d] New Canonical Model

Chapter 6

CONCLUSIONS

6.1 Background

Since their discovery more than twenty years ago, Kuiper Belt Objects and other outer solar system icy bodies have emerged as exciting worlds with interesting geologies. With frigid surface temperatures of less than 60 K, and volume fractions of water and other ices on the order of 50%, their thermal evolution and differentiation processes are unique in the solar system. Here liquid water can take on the role of terrestrial magmas, and volcanic plumes of water and dissolved ammonia can erupt from their surface in cryovolcanic outflows. My current research extends the KBO thermal evolution models of Desch et al. (2009) to include the effect of Rayleigh-Taylor instabilities in their evolution. In particular, I model the ability of a Charon-like body to maintain a substantial undifferentiated crust on top of its pure ice mantle.

The thermal evolution models of Desch et al. begin with an undifferentiated body that accretes cold as a mixture of rocky material ($\rho_{\rm rock} = 3.25\,{\rm g\,cm^{-3}}$) and ices ($\rho_{\rm ice} \sim 1\,{\rm g\,cm^{-3}}$). Long-lived radioactive isotopes accreted within the rocky material gradually heat the body. The inclusion of ammonia in the model with mass fraction $\geq 1\%$ relative to water causes the viscosity of the ice to drop by 5 orders of magnitude when the first melt is produced at 176 K. This facilitates Stokes flow, allowing meter-sized rocks to begin fall towards the core on geological timescales. Over time, layer upon layer of material differentiates, eventually forming a hot rocky core ($\rho \sim 3\,{\rm g\,cm^{-3}}$), surrounded by a liquid layer containing water and ammonia, which is in turn surrounded by a pure water ice mantle ($\rho \sim 1\,{\rm g\,cm^{-3}}$). The model predicts

that for a Charon-sized body with $\bar{\rho} = 1.70\,\mathrm{g\,cm^{-3}}$, the outer crust will never rise above $T = 176$ K and will therefore never differentiate. This undifferentiated crust was predicted to have a thickness of 85 km up to the present day.

In this thesis I address two significant objections to the model. The first is that the rock that initially accreted with ice and other volatiles to form the KBO may not have existed as meter-sized rock, but rather as particles centimeter-sized or smaller. Stokes flow is inadequate to separate these particles from the ice except at much higher temperatures. Also, Stokes flow will not operate on geological timescales if there is insufficient ammonia contained within the KBO. The second objection is that the existence of an undifferentiated crust with $\bar{\rho} \sim 1.70\,\mathrm{g\,cm^{-3}}$ atop a lower-density ice mantle is gravitationally unstable and therefore prone to Rayleigh-Taylor instabilities. These instabilities could completely overturn the crust if given sufficient time. Any unstable density stratification will eventually succumb to Rayleigh-Taylor instabilities, but the rate of growth depends on the viscosity, which can slow the growth rate to Gyr or more. The models in this thesis quantify the ability of Rayleigh-Taylor instabilities to overturn the undifferentiated crust of a Charon-like body.

Please note that the models in this thesis assume that some differentiation has already occurred, either via Stokes flow or through a melting of the ice at 273 K. It is at this point that Rayleigh-Taylor instabilities can take hold within the boundary layer between the ice mantle and crust. It is this second possible stage of differentiation that the thesis focuses on. The differentiation temperatures and critical viscosities calculated pertain specifically to this boundary layer in an attempt to see if Rayleigh-Taylor instabilities will continue the differentiation process, perhaps all the way out to the surface.

Chapter 2 describes a linear stability analysis I performed on the boundary layer between the ice mantle and the overlying crust based on the work of Chandrasekhar

(1961). The results of this analysis show that the growth rate for a Rayleigh-Taylor instability on this boundary layer is

$$n \approx \frac{\lambda}{2\pi} \frac{g(\bar{\rho} - \rho_{\rm ice})}{2\eta_{\rm ice}\,(1 + f(\phi))}, \tag{6.1}$$

where λ is the wavelength of the disturbance (parallel to the interface) and $\eta_{\rm ice}$ is the viscosity of the ice. Long wavelengths grow fastest but λ is limited to the planetary radius, so there is a limit to how fast Rayleigh-Taylor instabilities can operate. For the case of Charon in particular, amplitudes increase by less than a factor of 10 in 1.5 Gyr (roughly the time the interface will be at its maximum temperature) if $\eta > \eta_{\rm crit} \approx 1.09 \times 10^{22}\,{\rm Pa\,s}$. Theoretically, Rayleigh-Taylor instabilities can always operate, but if the viscosity of the ice mantle exceeds $\eta_{\rm crit}$, they are insufficient to effect an overturn of the crust on geological timescales. Since η generally increases with decreasing temperature, I found that the exceedingly cold temperatures on the surface of KBOs are sufficient to suppress Rayleigh-Taylor instability-driven overturn.

Chapter 3 explores the distinctly non-Newtonian rheology of water ice at the very low temperatures found in KBOs. Based on the work of Goldsby and Kohlstedt (2001), I computed the strain rate $\dot{\epsilon}$ as a function of stress σ, for each of four processes (volume diffusion, basal slip, grain boundary sliding, and dislocation creep). For each process the flow law $\dot{\epsilon} = A\sigma^n d^{-p} \exp(-Q^*/RT)$ holds, with different parameters A, n, p and Q^* for each process, and different dependencies on ice grain size d. The total strain rate is then found to be $\dot{\epsilon}_{\rm total} = \dot{\epsilon}_{\rm diff} + \dot{\epsilon}_{\rm disl} + (\dot{\epsilon}_{\rm bs}^{-1} + \dot{\epsilon}_{\rm GBS}^{-1})^{-1}$. Knowing the relationship between stress and strain allows us to determine the viscosity as $\eta = \sigma/(2\dot{\epsilon}) \times f(\phi)$, where $f(\phi)$ represents an enhancement to the viscosity due to the presence of rock with a volume fraction ϕ. Based on the formulas of Friedson & Stevenson (1983) for Charon, $\phi \approx 0.51$ and $f(\phi) \approx 16.83$.

For the purpose of our models, it is not possible to know the value for σ, a priori,

as it depends on the process initially creating the disturbance. Since the Rayleigh-Taylor instabilities must operate within $\tau = 1.5$ Gyr to be effective in overturning the crust, we fix the strain rate to $\dot{\epsilon} = 1/\tau = 2.11 \times 10^{-17}\,\mathrm{s}^{-1}$ which corresponds with the time period τ used to determine η_{crit} above. Combining this strain rate with the critical viscosity determined in Chapter 2 fixes σ. Once we know σ and $\dot{\epsilon}$ and fix the grain size d, the flow laws of Goldsby and Kohlstedt uniquely determine the temperature T_{diff} at which this will occur. For the case of our Charon analog with d fixed at 1 mm, $\bar{\rho} = 1.65\,\mathrm{g\,cm}^{-3}$, $\rho_{\mathrm{rock}} = 2.35\,\mathrm{g\,cm}^{-3}$ and $\rho_{\mathrm{ice}} = 0.935\,\mathrm{g\,cm}^{-3}$, we find $T_{\mathrm{diff}} = 143$ K.

Based on these results, I ran the thermal evolution code of Desch et al. (2009) for the case of Charon, assuming that zones that reach $T > T_{\mathrm{diff}} = 135$, 140 or 145 K differentiate, but zones that always remain below T_{diff} do not. I found that shells whose maximum temperature is near T_{diff} tend to remain at those temperatures for only 1.5 Gyr or so. This justifies our assumption that Rayleigh-Taylor instabilities have to operate in this time frame to be effective.

6.2 Summary of Findings

I ran the first set of model simulations at $T_{\mathrm{diff}} \approx 176$ K, the temperature at which the first melt of ammonia allows Stokes flow to become a viable mechanism for differentiation. The initial run with $\bar{\rho} = 1.70\,\mathrm{g\,cm}^{-3}$, $\rho_{\mathrm{rock}} = 3.25\,\mathrm{g\,cm}^{-3}$, $\rho_{\mathrm{ice}} = 0.935\,\mathrm{g\,cm}^{-3}$ and $k_{\mathrm{rock}} = 1\,\mathrm{W\,m}^{-1}\,\mathrm{K}^{-1}$ successfully replicated the results of Desch et al. (2009), resulting in a crustal thickness of 86 km at the present time. All of the remaining models were run with $\bar{\rho} = 1.65\,\mathrm{g\,cm}^{-3}$ to more accurately reflect current observations for the size and mass of Charon. This decrease in mean density required an increase the amount of ice relative to rock (with its embedded radioactive isotopes). This yielded a decrease in the maximum temperature of the core, and a

resultant decrease in the radius of maximum differentiation from 514 to 504 km.

Before proceeding with our Rayleigh-Taylor simulations, I decided to address the likelihood that the rocky material that accreted to form Charon was closer in composition to that of substantially aqueously altered CM chondrites than the olivine-type rock considered in previous models. To this end, we considered models where $\rho_{\rm rock}$ was changed from 3.25 to $2.35\,{\rm g\,cm^{-3}}$, and $k_{\rm rock}$ from 1.0 to $0.5\,{\rm W\,m^{-1}\,K^{-1}}$. Changing $\rho_{\rm rock}$ to $2.35\,{\rm g\,cm^{-3}}$ requires a substantial increase in the ratio of rock to ice and results in an increase in $R_{\rm diff}$ to 526 km. Changing the thermal conductivity of the rock to $0.5\,{\rm W\,m^{-1}\,K^{-1}}$ slightly decreases $R_{\rm diff}$ to 498 km, although it does have a substantial effect on the thermal history of the body, delaying the onset of the maximum temperatures in the core by about 1 Gyr. Finally, I implemented a change in the parametrization for ice convection in the model where the underlying viscosity of the ice is more accurately modeled through the use of Goldsby and Kohlstedt's ice flow laws. This change had minimal impact, increasing $R_{\rm diff}$ by 2 km to 506 km.

The final run in this set of simulations included the effect of changing all three parameters simultaneously for the Stokes flow model. This model becomes the new base model for Stokes flow, with $\bar{\rho} = 1.65\,{\rm g\,cm^{-3}}$, $\rho_{\rm rock} = 2.35\,{\rm g\,cm^{-3}}$, $\rho_{\rm ice} = 0.935\,{\rm g\,cm^{-3}}$, $k_{\rm rock} = 0.5\,{\rm W\,m^{-1}\,K^{-1}}$, and ice convection modeled using the flow laws of Goldsby and Kohlstedt. The resulting $R_{\rm diff}$ for this model increases to 530 km, still leaving a substantial crust of 70 km thickness.

The inclusion of Rayleigh-Taylor instabilities in the model substantially lowers the temperature at which shells of material can differentiate, lowering $T_{\rm diff}$ from about 176 to 143 K. This new canonical model for Charon includes all of the parameter changes listed above for the base Stokes flow model with $T_{\rm diff} = 145$ K. This model results with $R_{\rm diff}$ increasing to 542 km, but still leaving a substantial crust of 58 km. In this range, $R_{\rm diff}$ is relatively insensitive to $T_{\rm diff}$, only increasing by 6 km when

$T_{\rm diff}$ is lowered by 10 K. Changing the thermal conductivity of the rock from $k_{\rm rock}$ from 0.5 back to $1.0\,{\rm W\,m^{-1}\,K^{-1}}$ had almost no impact on the resulting thickness of the crust in the range where $T_{\rm diff}$ is between 135 and 145 K. Changing both $k_{\rm rock}$ to $1.0\,{\rm W\,m^{-1}\,K^{-1}}$ and $\rho_{\rm rock} = 3.25\,{\rm g\,cm^{-3}}$ reduces $R_{\rm diff}$ by exactly 18 km for $T_{\rm diff} = 135$, 140 and 145 K.

The final result is that the inclusion of the effects of Rayleigh-Taylor instabilities in our models for the thermal evolution of our Charon analog still results in the production of a substantial crust with a thickness of at least 52 km. This result is quite robust, only changing by 6 km when varying $T_{\rm diff}$ by 10 K, and actually increasing in thickness by 18 km when we return to our models with $k_{\rm rock} = 1.0\,{\rm W\,m^{-1}\,K^{-1}}$ and $\rho_{\rm rock} = 3.25\,{\rm g\,cm^{-3}}$. This result can be extended to other KBOs whose typical surface temperatures are closer to 40 K. In all of our models we found that the temperature gradient from the surface of the crust to the top of the ice mantle was ~ 2 K per km. Thus, the change in temperature of 100 K required for Rayleigh-Taylor instabilities to overturn the crust aren't typically reached until the crust has a thickness of at least 50 km.

6.3 Final Speculations and Future Research

Through the results of the model simulations, I found that a body like Charon will sustain a substantial crust on the order of 50 km or more, even in the face of Rayleigh-Taylor instabilities. This result is quite robust, and it would probably require an impactor on the order of 50 km to overturn the crust of a body like Charon. Additionally, KBOs whose surface temperatures are even lower than that of Charon will have even higher viscosities in the ice mantle and be therefore be less likely to have their crust overturn through the action of Rayleigh-Taylor instabilities.

The implications of having a substantially undifferentiated crust can be quite far

reaching. In particular, since this crust is thermally insulating, it can support the existence of subsurface liquid long after it could exist within a completely differentiated body. This subsurface liquid is a likely source for cryovolcanism as the liquid begins to freeze. Cryovolcanism can have spectacular results on KBOs similar to those already observed on the surface of the icy moons of the giant planets. Cryovolcanism can also have a significant impact on the resurfacing of KBOs, and emplacing crystalline water ice and ammonia on the surface which might otherwise be destroyed. This could alter the surface chemistry of the KBO as well as any spectroscopy observed from space. A final, possibly spectacular result, might be the creation of conditions conducive to the formation of life at the boundary between the hot, rocky core and the subsurface ocean above it. Although this would be a very surprising result, the discovery of chemosynthetic life at the bottom of Earth's oceans at "black smokers" was also unpredicted.

Future work will include a much broader parameter study considering a wide range of radii and densities. In particular, I would like to consider the model for other icy bodies such as Quaoar, Orcus and Rhea to model their ability to retain an undifferentiated crust. With some modifications, other solar system objects such as the the moons of Uranus could also be modeled. An exciting application of this model is the simulation of the thermal evolution of Rhea to determine its current structure. From this modeled structure its moment of inertia can be predicted and then compared with the moment of inertia observationally determined during the *Cassini* probe's most recent flyby. A final exciting prospect is the *New Horizons* mission to Pluto and Charon. Direct observations of the surface of Charon can help to provide evidence as to whether it has been resurfaced by cryovolcanism over the last 100 Myr. This could help to prove the existence of subsurface liquid up to the present epoch, thereby verifying one of the predictions of the thermal evolution models.

A final important consideration for future work is the inclusion of methanol in the model. Methanol has been frequently observed in comets at levels relative to water up to 6%, and typically around 2% (Bockelee-Morovan et al. 2004). Like ammonia, methanol is an effective antifreeze, and a ternary composition of water, ammonia and methanol (in the ratio 47:23:30) will freeze at an even lower temperature (153 K) than a water-ammonia mixture will (Kargel 1994). For most of the models presented in this thesis, the last liquid is found to freeze between 3 and 4 Gyr after the accretion of the KBO. This result suggests that cryovolcanism may not be occurring today on our Charon-like analog. However, the inclusion of methane in the model and its ability to further lower the melting point of the ice will probably result in differentiation out to a larger radii. This would result in the formation of a larger rocky core which could retain heat longer. The lowered melting point of the ice from 176 to 153 K would probably delay the onset of the final freezing of the liquid for an additional 0.6 - 2 Gyr (Desch et al. 2009). Thus, the inclusion of methanol in the model might allow cryovolcanism to occur up to the present epoch.

REFERENCES

Arakawa, M., Maeno, N. 1994. Effective viscosity of partially melted ice in the ammonia-water system. Geophysical Research Letters 21, 1515-1518.

Bockelée-Morvan, D., Crovisier, J., Mumma, M. J., Weaver, H. A. 2004. The composition of cometary volatiles. Comets II 391-423.

Brown, M. E. 2012. The Compositions of Kuiper Belt Objects. Annual Review of Earth and Planetary Sciences 40, 467-494.

Buie, M. W., Grundy, W. M., Young, E. F., Young, L. A., Stern, S. A. 2006. Orbits and Photometry of Pluto's Satellites: Charon, S/2005 P1, and S/2005 P2. The Astronomical Journal 132, 290-298.

Castillo-Rogez, J. 2006. Internal structure of Rhea. Journal of Geophysical Research (Planets) 111, 11005.

Castillo-Rogez, J. C., Matson, D. L., Sotin, C., Johnson, T. V., Lunine, J. I., Thomas, P. C. 2007a. Iapetus' geophysics: Rotation rate, shape, and equatorial ridge. Icarus 190, 179-202.

Castillo-Rogez, J. C., McCord, T. B., Davies, A. G. 2007b. Ceres: Evolution and Present State. Lunar and Planetary Institute Science Conference Abstracts 38, 2006.

Chandrasekhar, S. 1961. Hydrodynamic and hydromagnetic stability. International Series of Monographs on Physics, Oxford: Clarendon, 1961.

Cook, J. C., Desch, S. J., Roush, T. L., Trujillo, C. A., Geballe, T. R. 2007. Near-Infrared Spectroscopy of Charon: Possible Evidence for Cryovolcanism on Kuiper Belt Objects. The Astrophysical Journal 663, 1406-1419.

Crawford, G. D., Stevenson, D. J. 1988. Gas-driven water volcanism in the resurfacing of Europa. Icarus 73, 66-79.

Croft, S. K., Lunine, J. I., Kargel, J. 1988. Equation of state of ammonia-water liquid - Derivation and planetological applications. Icarus 73, 279-293

De Sanctis, M. C., Capria, M. T., Coradini, A. 2001. Thermal Evolution and Differentiation of Edgeworth-Kuiper Belt Objects. The Astronomical Journal 121, 2792-2799.

Desch, S. J., Cook, J. C., Doggett, T. C., Porter, S. B. 2009. Thermal evolution of Kuiper belt objects, with implications for cryovolcanism. Icarus 202, 694-714.

Dombard, A. J., McKinnon, W. B. 2001. Formation of Grooved Terrain on Ganymede: Extensional Instability Mediated by Cold, Superplastic Creep. Icarus 154, 321-336.

Durham, W. B., Stern, L. A. 2001. Rheological Properties of Water Ice-Applications to Satellites of the Outer Planets. Annual Review of Earth and Planetary Sciences 29, 295-330.

Durham, W. B., Prieto-Ballesteros, O., Goldsby, D. L., Kargel, J. S. 2010. Rheological and Thermal Properties of Icy Materials. Space Science Reviews 153, 273-298.

Edgeworth, K. E. 1943 The evolution of our planetary system. Journal of the British Astronomical Association, vol. 53, p. 181-188 (1943).

Ellsworth, K., Schubert, G. 1983. Saturn's icy satellites - Thermal and structural models. Icarus 54, 490-510.

Figueredo, P. H., Greeley, R. 2004. Resurfacing history of Europa from pole-to-pole geologimapping. Icarus 167, 287-312.

Fortes, A. D., Wood, I. G., Brodholt, J. P., Vočadlo, L. 2003. The structure, ordering and equation of state of ammonia dihydrate (nh_3 . $2h_2o$). Icarus 162, 59-73.

Goldsby, D. L., Kohlstedt, D. L. 2001. Superplastic deformation of ice: Experimental observations. Journal of Geophysical Research 106, 11017.

Gulbis, A. A. S., and 12 colleagues 2006. Charon's radius and atmospheric constraints from observations of a stellar occultation. Nature 439, 48-51.

Hansen, C. J., Esposito, L., Stewart, A. I. F., Colwell, J., Hendrix, A., Pryor, W., Shemansky, D., West, R. 2006. Enceladus' Water Vapor Plume. Science 311, 1422-1425.

Hill, R. H. 1950. The Mathematical Theory of Plasticity. Oxford: University Press. 355.

Hussmann, H., Sohl, F., Spohn, T. 2006. Subsurface oceans and deep interiors of medium-sized outer planet satellites and large trans-neptunian objects. Icarus 185, 258-273.

Jewitt, D., Luu, J. 1993. Discovery of the candidate Kuiper belt object 1992 QB1. Nature 362, 730-732.

Kargel, J. S. 1992. Ammonia-water volcanism on icy satellites - Phase relations at 1 atmosphere. Icarus 100, 556-574.

Kargel, J. S. 1994. Cryovolcanism on the icy satellites. Earth Moon and Planets 67, 101-113.

Kargel, J. S., Pozio, S. 1996. The Volcanic and Tectonic History of Enceladus. Icarus 119, 385-404.

Kirk, R. L., Stevenson, D. J. 1987. Thermal evolution of a differentiated Ganymede and implications for surface features. Icarus 69, 91-134.

Kivelson, M. G., Khurana, K. K., Russell, C. T., Volwerk, M., Walker, R. J., Zimmer, C. 2000. Galileo Magnetometer Measurements: A Stronger Case for a Subsurface Ocean at Europa. Science 289, 1340-1343.

Kuiper, G. P. 1951. On the origin of the solar system. In Astrophysics - A topical Symposium, ed. J. A. Hynek (New York: McGraw-Hill), 357-424.

Leonard, F. C. 1930. The new planet Pluto. Leaflet Astron. Soc. Pacific No. 30, August, 121-124.

Lorenz, R. D., Shandera, S. E. 2001. Physical properties of ammonia-rich ice: Application to Titan. Geophysical Research Letters 28, 215-218.

Mastrapa, R. M. E., Brown, R. H. 2006. Ion irradiation of crystalline H_2O ice: Effect on the 1.65-μm band. Icarus 183, 207-214.

McKinnon, W. 1998. Geodynamics of Icy Satellites. Solar System Ices 227, 525.

McKinnon, W. B. 1999. Convective instability in Europa's floating ice shell. Geophysical Research Letters 26, 951-954.

McKinnon, W. B. 2002. On the initial thermal evolution of Kuiper Belt objects. Asteroids, Comets, and Meteors: ACM 2002 500, 29-38.

Mueller, S., McKinnon, W. B. 1988. Three-layered models of Ganymede and Callisto - Compositions, structures, and aspects of evolution. Icarus 76, 437-464.

Multhaup, K., Spohn, T. 2007. Stagnant lid convection in the mid-sized icy satellites of Saturn. Icarus 186, 420-435.

Nimmo, F., Pappalardo, R. T., Giese, B. 2002. Effective elastic thickness and heat flux estimates on Ganymede. Geophysical Research Letters 29, 1158.

Nimmo, F., Pappalardo, R. T. 2004. Furrow flexure and ancient heat flux on Ganymede. Geophysical Research Letters 31, 19701.

Olkin, C. B., Wasserman, L. H., Franz, O. G. 2003. The mass ratio of Charon to Pluto from Hubble Space Telescope astrometry with the fine guidance sensors. Icarus 164, 254-259.

Opeil, C. P., Consolmagno, G. J., Britt, D. T. 2010. The thermal conductivity of meteorites: New measurements and analysis. Icarus 208, 449-454.

Person, M. J., Elliot, J. L., Gulbis, A. A. S., Pasachoff, J. M., Babcock, B. A., Souza, S. P., Gangestad, J. 2006. Charon's Radius and Density from the Combined Data Sets of the 2005 July 11 Occultation. The Astronomical Journal 132, 1575-1580.

Porco, C. C., and 24 colleagues 2006. Cassini Observes the Active South Pole of Enceladus. Science 311, 1393-1401.

Prialnik, D., Bar-Nun, A. 1990. Heating and melting of small icy satellites by the decay of Al-26. The Astrophysical Journal 355, 281-286.

Press, W. H., Teukolsky, S. A., Vetterling, W. T., Flannery, B. P. 1992. Numerical recipes in FORTRAN. The art of scientific computing. Cambridge: University Press, —c1992, 2nd ed. .

Reynolds, R. T., Cassen, P. M. 1979. On the internal structure of the major satellites of the outer planets. Geophysical Research Letters 6, 121-124.

Ruiz, J. 2003. Heat flow and depth to a possible internal ocean on Triton. Icarus 166, 436-439.

Schubert, G., Stevenson, D. J., Ellsworth, K. 1981. Internal structures of the Galilean satellites. Icarus 47, 46-59.

Schubert, G., Spohn, T., Reynolds, R. T. 1986. Thermal histories, compositions and internal structures of the moons of the solar system. IAU Colloq. 77: Some Background about Satellites 224-292.

Schubert, G., Anderson, J. D., Travis, B. J., Palguta, J. 2007. Enceladus: Present internal structure and differentiation by early and long-term radiogenic heating. Icarus 188, 345-355.

Shchuko, O. B., Coradini, A., Orosei, R., Shchuko, S. D. 2006. Varuna: Thermal evolution. Advances in Space Research 38, 1946-1951.

Showman, A. P., Mosqueira, I., Head, J. W. 2004. On the resurfacing of Ganymede by liquid water volcanism. Icarus 172, 625-640.

Shulman, L. M. 2004. The heat capacity of water ice in interstellar or interplanetary conditions. Astronomy and Astrophysics 416, 187-190.

Sirono, S.-I., Yamamoto, T. 1997. Thermal conductivity of granular materials relevant to the thermal evolution of cometary nuclei. Planetary and Space Science 45, 827-834.

Smith, B. A., and 10 colleagues 1979. The Galilean satellites and Jupiter - Voyager 2 imaging science results. Science 206, 927-950.

Solomatov, V. S. 1995. Scaling of temperature- and stress-dependent viscosity convection. Physics of Fluids 7, 266-274.

Song, M., Cole, D. M., Baker, I. 2006. Investigation of Newtonian creep in polycrystalline ice. Philosophical Magazine Letters 86, 763-771.

Stern, S. A. 2008. The New Horizons Pluto Kuiper Belt Mission: An Overview with Historical Context. Space Science Reviews 140, 3-21.

Thomas, P. J., Reynolds, R. T., Squyres, S. W., Cassen, P. M. 1987. The Viscosity of Miranda. Lunar and Planetary Institute Science Conference Abstracts 18, 1016.

Vitense, C., Krivov, A. V., Löhne, T. 2010. The Edgeworth-Kuiper debris disk. Astronomy and Astrophysics 520, A32.

Yomogida, K., Matsui, T. 1983. Physical properties of ordinary chondrites. Journal of Geophysical Research 88, 9513-9533.

Zahnle, K., Schenk, P., Levison, H., Dones, L. 2003. Cratering rates in the outer Solar System. Icarus 163, 263-289.